The University of Cape Town

MSc. Thesis

Biological tissue mechanics with fibres modelled as one dimensional *Cosserat* continua. Applications to cardiac tissue in healthy and diseased states.

Author:
Kevin Sack

Supervisor:
Dr. Sebastian Skatulla

A thesis submitted in fulfilment of the requirements for the degree of Master of Science in Engineering

May 2014

The financial assistance of the National Research Foundation (NRF) towards this research is hereby acknowledged. Opinions expressed and conclusions arrived at, are those of the author and are not necessarily to be attributed to the NRF.

Declaration of Authorship

I, Kevin Sack, declare that this thesis titled, 'Biological tissue mechanics with fibres modelled as one dimensional *Cosserat* continua. Applications to cardiac tissue in healthy and diseased states.' and the work presented in it are my own. I confirm that:

- This work was done wholly or mainly while in candidature for a research degree at this University.
- I know the meaning of plagiarism and declare that all the work in the document, save for that which is properly acknowledged, is my own.
- Where any part of this thesis has previously been submitted for a degree or any other qualification at this University or any other institution, this has been clearly stated.
- Where I have consulted the published work of others, this is always clearly attributed.

Signed: _____

Date: _____

Abstract

Biological tissue mechanics with fibres modelled as one dimensional *Cosserat* continua. Applications to cardiac tissue in healthy and diseased states.

by Kevin Sack

Classically, the elastic behaviour of cardiac tissue mechanics is modelled using anisotropic strain energy functions capturing the averaged behaviour of its fibrous microstructure. The strain energy function can be derived via representation theorems for anisotropic functions where a suitable nonlinear strain tensor, e.g. the Green strain tensor, describes locally the current state of strain [57, 150, 158]. These kinds of approaches, however, are usually of phenomenological nature and do not elucidate on the complex heterogeneous material composition of cardiac tissue characterized by different fibre hierarchies interwoven by collagen, elastin and coronary capillaries [61, 115]. Thus, pathological changes of microstructural constituents, e.g. with regards to the extra cellular matrix, and their implications on the macroscopically observable material behaviour cannot be directly investigated.

In this research the fibrous characteristics of the myocardium are modelled by one dimensional *Cosserat* continua. This additionally allows for the inclusion of fibre motion relative to the matrix representing the non-local material response due to twisting and bending of fibres. In this sense, a so-called characteristic scaling parameter associated with the micro structure, becomes a material parameters of the formulation. The ability to explicitly account for torsion and bending in the constitutive law gives this approach a natural advantage over classical formulations. Moreover, the additional degrees of freedom in the kinematic description allow for more complex, realistic deformations. The assumed hyperelastic material behaviour of myocardial tissue is represented by a nonlinear strain energy function which includes the contributions linked to the *Cosserat* fibre continuum and the complementary terms which refer to the extra-cellular matrix.

Utilizing the element-free Galerkin method, simulations of the left ventricle undergoing various stages of the cardiac cycle are introduced to investigate ventricular tissue mechanics.

Acknowledgements

It would not have been possible to write this thesis without the help and support of the kind people around me. In particular, I would like to thank and express my appreciation to the following:

My supervisor, Dr Sebastian Skatulla, for providing the interesting topic and giving me support, patience and guidance during the research.

All the past and present students and staff at the Centre for Research in Computational and Applied Mechanics.

The funding and resources that were provided by the University of Cape Town, the National Research Foundation (NRF) and the Centre for High Performance Computing (CHPC).

Finally, my family and friends that provided their unconditional support and encouragement.

Contents

List of Figures

List of Tables

Chapter 1

Introduction

Cardiovascular disease is the single leading cause of death in the world accounting for 30% of all human mortality [4]. Despite the recent advancements of pharmaceutical, surgical, device and tissue engineered therapy strategies, cardiovascular disease remains one of the most costly, common and deadly medical conditions. Despite current world-wide efforts to treat cardiovascular disease, projections show an increase in predicted mortality [1], keeping cardiovascular disease as the leading cause of death globally [4, 87]. Historically, clinical treatments for cardiovascular disease have been developed primarily by trial and error as opposed to a comprehensive understanding of the structural and mechanical changes that a diseased heart undergoes. Recent advancements in numerical methods and the proliferation of inexpensive high performance computing power has enabled more sophisticated simulation tools that could allow for greater insight into cardiovascular disease and guide the development of modern therapies.

Specifically, understanding and accurately describing the material and mechanical behaviour of the cardiac tissue is of great importance. The wall of the heart consists of three distinct layers known as the endocardium, myocardium and epicardium. The endocardium and epicardium have little functional influence for mechanical considerations and are of the order of $100\mu m$. Our focus will be on the description of the myocardium tissue in the left ventricle. Figure 1.1, reproduced from Holzapfel and Ogden [58] outlines the geometry and structure of the left ventricle starting from the macro-scale and further focusing on the basic structure of a small scale block. Mathematically describing the point located at the origin of fibre local coordinate systems in Figure 1.1 (d) is the primary objective this research.

[1] Reliable projections up until 2030.

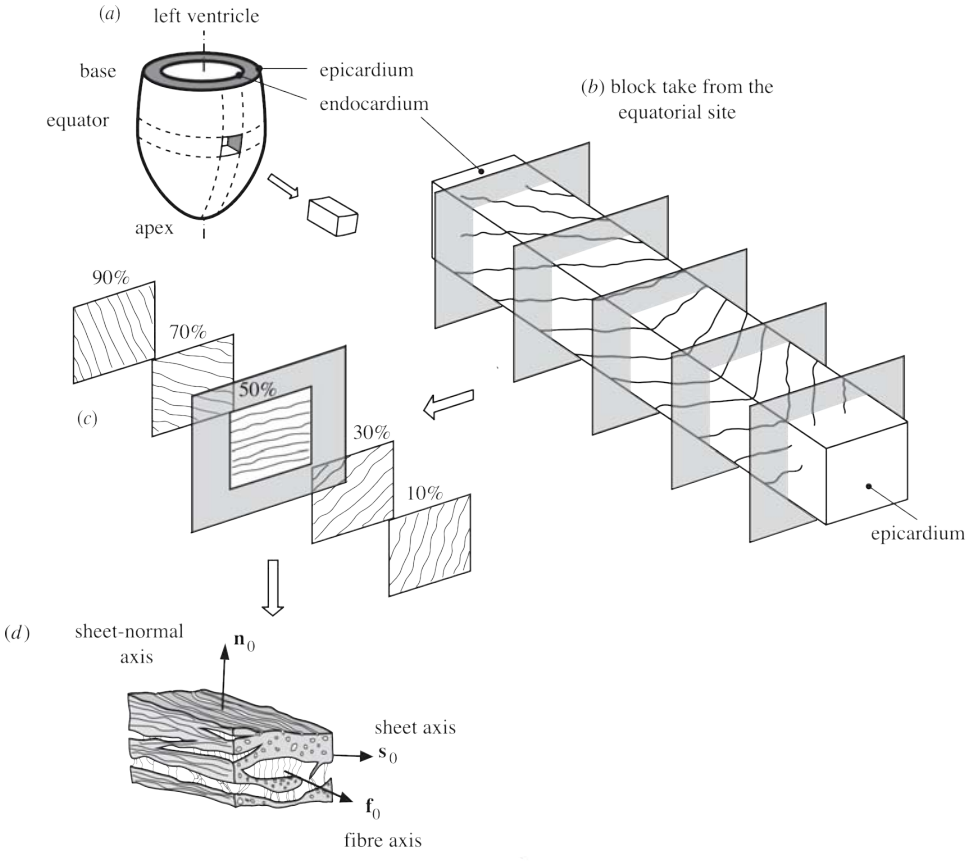

FIGURE 1.1: Schematic diagram of: (a) the left ventricle of the heart; (b) the structure through the thickness of a block taken from the equator of the left ventricle; (c) Five distinct layers showing the fibre orientation; (d) the layered organisation of myocytes and the collagen fibres between sheets.

An important aspect when creating constitutive laws for cardiac modelling is the accurate description and representation of the fibrous nature of the myocardium tissue. Mathematically this is best thought of as a non-linear, hyperelastic material with orthotropic properties arising from the micro-structure influence of the myocyte fibres.

1.1 Modelling of biological tissue mechanics

Modelling the mechanical behaviour of the heart has been a scientific endeavour for the last 30 years. The development of this field can be considered a part of a larger goal to accurately model human soft tissue. Different models over time have been introduced and have either been successfully developed or discarded for more accurate or efficient alternatives. What was originally modelled as an elastic or visco-elastic material, lacked the mechanical influences of the complex structure to accurately describe myocardium tissue. Specifically over the last 15 years, models have introduced phenomenological

properties as a means to overcome the complex structure on a macro and micro scale. A problem to this approach is the shortage in in experimental data suitable for detailed parameter estimation. Increasing attempts to include the micro structural influences have emerged with the hope to better capture the complex material response by placing a larger influence on the multi-scale physics underlying the behaviour.

The following outlines the various model developments for *passive material behaviour* of myocardial tissue, starting with the first published attempts and concluding with the most recent, relevant and sophisticated formulations published in the last few years.

Yuan-Cheng Fung is credited in the literature [61, 63, 118] for being one of the first to describe a constitutive relationship for passive myocardial behaviour. What was initially proposed as a linear isotropic strain energy function was later developed as a quadratic and then an exponential description. The first invariant based constitutive model is credited to Humphrey and Yin [65]. The strain energy function introduced an exponential "fibre specific" term to account for the material anisotropy. The early developments of Fung-type strain energy functions were limited to describing the myocardium as transversely isotropic [63].

Costa et al. [26] extended the formulation of Fung to an orthotropic formulation by introducing a fibre specific coordinate system and specifying principle material stiffness along the fibre, sheet and normal directions. The orthotropic formulation has varied slightly over time with minor modifications being introduced. Common formulations include those presented in Usyk et al. [147], Kerckhoffs [72], Holzapfel and Ogden [58] and others.

The need to place a larger emphasis on the micro structure is expressed heavily in the literature [47, 58, 134]. Over the last 10 years, significant progress has been made to achieve this with multi-scale modelling. Smith et al. [133] introduced a one of the first multi-scale models, by including cellular considerations for calculating the global active tension during contraction. Hussan et al. [66] includes micro mechanical contributions from the myocytes (and their perimysial collagen mesh), modelling them as cylinders with mechanical degrees of freedom corresponding to twist, bend and splay. In the mechanical modelling of hard biological tissue, various micro continuum approaches have also been investigated [2, 18, 103, 157]. However soft biological tissue remains significantly under investigated with respect to micro continuum theories.

1.2 Cosserat continuum theory

Classical theories of solid mechanics follow the theory of continua outlined by Cauchy in the early 19^{th} century for homogeneous elastic solids in the small strain deformation range. Maugin [88] summarises the main axioms of Cauchy that hold for classic materials in the following four statements:

1. *Cauchys postulate.* The traction exerted on a face of a solid depends on the geometry of that face only (i.e the local unit normal); it will be linear in that normal and independent of the curvature of the internal surface. The notion of a stress tensor follows, the so called stress being the only "internal force" in the theory.
2. It is understood that the matter in the solid is continuously distributed and fills the entire region of space it occupies (i.e the body is Euclidean and connected), as opposed to discrete particles with empty spaces.
3. There are no applied couples in both volume and surface.
4. There exists no microstructure described by additional internal degrees of freedom.

In this context, a representative volume element (RVE) is considered a substantial representation of the entire body, with regards to mechanical behaviour. As a result the material behaviour of the RVE undergoing external loading can be utilized to find material parameters that correspond to the entire body and in the limit for a single material point. In this sense, material parameters are always associated with the RVE and are a statistical average. The concept is based on the assumption that the RVE is large enough in comparison to the micro-constituents of the material to the effect that any micro-structure behaviour is averaged out. While the concept can and is applied successfully to many materials and models, in the case where the characteristic length of the micro-constituents are large enough in comparison to the dimensions of the body (i.e small scale structures, granular materials etc) this assumption breaks down [6].

The emergence of a generalized continua stem from a relaxation of the four basic axioms outlined above, with the motivation to describe material behaviour including a deeper understanding of kinematics at small scales.

The development of generalized continuum theories and the ideas that led to the description of micropolar continuum were pioneered by Cauchy, Voigt, Helmholtz, Kelvin, the Cosserat brothers and others at the turn of the 19^{th} century. The seminal work of the Cosserat brothers, *Théorie des corps déformables* [25] was the first official introduction

of these ideas. Following the publication, there was a significant period of stagnation in the field. It took almost five decades for new work in the field to appear [3]. Important study and progress of linear *Cosserat* theory was developed by Toupin [143, 144], Mindlin and Tiersten [91, 92], Eringen and Suhubi [34, 36], Kessel [73], Neuber [95], Schaefer [126] and many others.

In Generalized continuum theories that include the micro structure, each material point is associated with additional degrees of freedom usually relating to the micro continuum. A common representation of this, is to introduce a set of micro directors at the material point, and formulate a kinematic description accordingly.

Taking up again the idea of micro-directors attached to each material point, it is possible to constrain the motion of these directors in such a way that the micro body only exhibits certain strain conditions. This can be useful to mathematically model multi-scale physics problems, with micro continuum deformation. Various classifications exist, based on the deformation modes experienced by the micro continuum (or directors)[122]. These can be summarised as

1. Micropolar: if the micro continuum behaves as a rigid body;
2. Microstretch: if only stretch and rigid body rotations are considered; and
3. Micromorph: for stretch, shear and rigid body rotations [35].

Micropolar continuum mechanical models originated in the *Cosserat* theory of elasticity [25] and are characterized by the property that each material point inherits a rotation field which is independent of and additional to the conventional displacement field. The material response of a body to an external force is a corresponding force stress field (force per unit area) as well as a couple stress field (torque per unit area). A micropolar elastic solid will contain at least one additional material parameter in comparison to a corresponding classical elastic solid. These additional elastic constants corresponding to the couple stress are dependent on a characteristic length scale parameter which can be related to the material's micro structure.

It was shown that the classical couple stress theories (which contain no characteristic length parameter), like those proposed by Toupin [144] were encompassed as special cases of the *Cosserat* continuum theory [27].

Additionally, classical elasticity assume that stress at a material point is dependent on local features, i.e strain, strain rate, and strain history at a given point, and do not account for contributions from neighbouring points. This treatment neglects physical properties that become relevant when the micro and macro length scales are comparable

and the continuum behaviour at a point is influenced by the deformation of neighbouring points. In contrast, *Cosserat* continuum theory does account for the influence of neighbouring material points by introducing curvature and couple stresses into the kinematics and constitutive laws of the problem. These contributions are scaled by a characteristic length which is a direct and elegant method of including information about the micro structure.

Another method of dealing with heterogeneous materials is to establish a relation between macro and micro features in terms of localization and homogenization techniques [1, 45]. Significant work has been done in this field, particularly with respect to higher order homogenization techniques and their ability to capture the size effects of the micro space [76, 77].

The motivation for utilizing a generalized continuum formulation is strongly supported by experimental observations. Problems that are characterized by size scale effects, whereby the interaction between the micro and macro constituents of a material changes with their relative ratio is well documented. This has been found with the torsional hardening of copper wires, dependant on the diameter [42], the elastic bending of polypropylene microcantilevers [90], and the rigidity in porous synthetic material [79]. Also in hard biological tissue, such as wet bone, similar size-scale effects were noticed due to the ratio of pore diameters with respect to the specimen size [2, 18, 103, 157].

In all cases classical elastic theories substantially failed to predict the experimental results, whereas the generalized continuum theories were more successful. Of particular interest, the experiments with hard biological tissue were seen to be very successfully modelled using the *Cosserat* theory applied by Park and Lakes [103] as well as the strain gradient theory developed by Aifantis [2].

The development of nonlinear, i.e geometrically exact, *Cosserat* and micropolar theories is presented in the works of Sansour and Bufler [124]; Steinmann [136]; Sansour and Bednarczyk [123]; Forest et al. [44]; Sansour [119] and others. This allows for a geometrically exact description of finite deformation and rotation.

1.3 Thesis motivation, aims and objectives

Biological tissue is a complex heterogeneous material with a significant hierarchical micro-structure that influences the material on a macro scale [39, 61, 115, 129]. Cardiac tissue is no exception, with the collagen enmeshed fibres being the dominant material constituent and orientated in a significantly complex arrangement. The majority of computational research attempt to account for this through a phenomenological approach.

However these approaches rely heavily on experimental data, of which there is a significant shortage. There is an increasing need to include micro continuum influences, modelling the multi-scale physics of cardiac mechanics more accurately. The successful inclusion of generalized continua approaches, including *Cosserat* models, in the application to other hard biological tissue, i.e bone [2, 39, 103, 115], has proved successful in capturing more realistic material responses.

Motivated by these results in hard biological tissue, this research intends to adopt the work of Sansour and Skatulla [121] and extend its application to soft biological tissue. One can hypothesize that including contributions from the micro level will create more accurate multi scale simulations and furthermore will provide a more complete understanding of cardiac function. This study aims to include one dimensional *Cosserat* rods as a mathematical representation of the fibre bundles found within cardiac tissue. Investigation into the higher order contributions from the one dimensional rods will be analysed in application to small cardiac specimens and left ventricular representations. The model will be tested by comparison of simulated and experimental data.

1.4 Organization of thesis

In Chapter 2 the fundamentals of classical continuum mechanics needed to describe cardiac mechanics are reviewed. The kinematic measures used to describe deformation and the stress measures needed to relate forces to deformation are introduced. Finally, the constitutive laws for a hyperelastic material are introduced to describe materials with isotropic, transversely isotropic and orthotropic properties.

In Chapter 3 the framework for the *Cosserat* continuum is introduced. The *Cosserat* strain tensors and their variational forms are derived. This is followed by the presentation of the variational principle based on the *Cosserat* continuum which includes the corresponding equilibrium equations.

In Chapter 4 a suitable one dimensional *Cosserat* continuum framework is introduced specifically for the applicable to one dimensional fibre bundles. The fibre local coordinate system is also introduced and the necessary *Cosserat* strains are derived for application to the one dimensional continuum. The fibre specific variational principle is presented.

In Chapter 5 the various constitutive laws used to investigate cardiac mechanics are introduced. These include both linear and nonlinear laws presented for homogenised and non-homogenised materials. Additionally a novel and equivalent strain invariant form is introduced for the nonlinear formulation.

In Chapter 6 the physiology of the heart is reviewed. The morphology, fibre orientation and simplified geometry of the left ventricle is discussed. The passive and active mechanics of the heart are considered with respect to healthy and diseased heart function. Finally, the boundary conditions controlling the cardiac cycle are introduced.

In Chapter 7 the passive mechanical model is then simulated and validated with pressure volume relationships of experimental results. The mechanical model is extended to simulate the active stages of the cardiac cycle in a healthy heart. The results of the healthy model are compared with experimental data and literature results. Initial investigation into modelling diseased cardiac function is also presented.

In Chapter 8 the key results are summarised and their significance discussed. Recommendations for further development of this cardiac model are discussed.

Chapter 2

Classical continuum mechanics

Continuum mechanics is a mathematical discipline that deals with the analysis of the kinematics and mechanics of deformable materials where the materials are modelled as continuous media, as opposed to discrete particles. The mathematical preliminaries of continuum mechanics are essential to the analysis and study of cardiac mechanics.

The fundamental assumption is that the material is continuous and completely fills the space it occupies. Additionally the underlying molecular structure is generalised by the overlying material properties. Thus, each point can be subjected to any kind of stress and strain, based on certain physical and material laws, in the same way as the overall structure, irrespective of its size.

In this chapter, fundamental equations relating to non-linear continuum mechanics will be introduced and the relations of these equations to stress and strain will be highlighted as they have been employed quite extensively afterwards. For more detailed descriptions and derivations, the reader may consult Mase and Mase [86].

2.1 Kinematics in classical continua

Consider a body $\mathcal{B}$ in a three dimensional Euclidean vector space characterised as the reference state (i.e the undeformed configuration). $\mathcal{B}$ is parametrised by the Cartesian coordinates X_1, X_2 and X_3 where the associated basis vectors are denoted by $\mathbf{e}_1, \mathbf{e}_2$ and $\mathbf{e}_3$. After being subjected to certain boundary conditions, the body, at time t, in its deformed state is referred as $\mathcal{B}_t$. To describe this transition of state, a non-linear deformation mapping $\varphi : \mathcal{B} \to \mathcal{B}_t$ is introduced, enabling us to define the relation of a material point in the reference configuration $\mathbf{X} \in \mathcal{B}$ and the current configuration

$\mathbf{x} \in \mathcal{B}_t$:

$$\mathbf{x} = \varphi(\mathbf{X}, t) \qquad \text{and} \qquad \mathbf{X} = \varphi^{-1}(\mathbf{x}, t) \tag{2.1}$$

The mapping $\varphi(\mathbf{X}, t)$ is defined as a bijective function, i.e. each *material coordinate* $\mathbf{X} \in \mathcal{B}$ has a unique and corresponding *spatial coordinate* $\mathbf{x} \in \mathcal{B}_t$ and the same is given for the inverse map, φ^{-1}, from $\mathcal{B}_t$ to $\mathcal{B}$.

Following the derivation of Sansour and Skatulla [121], we introduce $\vartheta^i,\ i = 1, 2, 3$, the coordinate system parametrizing convected $\mathcal{B}$, we define, $\mathbf{G}_i$, the co-variant tangent vectors spanning the corresponding tangent space $\mathcal{TB}$ by

$$\mathbf{G}_i = \frac{\partial \mathbf{X}}{\partial \vartheta^i} \qquad \text{with} \qquad \mathbf{G}_i \in \mathcal{TB}. \tag{2.2}$$

Similarly for $\mathcal{TB}_t$ being the tangent space of $\mathcal{B}$, the covariant base vector is

$$\mathbf{g}_i = \frac{\partial \mathbf{x}}{\partial \vartheta^i} \qquad \text{with} \qquad \mathbf{g}_i \in \mathcal{TB}_t. \tag{2.3}$$

The following operators with respect to the material (or reference) configuration and spatial (or current) configuration are considered in Table 2.1:

TABLE 2.1: Gradient and Divergence operation in the material and spatial configuration

	Configuration	
Operator	Material	Spatial
Gradient	$\text{Grad}(\bullet) = \frac{\partial}{\partial \mathbf{X}}(\bullet) = \boldsymbol{\nabla}(\bullet)$	$\text{grad}(\bullet) = \frac{\partial}{\partial \mathbf{x}}(\bullet) = \boldsymbol{\nabla}_t(\bullet)$
Divergence	$\text{Div}(\bullet) = \frac{\partial}{\partial X_i}(\bullet) \cdot \mathbf{e}_i = \boldsymbol{\nabla} \cdot (\bullet)$	$\text{div}(\bullet) = \frac{\partial}{\partial x_i}(\bullet) \cdot \mathbf{e}_i = \boldsymbol{\nabla}_t \cdot (\bullet)$

With φ being known, the corresponding invertible linear tangent map $\mathbf{F}$ labelled as the deformation gradient tensor, is established as the gradient of φ. The *Jacobian* J given by the determinant of $\mathbf{F}$ is the measure of the change in volumes from from $\mathcal{B}$ to $\mathcal{B}_t$. Modelling realistic mechanics only allow for

$$J = \det\mathbf{F} = \det(\text{Grad}\ \varphi) > 0, \tag{2.4}$$

that is, a material undergoing deformation has to maintain volume. For the case when there is no deformation, we obtain the trivial solution that $\mathcal{B}_t$ coincides with $\mathcal{B}$, whereby $\mathbf{F} = \mathbf{1}$, the identity tensor. For this case $J = \det\mathbf{F} = 1$.

With the displacement field given by $\mathbf{u}(\mathbf{X}, t) = \mathbf{x}(\mathbf{X}, t) - \mathbf{X}$, the deformation gradient $\mathbf{F}$ can be alternatively defined as

$$\mathbf{F} = \mathbf{1} + \text{Grad } \mathbf{u}. \tag{2.5}$$

Utilizing (2.2) and (2.3) we can relate the covariant base vectors in the reference and current configurations by

$$\mathbf{g}_i(\vartheta^i, t) = \mathbf{G}_i + \mathbf{u}_{,i}, \tag{2.6}$$

Where the comma denotes a partial derivative. The corresponding dual contra-variant vectors are donated as $\mathbf{G}^i$ and $\mathbf{g}^i$ respectively. The *Riemannian* metric in each configuration is given by

$$G_{ij} = \mathbf{G}_i \cdot \mathbf{G}_j \qquad \text{and} \qquad g_{ij} = \mathbf{g}_i \cdot \mathbf{g}_j \tag{2.7}$$

respectively. The deformation gradient can equally be represented by as the tangent map

$$\mathbf{F} = \mathbf{g}_i \otimes \mathbf{G}^i, \tag{2.8}$$

which can further be considered as $\mathbf{F} = (\mathbf{G}_i + \mathbf{u}_{,i}) \otimes \mathbf{G}^i$, when using Eq. (2.6).

Any change in time is termed the local rate of change and expressed as,

$$\frac{\partial}{\partial t}(\bullet). \tag{2.9}$$

Therefore, the overall time rate of change is

$$\dot{\bullet} = \frac{D}{Dt}(\bullet) = \frac{\partial}{\partial t}(\bullet) + \frac{\partial}{\partial x_i}(\bullet)\frac{dx_i}{dt}. \tag{2.10}$$

Correspondingly, the Jacobian, can also vary with respect to time:

$$\dot{J} = J \text{ div } \dot{\mathbf{x}}. \tag{2.11}$$

For later usage, we also take into account that a surface element in its material configuration dA with its unit normal $\mathbf{n}$ is related to its counterpart in the spacial configuration da with its unit normal $\boldsymbol{\nu}$ by

$$\boldsymbol{\nu} da = J\mathbf{F}^{-T}\mathbf{n}\, dA, \tag{2.12}$$

and one can relate a volume element in the reference configuration dV to its counterpart in the current configuration dv by

$$dv = J\, dV. \tag{2.13}$$

The change in length of a line after deformation would require the difference between the length in the deformed configuration, $d\mathbf{x}^2$, and the undeformed one, $d\mathbf{X}^2$:

$$d\mathbf{x}^2 - d\mathbf{X}^2 = (\mathbf{F}^T\mathbf{F} - \mathbf{1}) : (d\mathbf{X} \otimes d\mathbf{X}). \tag{2.14}$$

Based on the above, the right *Cauchy-green* tensor is defined as:

$$\mathbf{C} = \mathbf{F}^T\mathbf{F}. \tag{2.15}$$

In turn, the *Green strain* tensor, symmetric in nature, can now also be introduced as a function of $\mathbf{C}$:

$$\mathbf{E} = \frac{1}{2}(\mathbf{C} - \mathbf{1}) = \frac{1}{2}(\mathbf{F}^T\mathbf{F} - \mathbf{1}). \tag{2.16}$$

The multiplicative or polar decomposition of $\mathbf{F}$ expresses the tensor as the product of an orthogonal rotation tensor $\mathbf{R}$ and a positive-definite stretch tensor $\mathbf{U}$

$$\mathbf{F} = \mathbf{R}\mathbf{U}. \tag{2.17}$$

Combined with Eq. (2.15), the right *Cauchy-green* tensor can also be expressed as,

$$\mathbf{C} = \mathbf{U}^\mathbf{2}. \tag{2.18}$$

With the eigenvalues of $\mathbf{U}$, the scalar invariants of $\mathbf{C}$ are:

$$I_1^{\mathrm{C}} = \mathrm{tr}(\mathbf{C}) = \lambda_1^2 + \lambda_2^2 + \lambda_3^2 \tag{2.19}$$

$$I_2^{\mathrm{C}} = \frac{1}{2}\left[(\mathrm{tr}\mathbf{C})^2 - \mathrm{tr}(\mathbf{C}^2)\right] = \lambda_1^2\lambda_2^2 + \lambda_2^2\lambda_3^2 + \lambda_3^2\lambda_1^2 \tag{2.20}$$

$$I_3^{\mathrm{C}} = \det(\mathbf{C}) = \lambda_1^2\lambda_2^2\lambda_3^2. \tag{2.21}$$

2.2 Stress measures

Stress is a physical quantity that expresses the distribution of internal forces on a continuous body. Stress inside a body arise as a reaction to external forces applied to the material. These can be body forces, $\mathbf{b}$ which apply to the entire bulk material (i.e gravity) or traction forces $\mathbf{t}^{(\boldsymbol{\nu})}$ which apply to the material's surface with unit normal $\boldsymbol{\nu}$ (i.e friction).

Following the *Cauchy stress* principle that the resulting force $\Delta\mathbf{f}$ on a surface element Δa which is part of a cutting plane throughout the body $\mathcal{B}_t$ defines in the limit the

traction vector $\mathbf{t}^{(\boldsymbol{\nu})}$ acting on the surface with normal $\boldsymbol{\nu}$:

$$\lim_{\Delta a \to 0} \frac{\Delta \mathbf{f}}{\Delta a} = \frac{d\mathbf{f}}{da} = \mathbf{t}^{(\boldsymbol{\nu})} \tag{2.22}$$

then the state of stress at each point $\mathbf{x} \in \mathcal{B}_t$ is introduced by the *Cauchy stress lemma*:

$$\mathbf{t}^{(\boldsymbol{\nu})}(\mathbf{x}, t) = \boldsymbol{\sigma}^T(\mathbf{x}, t)\boldsymbol{\nu}(\mathbf{x}, t) \tag{2.23}$$

with $\boldsymbol{\sigma}$ defined as the *Cauchy stress* tensor in the spatial coordinate of $\mathbf{x}$. If the stress state of the same point in the undeformed configuration is to be found, then the element surface to be considered is dA with a unit normal of $\mathbf{n}$:

$$\mathbf{t}^{(\boldsymbol{n})}(\mathbf{X}, t) = \mathbf{P}(\mathbf{X}, t)\, \mathbf{n}(\mathbf{X}, t) \tag{2.24}$$

with $\mathbf{P}$ being the first *Piola-Kirchhoff* stress tensor which is now a function of the coordinate $\mathbf{X}$. $\mathbf{P}$ relates stresses with forces in the current configuration as acting on areas in the reference configuration. It is desirable to construct another stress measure, the second *Piola-Kirchhoff* stress tensor which is related to the the first *Piola-Kirchhoff* through the deformation gradient

$$\mathbf{P} = \mathbf{FS}. \tag{2.25}$$

The second *Piola-Kirchhoff* stress tensor is completely defined in the material configuration and is symmetric, unlike $\mathbf{P}$. The symmetry of the second *Piola-Kirchhoff* tensor and others is a result of the conservation of angular momentum and is further discussed in Section 2.3. Using $\boldsymbol{\sigma}$, $\mathbf{P}$ can be defined differently. This is done by first assuming that a force $\mathbf{f}$ acting on da is not different to the one applied on dA. Therefore,

$$d\mathbf{f} = \mathbf{P}\mathbf{n}\, dA = \boldsymbol{\sigma}^T \boldsymbol{\nu} da = \boldsymbol{\sigma}^T \det(\mathbf{F})\mathbf{F}^{-T}\mathbf{n}\, dA. \tag{2.26}$$

Where, the first *Piola-Kirchhoff* stress can also be calculated from:

$$\mathbf{P} = \det(\mathbf{F})\boldsymbol{\sigma}^T\mathbf{F}^{-T}. \tag{2.27}$$

2.3 Balance laws of continuum mechanics

If a body is subjected to perturbations of any form (e.g force, temperature or magnetic field), then the following fundamental physical laws can be used to describe the behaviour of the body:

- **The law of Conservation of Mass** ensures that there is no mass loss or gain when the body change from the undeformed to the deformed configuration.
- **The law of Linear and Angular Momentum Conservation** is related to Newton's Second Law which defines the rate of change of linear and angular momentum over time, resulting in force and momentum.
- **The law of Energy Conservation** is related to the Principle law of Energy which states that energy can neither be created nor destroyed but can only change forms. However, in this project, we focus mainly on the conversion of energy into deformations.

2.3.1 Conservation of mass

Consider a continuum body $\mathcal{B}_t$ at time t or any arbitrary sub-body, whose mass is calculated by:

$$m = \int_{\mathcal{B}_t} \rho(\mathbf{x}, t)\, dv \tag{2.28}$$

with ρ being in the current configuration. The principle of conservation of mass states that the body will conserve its total mass throughout its motion. This asserts that the derivative with respect to time is zero

$$\dot{m} = \frac{d}{dt} \int_{\mathcal{B}_t} \rho(\mathbf{x}, t)\, dv = \int_{\mathcal{B}_t} \{\dot{\rho}(\mathbf{x}, t) + \rho(\mathbf{x}, t) \operatorname{div} \dot{\mathbf{x}}\}\, dv = 0. \tag{2.29}$$

Since $\mathcal{B}_t$ is arbitrary,

$$\dot{\rho}(\mathbf{x}, t) + \rho(\mathbf{x}, t) \operatorname{div} \dot{\mathbf{x}} = 0. \tag{2.30}$$

As the mass remains the same, irrespective of the different configurations it went through,

$$m = \int_{\mathcal{B}_t} \rho(\mathbf{x}, t)\, dv = \int_{\mathcal{B}} \rho_0(\mathbf{X})\, dV \tag{2.31}$$

where, ρ_0, is the density in the reference configuration. Using the Jacobian,

$$\int_{\mathcal{B}} \{\rho(\mathbf{X}, t)\, J - \rho_0(\mathbf{X})\}\, dV = 0. \tag{2.32}$$

Knowing that $\mathcal{B}$ is arbitrary, we are left with,

$$\rho(\mathbf{X}, t)\, J = \rho_0(\mathbf{X}). \tag{2.33}$$

If the derivative of the above is taken with respect to time,

$$\frac{d}{dt}\left(\rho(\mathbf{X}, t)\, J\right) = 0 \qquad \text{as} \qquad \frac{d}{dt}(\rho_0(\mathbf{X})) = 0. \tag{2.34}$$

Another useful equation that is proposed to evaluate the material derivative,

$$\frac{d}{dt}\int_{\mathcal{B}_t}\rho(\mathbf{x},t)\,A(\mathbf{x},t)\,dv=\int_{\mathcal{B}_t}\rho(\mathbf{x},t)\,\dot{A}(\mathbf{x},t)\,dv \tag{2.35}$$

where A is a field of unit mass.

2.3.2 Linear momentum conservation

If a material continuum body, $\mathcal{B}$, is subjected to a body force $\mathbf{b}$ and a surface traction $\mathbf{t}^{\boldsymbol{\nu}}$ is applied to a boundary surface, $\partial\mathcal{B}$, the principle of linear momentum states that the rate of change of the linear momentum equals the total resultant force acting on the body:

$$\frac{d}{dt}\int_{\mathcal{B}_t}\rho(\mathbf{x},t)\,\dot{\mathbf{x}}\,dv=\int_{\partial\mathcal{B}_t}\mathbf{t}^{(\boldsymbol{\nu})}(\mathbf{x},t)\,da+\int_{\mathcal{B}_t}\mathbf{b}(\mathbf{x},t)\,dv. \tag{2.36}$$

Introducing the *Cauchy stress lemma* and making use of the Gauss divergence theorem, Eq (2.36) is transformed into the global equation of motion:

$$\int_{\mathcal{B}_t}\left\{\rho(\mathbf{x},t)\,\ddot{\mathbf{x}}\;-\operatorname{div}\boldsymbol{\sigma}^T-\mathbf{b}(\mathbf{x},t)\right\}\,dv=\mathbf{0}. \tag{2.37}$$

The local form of the equation of motion is obtained if one acknowledges that $\mathcal{B}_t$ is arbitrary,

$$\operatorname{div}\boldsymbol{\sigma}^T+\mathbf{b}(\mathbf{x},t)=\rho(\mathbf{x},t)\,\ddot{\mathbf{x}}. \tag{2.38}$$

For constant velocity field, $\dot{\mathbf{x}}(\mathbf{x},t)$, the acceleration field, $\ddot{\mathbf{x}}$, is zero, reducing Eq (2.38) to the equilibrium equation:

$$\operatorname{div}\boldsymbol{\sigma}^T+\mathbf{b}(\mathbf{x},t)=\mathbf{0}. \tag{2.39}$$

The above steps can be repeated for quantities in the reference configuration. The global equation is now:

$$\frac{d}{dt}\int_{\mathcal{B}_t}\rho_0\dot{\mathbf{x}}(\mathbf{X},t)\,dV=\int_{\partial\mathcal{B}_t}\mathbf{t}^{(\boldsymbol{n})}(\mathbf{X},t)\,dA+\int_{\mathcal{B}_t}\mathbf{b}(\mathbf{x},t)\,dV. \tag{2.40}$$

Applying the Gauss' divergence theorem and utilizing Eq (2.24),

$$\int_{\mathcal{B}_t}\left\{\rho_0\ddot{\mathbf{x}}(\mathbf{X},t)\;-\operatorname{div}\mathbf{P}-\mathbf{b}(\mathbf{X},t)\right\}=\mathbf{0}. \tag{2.41}$$

Since $\mathcal{B}_t$ is arbitrary, to get the localised equation of motion which shall now be called the *Lagrangian equation of motion*:

$$\operatorname{div}\mathbf{P}+\mathbf{b}(\mathbf{X},t)=\rho_0\ddot{\mathbf{x}}(\mathbf{X},\mathbf{t}). \tag{2.42}$$

Finally, the Lagrangian equilibrium equation with constant velocity field is given by,

$$\operatorname{div}\mathbf{P} + \mathbf{b}(\mathbf{X}, t)\, dV = \mathbf{0}. \tag{2.43}$$

2.3.3 Angular momentum conservation

Angular momentum is defined as a moment of the linear momentum about a particular reference point, which is usually taken as the origin of a coordinate system:

$$\frac{d}{dt}\int_{\mathcal{B}_t} \mathbf{x} \times \rho(\mathbf{x}, t)\, \dot{\mathbf{x}}\, dv = \int_{\partial\mathcal{B}_t} \mathbf{x}\times\mathbf{t}^{(\boldsymbol{\nu})}(\mathbf{x}, t)\, da + \int_{\mathcal{B}_t} \mathbf{x}\times\mathbf{b}(\mathbf{x}, t)\, dv. \tag{2.44}$$

Normalising the integrands by taking the material derivative, using the *Cauchy stress* tensor $\boldsymbol{\sigma}$ and utilizing the Gauss' divergence theorem,

$$\int_{\mathcal{B}_t} \left\{\mathbf{x} \times \rho(\mathbf{x}, t)\, \ddot{\mathbf{x}} - \operatorname{div}(\mathbf{x}\times\boldsymbol{\sigma}^T) + \mathbf{x}\times\mathbf{b}(\mathbf{x}, t)\right\}\, dv = \mathbf{0} \tag{2.45}$$

with

$$\operatorname{div}(\mathbf{x}\times\boldsymbol{\sigma}^T) = \operatorname{Grad}\mathbf{x}\times\boldsymbol{\sigma}^T + \mathbf{x}\times\operatorname{div}\boldsymbol{\sigma}^T. \tag{2.46}$$

Simplifying the above, Eq. (2.46) is transformed into:

$$\int_{\mathcal{B}_t} \left\{\mathbf{x} \times \rho(\mathbf{x}, t)\, \ddot{\mathbf{x}} + \boldsymbol{\epsilon} : \boldsymbol{\sigma}^T - \mathbf{x}\times\operatorname{div}\boldsymbol{\sigma}^T - \mathbf{x}\times\mathbf{b}(\mathbf{x}, t)\right\}\, dv = \mathbf{0} \tag{2.47}$$

Since $\mathcal{B}_t$ is arbitrary,

$$\mathbf{x} \times \rho(\mathbf{x}, t)\, \ddot{\mathbf{x}} - \mathbf{x}\times\operatorname{div}\boldsymbol{\sigma}^T - \mathbf{x}\times\mathbf{b}(\mathbf{x}, t) + \boldsymbol{\epsilon} : \boldsymbol{\sigma}^T = \mathbf{0} \tag{2.48}$$

Then, with Eq (2.38), we have:

$$\boldsymbol{\epsilon} : \boldsymbol{\sigma}^T = \mathbf{0} \tag{2.49}$$

showing the symmetric properties of the *Cauchy stress* tensor.

Setting up the Lagrangian form of the above equations,

$$\frac{d}{dt}\int_{\mathcal{B}} \mathbf{x}(\mathbf{X}, t) \times \rho_0\dot{\mathbf{x}}(\mathbf{X}, t)\, dV = \int_{\partial\mathcal{B}} \mathbf{x}(\mathbf{X}, t) \times \mathbf{t}^{(\boldsymbol{n})}(\mathbf{X}, t)\, dA + \int_{\mathcal{B}} \mathbf{x}(\mathbf{X}, t) \times \mathbf{b}(\mathbf{X}, t)\, dV. \tag{2.50}$$

Utilizing the first Piola Kirchhoff stress and using the Gauss Divergence theorem,

$$\int_{\mathcal{B}} \left\{\mathbf{x}(\mathbf{X}, t) \times \rho_0\ddot{\mathbf{x}}(\mathbf{X}, t) - \operatorname{div}\left(\mathbf{x}(\mathbf{X}, t) \times \mathbf{P}\right) - \mathbf{x}(\mathbf{X}, t) \times \mathbf{b}(\mathbf{X}, t)\right\} dV = \mathbf{0} \tag{2.51}$$

Taking the divergence of $(\mathbf{x}(\mathbf{X},t) \times \mathbf{P})$,

$$\int_{\mathcal{B}} \{\mathbf{x}(\mathbf{X},t) \times (\rho_0 \ddot{\mathbf{x}}(\mathbf{X},t) - \mathrm{div}\mathbf{P} - \mathbf{b}(\mathbf{X},t)) - \mathrm{Grad}\,\mathbf{x}(\mathbf{X},t) \times \mathbf{P}\}\, dV = \mathbf{0} \tag{2.52}$$

with Eq (2.42)

$$\int_{\mathcal{B}} \mathbf{F} \times \mathbf{P}\, dV = \mathbf{0}. \tag{2.53}$$

Since the integrand is arbitrary,

$$\mathbf{F} \times \mathbf{P} = \boldsymbol{\epsilon} : \left(\mathbf{F}\mathbf{P}^T\right) = \mathbf{0} \tag{2.54}$$

this time demonstrating the symmetric property of $(\mathbf{F}\mathbf{P})^T$:

$$\mathbf{F}\mathbf{P}^T = \mathbf{P}\mathbf{F}^T. \tag{2.55}$$

As $\mathbf{S} = \mathbf{P}\mathbf{F}^T$, the second Piola-Kirchhoff stress is also symmetric.

2.4 Variational formulation

In the analysis of nonlinear initial value boundary problems, a coupled system of partial differential equations, specifically, the deformation and strain descriptions, local balance laws of momentum and constitutive equations, have to be considered. In cardiac mechanics these relations and the complex geometries they are applied to require computational approximation methods to be employed.

In this research the use of the Element-free Galerkin method which is a so-called mesh free method is utilized. Element-free Galerkin (and the standard Galerkin method) is based on a variational formulation of the governing equations, also known as the principle of virtual work or the weak form.

Consider a nonlinear boundary value problem on domain $\mathcal{B}$ with boundary $\partial\mathcal{B}$. Dirchlet boundary conditions are prescribed $\mathbf{u} = \bar{\mathbf{u}}$ on $\partial\mathcal{B}_D \subset \partial\mathcal{B}$ and Neuman boundary conditions $\mathbf{P}\mathbf{n} = \bar{\mathbf{t}}^{(\mathbf{n})}$ are prescribed on $\mathcal{B}_N \subset \partial\mathcal{B}$ such that

$$\begin{aligned} \partial\mathcal{B}_N \cup \partial\mathcal{B}_D &= \partial\mathcal{B} \\ \partial\mathcal{B}_N \cap \partial\mathcal{B}_D &= \emptyset. \end{aligned}$$

Assuming hyperelastic material behaviour, we let $\rho_0\psi(\mathbf{E})$ define the stored energy function per unit volume as a function of the Green strain tensor, given by Eq. (2.16). The

internal work is often expressed as

$$\mathcal{W}_{int}(\mathbf{u}) = \int_{\mathcal{B}} \rho_0 \frac{\partial \psi(\mathbf{E})}{\partial \mathbf{E}} : \delta\mathbf{E} dV = \int_{\mathcal{B}} \mathbf{S}(\mathbf{u}) : \delta\mathbf{E} dV \tag{2.56}$$

where $\delta\mathbf{E}$ is the variation of the Green strain tensor. Using Eqs. (2.16) and (2.5) allows us to express $\mathbf{S}$ as a function of $\mathbf{u}$.

The variational formulation of continuum mechanics states that the total external work $\mathcal{W}_{ext}$ is equal to the total internal work $\mathcal{W}_{int}$. The external work corresponds to work done by the external forces such as body forces $\mathbf{b}$ acting over the volume of the body and prescribed traction forces $\bar{\mathbf{t}}^{(\mathbf{n})}$ acting on the surface of the body. The external work is given by

$$\mathcal{W}_{ext}(\mathbf{u}) = \int_{\mathcal{B}} \rho_0 \mathbf{b} \cdot \delta\mathbf{u} dV + \int_{\partial\mathcal{B}_N} \bar{\mathbf{t}}^{(\mathbf{n})} \cdot \delta\mathbf{u} dA \tag{2.57}$$

where ρ_0 is the density in the reference configuration, $\mathbf{b}$ is the body force, $\bar{\mathbf{t}}^{(\mathbf{n})}$ is the traction acting on the *Neuman* boundary surface $\partial\mathcal{B}_N$ with unit normal vector $\mathbf{n}$ and $\delta\mathbf{u}$ is the variation of displacement. The full variational formulation is

$$\begin{aligned} \delta\Psi(\mathbf{u}) &= \mathcal{W}_{int} - \mathcal{W}_{ext} = 0 \\ &= \int_{\mathcal{B}} \mathbf{S} : \delta\mathbf{E} dV - \int_{\mathcal{B}} \rho_0 \mathbf{b} \cdot \delta\mathbf{u} dV - \int_{\partial\mathcal{B}_N} \bar{\mathbf{t}}^{(\mathbf{n})} \cdot \delta\mathbf{u} dA \end{aligned} \tag{2.58}$$

where $\mathbf{u} = \bar{\mathbf{u}}$ on $\partial\mathcal{B}_D$. It can be shown that the fulfilment of the variational form satisfies the governing equations with the same boundary conditions. For more details on the variational form one is directed to Holzapfel [59], Bonet and Wood [12] and Wriggers [156].

2.5 Constitutive laws

Constitutive laws allow us to describe the relationship between stresses within a body $\mathcal{B}$ to specified strain measures. Formulation of constitutive laws depend on the material under consideration, allowable deformations (i.e incompressibility) and certain physical principles (i.e frame invariances). For most materials undergoing small strain deformations it is appropriate to approximate the stresses as a linear function of the strain. However, this assumption is not applicable to cardiac mechanics, where the material undergoes significant deformation.

Hyperelastic material descriptions begin with the formulation of an elastic potential Ψ. From this elastic potential, or strain energy function, we derive the stresses and consequent constitutive law of our material. It is convenient to define the strain energy

function in terms of the principal invariants of **E**. The principal invariants of a tensor are scalars quantities that remain constant for any orthogonal coordinate transformation. The second order tensor **E** contains three independent invariants

$$I_1^{\mathrm{E}} = \mathrm{tr}(\mathbf{E}) \tag{2.59}$$

$$I_2^{\mathrm{E}} = \frac{1}{2}\left[(\mathrm{tr}\mathbf{E})^2 - \mathrm{tr}(\mathbf{E}^2)\right] \tag{2.60}$$

$$I_3^{\mathrm{E}} = \det(\mathbf{E}). \tag{2.61}$$

It should be noted that I_3^{E} will be a function of the Jacobian J as well as the other two invariants, and as such can be included in constitutive relations as a means to enforce incompressibility via a penalty relation.

2.5.1 Isotropy

An isotropic material is a material where the material properties are independent of the direction in which they are measured. Consider the *St. Venant-Kirchhoff* model, which is defined by the strain energy function

$$\Psi(\mathbf{E}) = \frac{1}{2}\lambda \mathrm{tr}(\mathbf{E})^2 + \mu \mathrm{tr}(\mathbf{E}^2), \tag{2.62}$$

where λ and μ are the *Lamè* parameters which characterise the material response. Using the second part of Eq. (2.56) we can derive second *Piola-Kirchhoff* stress tensor as

$$\mathbf{S} = \frac{\partial \Psi(\mathbf{E})}{\partial \mathbf{E}} = \lambda \mathrm{tr}(\mathbf{E})\mathbf{1} + 2\mu\mathbf{E}. \tag{2.63}$$

The material fourth order elasticity tensor $\overset{4}{\boldsymbol{\mathcal{C}}}$ is defined by the partial derivative of the second *Piola-Kirchhoff* stress tensor with respect to Green strain

$$\overset{4}{\boldsymbol{\mathcal{C}}} = \frac{\partial \mathbf{S}}{\partial \mathbf{E}}, \tag{2.64}$$

which for the *St. Venant-Kirchhoff* material is conveniently expressed in index notation as

$$\overset{4}{\mathcal{C}}_{ijkl} = \frac{\partial \mathrm{S_{ij}}}{\partial \mathrm{E_{kl}}} = \lambda \delta_{ij}\delta_{kl} + \mu(\delta_{ik}\delta_{jl} + \delta_{il}\delta_{jk}) \tag{2.65}$$

Making use of Eqs. (2.59) and (2.60) it is possible to construct the *St. Venant-Kirchhoff* strain energy function in terms of the invariants of **E**. This is given as

$$\Psi(I_1^{\mathrm{E}}, I_2^{\mathrm{E}}, I_3^{\mathrm{E}}) = \frac{1}{2} I_1^{\mathrm{E}^2} (\lambda + \mu) - \mu I_2^{\mathrm{E}}, \tag{2.66}$$

which by definition ensures the condition of isotropy. Using the chain rule one can compose $\mathbf{S}$ in the general sense as

$$\mathbf{S}(I_1^{\mathrm{E}}, I_2^{\mathrm{E}}, I_3^{\mathrm{E}}) = \sum_{i=1}^{3} \rho_0 \frac{\partial \psi(I_1^{\mathrm{E}}, I_2^{\mathrm{E}}, I_3^{\mathrm{E}})}{\partial I_i^{\mathrm{E}}} \frac{I_i^{\mathrm{E}}}{\partial \mathbf{E}}. \tag{2.67}$$

$\overset{4}{\boldsymbol{\mathcal{C}}}$ can be derived in a similar manner.

2.5.2 Transverse isotropy

Materials that exhibit different deformation properties depending on the material direction are called anisotropic. The simplest case and often the first step in modelling anisotropy is transverse isotropy; the case where the material behaviour in a certain preferred direction is different from the bulk material. In the transverse plane orthogonal to this preferred direction, the material behaves in an isotropic manner. A simple applicable case is an isotropic material reinforced with uniform cylindrical fibres.

To mathematically describe transverse isotropy we introduce $\mathbf{V}_f$ to denote a co-variant vector in fibre direction and $\hat{\mathbf{V}}_f$ its contra-variant equivalent. Following the work of Klinkel et al. [74], we define a structural tensor representing the one dimensional fibre continuum as

$$\mathbf{M}_f = \mathbf{V}_f \otimes \hat{\mathbf{V}}_f. \tag{2.68}$$

Strain energy function that exhibit transverse isotropy require additional invariants to accurately represent the fibre reinforcement in the preferred direction $\mathbf{V}_f$. This is achieved by introducing two additional *fibre* invariants given by:

$$I_{4f}^{\mathrm{E}} = \mathrm{tr}(\mathbf{M}_f \mathbf{E}) \tag{2.69}$$

$$I_{5f}^{\mathrm{E}} = \mathrm{tr}(\mathbf{M}_f \mathbf{E}^2). \tag{2.70}$$

The inclusion of these invariants into the strain energy function (with additional material parameters) fulfil any requirements to describe transverse isotropy. The second *Piola-Kirchhoff* stress tensor is consequently derived as

$$\mathbf{S}(I_1^{\mathrm{E}}, I_2^{\mathrm{E}}, I_3^{\mathrm{E}}, I_{4f}^{\mathrm{E}}, I_{5f}^{\mathrm{E}}) = \sum_{i=1}^{5} \rho_0 \frac{\partial \psi(I_1^{\mathrm{E}}, I_2^{\mathrm{E}}, I_3^{\mathrm{E}}, I_{4f}^{\mathrm{E}}, I_{5f}^{\mathrm{E}})}{\partial I_i^{\mathrm{E}}} \frac{I_i^{\mathrm{E}}}{\partial \mathbf{E}}. \tag{2.71}$$

2.5.3 Orthotropy

For an orthotropic material with three orthonormal material co-variant directions $\mathbf{V}_f$, $\mathbf{V}_t$ and $\mathbf{V}_n$ we can define additional structural tensors as

$$\mathbf{M}_t = \mathbf{V}_t \otimes \hat{\mathbf{V}}_t \tag{2.72}$$

$$\mathbf{M}_n = \mathbf{V}_n \otimes \hat{\mathbf{V}}_n. \tag{2.73}$$

Where $\hat{\mathbf{V}}_f$, $\hat{\mathbf{V}}_t$ and $\hat{\mathbf{V}}_n$ are the corresponding contra-variant vectors. This allows us to compose additional strain invariants relating to these material directions. These are introduced as

$$I_{4t}^{\mathrm{E}} = \mathrm{tr}(\mathbf{M}_t\mathbf{E}) \tag{2.74}$$

$$I_{5t}^{\mathrm{E}} = \mathrm{tr}(\mathbf{M}_t\mathbf{E}^2) \tag{2.75}$$

$$I_{4n}^{\mathrm{E}} = \mathrm{tr}(\mathbf{M}_n\mathbf{E}) \tag{2.76}$$

$$I_{5n}^{\mathrm{E}} = \mathrm{tr}(\mathbf{M}_n\mathbf{E}^2). \tag{2.77}$$

Note that

$$\sum_{i=f,t,n} I_{4i}^{\mathrm{E}} = \mathbf{E} : (\mathbf{M}_f + \mathbf{M}_t + \mathbf{M}_n) = \mathbf{E} : \mathbf{1} = I_1^{\mathrm{E}}, \tag{2.78}$$

making only three of the invariants I_{4f}^{E}, I_{4t}^{E}, I_{4n}^{E} and I_1^{E} independent.

This allows us to describe an orthotropic material via the use of nine independent strain invariants or seven in the case of incompressibility where $J = 1$. Another approach is to express the strain energy function in terms of the local material directions directly. The required basis transformation needed to achieve this will be dealt with in detail in Chapter 4. Each strain component of the local Green strain tensor can be associated with the orthonormal basis $(\mathbf{V}_f, \mathbf{V}_t, \mathbf{V}_n)$ such that

$$\begin{aligned}\mathbf{E} =& E_{ff}\mathbf{V}_f \otimes \hat{\mathbf{V}}_f + E_{tt}\mathbf{V}_t \otimes \hat{\mathbf{V}}_t + E_{nn}\mathbf{V}_n \otimes \hat{\mathbf{V}}_n + E_{ft}(\mathbf{V}_f \otimes \hat{\mathbf{V}}_t + \mathbf{V}_t \otimes \hat{\mathbf{V}}_f) \\ &+ E_{fn}(\mathbf{V}_f \otimes \hat{\mathbf{V}}_n + \mathbf{V}_n \otimes \hat{\mathbf{V}}_f) + E_{tn}(\mathbf{V}_t \otimes \hat{\mathbf{V}}_n + \mathbf{V}_n \otimes \hat{\mathbf{V}}_t).\end{aligned} \tag{2.79}$$

Where the symmetry of the Green strain tensor is utilized in the formulation. As an example, the orthotropic strain energy function for cardiac tissue used in Usyk et al. [147] is expressed as

$$\Psi = \frac{1}{2}A\left(e^Q - 1\right),$$

with $Q = b_{ff}E_{ff}^2 + b_{nn}E_{nn}^2 + b_{tt}E_{tt}^2 + b_{tn}(E_{nt}^2 + E_{tn}^2) + b_{ft}(E_{ft}^2 + E_{tf}^2) + b_{fn}(E_{fn}^2 + E_{nf}^2)$. The material stiffness parameters b_{ij} govern the anisotropy, while A is used as global stress scaling factor to assist in calibrating the material to experimental results.

Chapter 3

Three dimensional *Cosserat* continuum

3.1 Overview

The *Cosserat* continuum falls under the family of generalized continuum mechanics classified as micropolar continua, defined by Eringen [35]. Micropolar continua are characterized by the additional degrees of freedom that each material point inherits, independent of the classical displacement field. The field of study originated with the work of the Cosserat brothers, *Théorie des corps déformables* (1909) [25], and was developed and popularized in the the mid 1960s.

The following derivations rely heavy on the works of Sansour [120, 122, 123] and Skatulla [121, 131, 132].

3.2 Deformation and strain measures

In the classical *Cosserat* continuum every material point P is assigned a rotational field independent of displacements [120], enriching the continuum with additional degrees of freedom. Furthermore, whereas classical continua can be described by one strain measure, i.e. by the stretch tensor, the *Cosserat* continuum requires, due to the independent rotation field, a second strain measure. Consider $\mathbf{R} \in SO(3)$ where $SO(3)$ is defined as

$$SO(3) = \{\mathbf{R} \in \mathbb{R}^3 | \mathbf{R}^T\mathbf{R} = \mathbf{1}, \text{ and } \det(\mathbf{R}) = 1\} \tag{3.1}$$

We start with an explicit expression for the rotational field $\mathbf{R}$, based on the Rodrigues equation [121]:

$$\mathbf{R}(\vartheta^i, t) = 1 + \frac{\sin|\boldsymbol{\gamma}|}{|\boldsymbol{\gamma}|}\boldsymbol{\Gamma} + \frac{\cos|\boldsymbol{\gamma}|}{|\boldsymbol{\gamma}|^2}\boldsymbol{\Gamma}^2 \tag{3.2}$$

where $\boldsymbol{\gamma}$ denotes the rotation vector and $\boldsymbol{\Gamma}(\vartheta^i, t) \in so(3)$ is a skew symmetric tensor with $\boldsymbol{\gamma}$ as its axial vector. Here $so(3)$ is defined as the corresponding *lie algebra* of the *lie group* $SO(3)$.

The *Cosserat* continuum features two strain measures. The first *Cosserat* strain tensor is a stretch-like tensor given by:

$$\mathbf{U}(\vartheta^i, t) = \mathbf{R}^T\mathbf{F} \tag{3.3}$$

where it should be noted, that unlike it's classical counterpart, is not symmetric in general. The second *Cosserat* strain measure is a change of curvature strain tensor given by:

$$\mathbf{K}(\vartheta^i, t) = -\frac{1}{2}\boldsymbol{\epsilon} : (\mathbf{R}^T\mathbf{R}_{,i}) \otimes \mathbf{G}^i \tag{3.4}$$

Considering $\mathbf{R} \in SO(3)$, it holds that $\mathbf{R}^T\mathbf{R} = \mathbf{1}$ and further that the derivative $\mathbf{R}^T_{,i}\mathbf{R} + \mathbf{R}^T\mathbf{R}_{,i} = \mathbf{0}$. This implies that that the tensor product $\mathbf{R}^T_{,i}\mathbf{R}$ is skew symmetric and an axial vector $\mathbf{k}_i$ exists such that

$$\mathbf{k}_i(\vartheta^i, t) = \text{axial}(\mathbf{R}^T\mathbf{R}_{,i}) = -\frac{1}{2}\boldsymbol{\epsilon} : (\mathbf{R}^T\mathbf{R}_{,i}), \tag{3.5}$$

where $\boldsymbol{\epsilon}$ is the permutation tensor. This allows us to express Eq. (3.4) as

$$\mathbf{K}(\vartheta^i, t) = \mathbf{k}_i \otimes \mathbf{G}^i \tag{3.6}$$

Variants of the *Cosserat* strains

Following the work Sansour and Skatulla [121], the variation of $\mathbf{U}$ is expressed as:

$$\begin{aligned}\delta\mathbf{U} &= -\mathbf{R}^T\mathbf{W}\mathbf{F} + \mathbf{R}^T\delta\mathbf{F} \\ &= -\mathbf{R}^T\mathbf{W}\mathbf{F} + \mathbf{R}^T\delta\mathbf{u}_{,i} \otimes \mathbf{G}^i\end{aligned} \tag{3.7}$$

Note that variations of rotations are not only multiplicative, but for the quasi-static case we only consider the so called *left group action* $\mathbf{W}$, which is skew-symmetric. We are able to express $\delta\mathbf{K}$ through it's axial vector $\mathbf{k}$ in a similar manner to how we obtained Eq. (3.7) as

$$\delta\mathbf{k}_i = \text{axial}\{\delta(\mathbf{R}^T\mathbf{R}_{,i})\} = \mathbf{R}^T\mathbf{w}_{,i} \ . \tag{3.8}$$

Where $\mathbf{w}$ is the axial vector of $\mathbf{W}$.

3.3 Variational formulation

We look at establishing a strain energy function as a function of the two *Cosserat* strain measures [121]. The stored strain energy per unit volume is the defined as:

$$\rho_0 \psi(\mathbf{U}, \mathbf{K}) \tag{3.9}$$

Where hyperelastic material behaviour is assumed, ρ_0 is the density in the reference configuration and l the so called *characteristic length* is included in the formulation of ψ, as the contributions from $\mathbf{K}$ are associated with l. The incorporation of l into the stored energy functions is commonly achieved by integrating over the micro-continuum within the limits $\left[-\frac{l}{2}, \frac{l}{2}\right]$, producing an additional multiplicative term $\frac{l^2}{12}$.

This allows us to express the internal work of the system as:

$$\mathcal{W}_{int} = \int_{\mathcal{B}} \left\{ \rho_0 \frac{\partial \psi(\mathbf{U}, \mathbf{K})}{\partial \mathbf{U}} : \delta \mathbf{U} + \rho_0 \frac{\partial \psi(\mathbf{U}, \mathbf{K})}{\partial \mathbf{K}} : \delta \mathbf{K} \right\} dV \tag{3.10}$$

$$\mathcal{W}_{int} = \int_{\mathcal{B}} \left\{ \boldsymbol{n} : \delta \mathbf{U} + \boldsymbol{m} : \delta \mathbf{K} \right\} dV \tag{3.11}$$

Where $\boldsymbol{n} = \rho_0 \frac{\partial \psi}{\partial \mathbf{U}}$, the force stress tensor, and $\boldsymbol{m} = \rho_0 \frac{\partial \psi}{\partial \mathbf{K}}$, the couple stress tensor, are work conjugate to $\mathbf{U}$ and $\mathbf{K}$, respectively.

Corresponding to internal virtual potential we define $\mathcal{W}_{ext}$ as the external virtual work, the source of which are the external forces acting on the body. The external work is given as

$$\mathcal{W}_{ext} = \int_{\mathcal{B}} \rho_0 \mathbf{b} \cdot \delta \mathbf{u} \; dV + \int_{\mathcal{B}} \rho_0 \mathbf{l} \cdot \mathbf{w} \; dV + \int_{\partial \mathcal{B}_N} \bar{\mathbf{t}}^{(\mathbf{n})} \cdot \delta \mathbf{u} \; dA + \int_{\partial \mathcal{B}_N} \bar{\mathbf{q}}^{(\mathbf{n})} \cdot \mathbf{w} \; dA \tag{3.12}$$

Where $\mathbf{b}$ and $\mathbf{l}$ are the external body force and torque respectively. The corresponding quantities on the boundary are given by $\mathbf{t}^{(\mathbf{n})}$ and $\mathbf{q}^{(\mathbf{n})}$. The vector $\mathbf{w}$ is work conjugate to the external torque.

For the static case, the *first law of thermodynamics* provides the following variational statement

$$\delta \Psi(\mathbf{U}, \mathbf{K}) = \mathcal{W}_{int} - \mathcal{W}_{ext} = 0. \tag{3.13}$$

Now, considering Eqs. (3.7) and (3.4), we can compose the internal work Eq. (3.11) as:

$$\begin{aligned}\mathcal{W}_{int} &= \int_{\mathcal{B}} \left\{ \mathbf{R}\boldsymbol{n} : (\delta\mathbf{u}_{,i} \otimes \mathbf{G}^i - \mathbf{W}\mathbf{F}) + \mathbf{R}\boldsymbol{m} : \mathbf{w}_{,i} \otimes \mathbf{G}^i \right\} \, dV \\ &= \int_{\mathcal{B}} \left\{ \mathbf{R}\boldsymbol{n}\mathbf{G}^i \cdot \delta\mathbf{u}_{,i} - \mathbf{R}\boldsymbol{n}\mathbf{F}^T : \mathbf{W} + \mathbf{R}\boldsymbol{m}\mathbf{G}^i \cdot \mathbf{w}_{,i} \right\} \, dV. \end{aligned} \tag{3.14}$$

Further simplifications can be made on the term containing the skew symmetric tensor $\mathbf{W}$, noticing that

$$\begin{aligned}\mathbf{R}\boldsymbol{n}\mathbf{F}^T : \mathbf{W} &= \mathbf{R}\boldsymbol{n}\mathbf{G}^i \otimes \mathbf{x}_{,i} : \mathbf{W} = \mathbf{R}\boldsymbol{n}\mathbf{G}^i : \mathbf{W}\mathbf{x}_{,i} = \mathbf{R}\boldsymbol{n}\mathbf{G}^i \cdot \mathbf{w} \times \mathbf{x}_{,i} \\ &= \mathbf{x}_{,i} \times \mathbf{R}\boldsymbol{n}\mathbf{G}^i \cdot \mathbf{w} \ , \end{aligned} \tag{3.15}$$

allowing us to write the variational statement as

$$\int_{\mathcal{B}} \mathbf{R}\boldsymbol{n}\mathbf{G}^i \cdot \delta\mathbf{u}_{,i} \, dV - \int_{\mathcal{B}} \mathbf{x}_{,i} \times \mathbf{R}\boldsymbol{n}\mathbf{G}^i \cdot \mathbf{w} \, dV + \int_{\mathcal{B}} \mathbf{R}\boldsymbol{m}\mathbf{G}^i \cdot \mathbf{w}_{,i} \, dV - \mathcal{W}_{ext} = 0 \tag{3.16}$$

We apply *Gauss's divergence theorem* to the terms containing $\delta\mathbf{u}_{,i}$ and $\mathbf{w}_{,i}$. This gives us the full expression for the variational formulation in terms of virtual displacement $\delta\mathbf{u}$ and virtual rotation $\mathbf{w}$, expressed as

$$\begin{aligned} &- \int_{\mathcal{B}} \frac{1}{\sqrt{G}} (\sqrt{G}\mathbf{R}\boldsymbol{n}\mathbf{G}^i)_{,i} \cdot \delta\mathbf{u} \, dV + \int_{\partial\mathcal{B}} \mathbf{R}\boldsymbol{n}\mathbf{n} \cdot \delta\mathbf{u} \, dA - \int_{\mathcal{B}} \mathbf{x}_{,i} \times \mathbf{R}\boldsymbol{n}\mathbf{G}^i \cdot \mathbf{w} \, dV \\ &- \int_{\mathcal{B}} \frac{1}{\sqrt{G}} (\sqrt{G}\mathbf{R}\boldsymbol{m}\mathbf{G}^i)_{,i} \cdot \mathbf{w} \, dV + \int_{\partial\mathcal{B}} \mathbf{R}\boldsymbol{m}\mathbf{n} \cdot \mathbf{w} \, dA - \mathcal{W}_{ext} = 0. \end{aligned} \tag{3.17}$$

Where G is the determinant of the *Riemannian* metric coefficient given in Eq. (2.7). Due to $\delta\mathbf{u}$ and $\mathbf{w}$ being arbitrary (the variational from must be valid for any choice of $\delta\mathbf{u}$ and $\mathbf{w}$), the local statements of the governing equations can be expressed directly from Eq. (3.17) as

$$\frac{1}{\sqrt{G}} (\sqrt{G}\mathbf{R}\boldsymbol{n}\mathbf{G}^i)_{,i} + \rho_0\mathbf{b} = \mathbf{0} \quad \text{in } \mathcal{B} \tag{3.18}$$

$$\mathbf{x}_{,i} \times \mathbf{R}\boldsymbol{n}\mathbf{G}^i + \frac{1}{\sqrt{G}} (\sqrt{G}\mathbf{R}\boldsymbol{m}\mathbf{G}^i)_{,i} + \rho_0\mathbf{l} = \mathbf{0} \quad \text{in } \mathcal{B} \ . \tag{3.19}$$

The accompanying Neuman boundary conditions are given as

$$\mathbf{R}\boldsymbol{n}\mathbf{n} = \bar{\mathbf{t}}^{(\mathbf{n})} \qquad \text{and} \qquad \mathbf{R}\boldsymbol{m}\mathbf{n} = \bar{\mathbf{q}}^{(\mathbf{n})} \ , \quad \text{on } \partial\mathcal{B}_N \ ,$$

and the Dirchlet boundary conditions as $\mathbf{u} = \bar{\mathbf{u}}$ and $\boldsymbol{\gamma} = \bar{\boldsymbol{\gamma}}$ on $\partial\mathcal{B}_D$.

3.3.1 Stress measures

Following the work of Sansour [120], we define a moment tensor, also known as the couple stress tensor, $\boldsymbol{\xi}$ which is expected to satisfy the *Cauchy* lemma with respect to external moments. The couple stress tensor $\boldsymbol{\xi}$ and the *Cauchy* stress tensor $\boldsymbol{\sigma}$ can be cast into material setting, by defining the following isometric material stress and moment tensors

$$\boldsymbol{\Sigma} = \frac{\rho_0}{\rho}\mathbf{R}^T\boldsymbol{\sigma}\mathbf{R} \qquad \text{and} \qquad \boldsymbol{\Xi} = \frac{\rho_0}{\rho}\mathbf{R}^T\boldsymbol{\xi}\mathbf{R}. \tag{3.20}$$

These material stress measure can be related to the previously introduced force stress tensor $\boldsymbol{n}$ and couple stress tensor $\boldsymbol{m}$ [120]. This is given by

$$\boldsymbol{\Sigma} = \boldsymbol{n}\mathbf{U}^T \qquad \text{and} \qquad \boldsymbol{\Xi} = \boldsymbol{m}\mathbf{U}^T. \tag{3.21}$$

Combining Eqs. (3.20) and (3.21) yields

$$\boldsymbol{\sigma} = J\mathbf{R}\boldsymbol{n}\mathbf{U}^T\mathbf{R}^T \qquad \text{and} \qquad \boldsymbol{\xi} = J\mathbf{R}\boldsymbol{m}\mathbf{U}^T\mathbf{R}^T. \tag{3.22}$$

Where J is the Jacobian defined in Eq. (2.4). This allows us to express the force stress and couple stress state of the problem in terms of the current configuration.

Cartesian systems

In the case of a Cartesian coordinates system the following simplifications can be made:

$$\mathbf{G}_i = \mathbf{G}^i = \mathbf{e}_i \qquad \text{with} \qquad \vartheta^i = X_i. \tag{3.23}$$

Furthermore, the determinant of the *Riemannian* metric coefficient, $G = 1$.

Chapter 4

One dimensional *Cosserat* Fibre

4.1 Main objective

Imposing the *Cosserat* continuum theory on a one dimensional space would produce a one dimensional continuum, a so-called "Cosserat rod", with a rotational field independent to the conventional displacement field. Modelling isolated fibres and fibre reinforced continua has already been achieved with great success [39, 93, 103]. There has even been some recent application of a one dimensional *Cosserat* rod theory in computer animations and visualization software [102, 135]. However, the application of the *Cosserat* continuum has yet to be applied to biological soft tissue, specifically with regards to cardiac mechanics.

By considering a fibre bundle as a *Cosserat* rod we are able to consider material stiffness parameters relating to the change of curvature strains of one dimensional rod theory directly in the material laws. The ability to explicitly account for torsion and bending in the constitutive law gives this approach a natural advantage over classical formulations. Moreover, the additional degrees of freedom in the kinematic description allow for more complex, realistic deformations. The scaling of the contributions are ultimately determined by a length scale parameter, l. Physically one could consider this as a measure of the cross sectional diameter of the fibre, but it is more accurately considered as a mathematical weighting of the micro space and is not necessarily limited to the dimensions of the micro structure's physiology.

As illustrated in Figure 4.1, a *Cosserat* rod can experience axial, shear, torsional and bending deformations, each of these associated to the material stiffness parameters corresponding to Youngs modulus, E, Shear modulus, G, and the second moments of inertia for torsion, I_1 and bending, I_2, respectively.

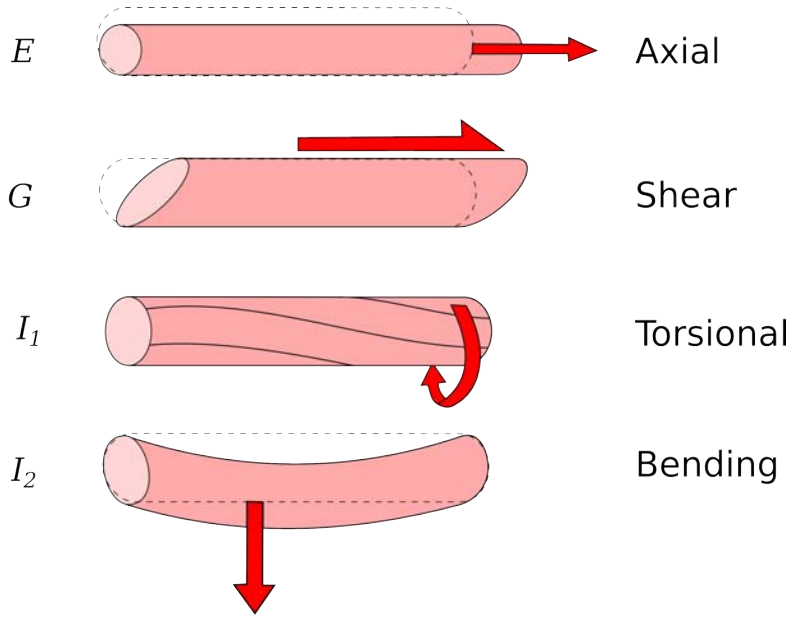

FIGURE 4.1: Various deformation modes of a one dimensional *Cosserat* rod.

It is our hope that the application of *Cosserat* theory to cardiac mechanics will help capture more realistic deformations of the cardiac tissue and the left ventricle as a whole while undergoing cardiac function.

4.2 Fibre local coordinates

In the same manner as Costa et al. [26], Usyk et al. [147] and Kerckhoffs [72] a local orthonormal coordinate system $\{\mathbf{V}_f, \mathbf{V}_t, \mathbf{V}_n\}$ describes fibre orientation, sheet-tangent direction and sheet-normal direction, respectively. This is consistent to the schematic in Figure 1.1. In this sense a specific entry in a higher order tensor can be referred to by the fibre local components (i.e shear strain in the the plane normal to the fibre in the direction of the sheet would correspond to the entry U_{ft}).

4.3 Cosserat measures of a one dimensional rod

Consider a one dimensional fibre continuum mapped by the coordinate $s = s(\vartheta^i)$. As such the fibre is assumed to be embedded in three dimensional space. The fibre deformation gradient is given by:

$$\mathbf{F}^{(s)} = \frac{\partial \mathbf{x}}{\partial \vartheta^i} \frac{\partial \vartheta^i}{\partial s} \otimes \hat{\mathbf{V}}_f = \mathbf{v}_f \otimes \hat{\mathbf{V}}_f \tag{4.1}$$

where $\mathbf{V}_f$ denotes a co-variant vector in fibre direction and $\hat{\mathbf{V}}_f$ its contra-variant equivalent. The fibre direction in the current configuration is expressed by $\mathbf{v}_f = \mathbf{F}\mathbf{V}_f$. In this sense, $\mathbf{F}^{(s)}$ is the projection of the deformation gradient $\mathbf{F}$ in direction of the fibre. Making use of the structural tensor introduced in Eq. (2.68) allows us to alternatively express $\mathbf{F}^{(s)} = \mathbf{F}\mathbf{M}_f$ [74]. Similarly, we find associated strain measures $\mathbf{U}^{(s)}$ and $\mathbf{K}^{(s)}$, respectively, for the *Cosserat* fibre continuum:

$$\begin{aligned}
\mathbf{U}^{(s)} = & \quad \mathbf{R}^T\mathbf{F}^{(s)} & = U_{ff}\mathbf{V}_f \otimes \hat{\mathbf{V}}_f + U_{tf}\mathbf{V}_t \otimes \hat{\mathbf{V}}_f + U_{nf}\mathbf{V}_n \otimes \hat{\mathbf{V}}_f \\
\mathbf{K}^{(s)} = & \quad -\tfrac{1}{2}\,\epsilon : \mathbf{R}^T \frac{\partial \mathbf{R}}{\partial \vartheta^i}\frac{\partial \vartheta^i}{\partial s} \otimes \hat{\mathbf{V}}_f & = K_{ff}\mathbf{V}_f \otimes \hat{\mathbf{V}}_f + K_{tf}\mathbf{V}_t \otimes \hat{\mathbf{V}}_f + K_{nf}\mathbf{V}_n \otimes \hat{\mathbf{V}}_f
\end{aligned}$$

4.4 Variational formulation

Following the same approach outlined in the previous chapter, we look at establishing a stored strain energy function for the the one dimensional fibre bundle ψ_{fibre} as a function of the two *Cosserat* fibre strain measures

$$\psi_{fibre}(\mathbf{U}^{(s)}, \mathbf{K}^{(s)}). \tag{4.2}$$

where hyperelastic material behaviour is assumed and l, the so called *characteristic length* of the underlying micro structure is associated with $\mathbf{K}^{(s)}$. This allows us to express a variational principle as

$$\delta\Psi_{fibre} = \int_{\mathcal{B}} \left\{ \boldsymbol{n}^{(s)} : \delta\mathbf{U}^{(s)} + \boldsymbol{m}^{(s)} : \delta\mathbf{K}^{(s)} \right\} \mathrm{d}V - W_{ext} = 0. \tag{4.3}$$

The force stress tensor, $\boldsymbol{n}^{(s)}$ and the couple stress tensor, $\boldsymbol{m}^{(s)}$ for the fibre bundle are work conjugate to $\mathbf{U}^{(s)}$ and $\mathbf{K}^{(s)}$ respectively. They are expressed as

$$\begin{aligned}
\boldsymbol{n}^{(s)} &= \frac{\partial \psi}{\partial \mathbf{U}^{(s)}} \\
\boldsymbol{m}^{(s)} &= \frac{\partial \psi}{\partial \mathbf{K}^{(s)}}.
\end{aligned}$$

Chapter 5

Constitutive model development

Developing the constitutive model has been a key research area of this study. The constitutive model governs the material response to external stimuli of the computational model. How to best reflect the physiological material response of cardiac tissue, in a meaningful, accurate and reasoned manner is addressed in this chapter.

Mathematical representations of the one dimensional fibre bundle and the accompanying extracellular matrix (ECM), together with the various stages of the constitutive model development are presented in the following sections. Meaningful experiments and results that inform some of the developmental steps may be referred to here, but will be presented in full in Chapter 7.

5.1 Overview: one dimensional *Cosserat* fibre embedded in a three dimensional matrix

The one dimensional *Cosserat* rod cannot provide a fully meaningful description for a three dimensional continuum on its own. A trivial investigation into this would show that the resulting fourth order tangent stiffness tensors would violate the positive definiteness requirement needed to solve the system of equations. Additionally the physical description of cardiac tissue is complex and would be improperly simplified by a one dimensional representation. The myocardium is often described as a sum of its main components, i.e a combination of myocytes which accounts for two thirds of the material volume and an extracellular matrix which accounts for the remaining third [22]. Subsequently, the inclusion of the ECM in constitutive development is essential as it plays a significant role in the mechanics of the problem [43]. The ECM has various components, most notably collagen (85% of which are type I, 11% type III and 3% type V) [20] which

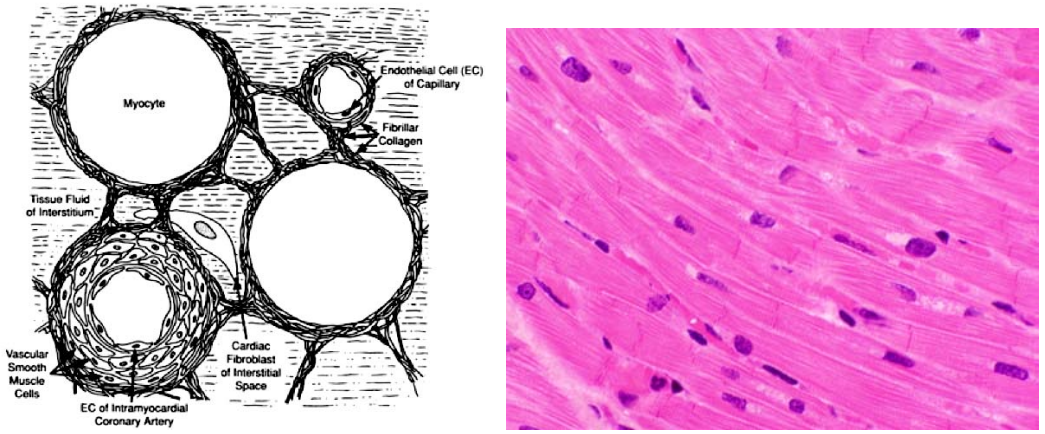

(a) Schematic of a highly magnified, cross sectional view of cardiac tissue

(b) Rat cardiac tissue, stained with Hematoxylin and Eosin at 400x magnification.

FIGURE 5.1: The bulk of myocardium tissue is composed of striated myocytes, surrounded in an extracellular matrix. Figure (a) is reproduced from [152] and Figure (b) from [19].

are responsible for the structural support and contributes to the mechanical stiffness of the problem. Other components include elastin, fibroblasts, plasma cells, endothelial cells, smooth muscle cells, the coronary capillaries and proteins [153] [68]. The approach of this research is to consider the components under two main categories:

1. The fibrous structure: composed of a bundle of myocytes bound by perimysial collagen fibres, which are anisotropic.

2. The complementary connective tissue: made up from remaining components of the ECM, which will be considered isotropic.

For brevity these will be referred to as fibre bundles and the ECM in the subsequent model development. The first concern in the constitutive model development was on the

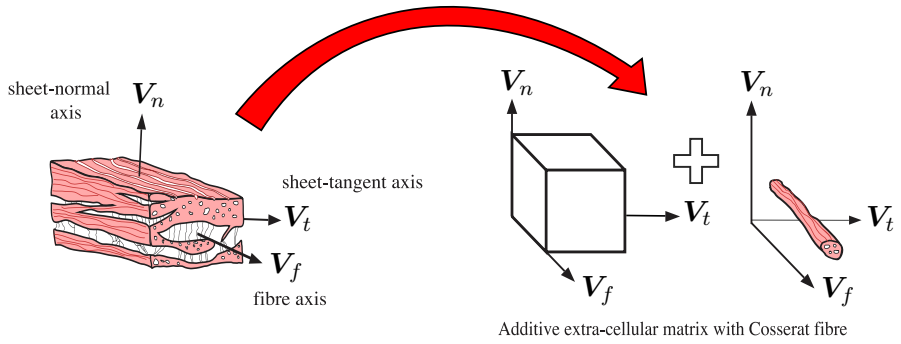

FIGURE 5.2: The main objective of the constitutive model is to take the cardiac specimen and create a mathematical representation. In this case we consider contributions from a three dimensional ECM and a fibre bundle

method chosen to combine the influences from these two components. Two approaches have been chosen, each with their own advantages. First chosen was a homogenization approach, in which stress contributions from the ECM and the fibre are allowed to overlap. Both constituents have stiffness parameters along fibre directions and their contributions to the stress tensors $\boldsymbol{n}$ and $\boldsymbol{m}$ are weighted through the use of volume fractions.

The second approach, and the one most used this study, is a direct (or invariant) approach that does not utilize homogenization. The contributions from the ECM are limited to exclude the stress contributions from the fibre. In this sense the fibre is fully responsible for stress in the fibre directions n_{ff}, n_{tf}, n_{nf} and the ECM experiences the remaining bulk behaviour. We can express the collection of ECM strains as $\mathbf{U}^{(m)} = \mathbf{U} \setminus \mathbf{U}^{(s)}$ which results in

$$\begin{aligned} \mathbf{U}^{(m)} \;=\; & U_{tt}\mathbf{V}_t \otimes \hat{\mathbf{V}}_t \;+\; U_{nn}\mathbf{V}_n \otimes \hat{\mathbf{V}}_n \;+\; U_{ft}\mathbf{V}_f \otimes \hat{\mathbf{V}}_t \\ & + U_{fn}\mathbf{V}_f \otimes \hat{\mathbf{V}}_n \;+\; U_{tn}\mathbf{V}_t \otimes \hat{\mathbf{V}}_n \;+\; U_{nt}\mathbf{V}_n \otimes \hat{\mathbf{V}}_t. \end{aligned} \tag{5.1}$$

This allows for the exclusion of volume fractions, as they are rendered unnecessary and thereby reducing the number of material parameters needed to calibrate.

5.2 Linear-elastic stored energy formulation

The first approach to modelling cardiac tissue was to employ a fully linear constitutive law. This would mean that the fibre and ECM would both be governed by linear relationships between stress and strain. Under the assumption of hyperelastic material behaviour this would require a strain energy function that would produce linearly composed stress tensors upon differentiation.

We establish an additive stored energy function $\psi(\mathbf{U}, \mathbf{K})$ with separate contributions from the fibre, the ECM and a penalty term that enforces the incompressibility

$$\psi = \psi_{fibre}(\mathbf{U}^{(s)}, \mathbf{K}^{(s)}) + \psi_{ECM}(\mathbf{U}^{(m)}) + A_{comp}\,(J\,\ln J - J + 1)\,. \tag{5.2}$$

A_{comp} is the scaling parameter that enforces incompressibility, the form of which is popular in biological soft tissue [99, 148]. We define $\psi_{ECM}(\mathbf{U}^{(m)})$ as an isotropic *St. Venant-Kirchhoff* material

$$\psi_{ECM}(\mathbf{U}^{(m)}) = \frac{1}{2}\left(\lambda\delta_{ij}\delta_{kl}U_{ij}U_{kl} + 2\mu\delta_{il}\delta_{jk}U_{ij}U_{kl}\right) \text{ with } U_{ij}, U_{kl} \in U^{(m)}_{ab}. \tag{5.3}$$

While ψ_{fibre} is defined as a de-coupled function of the two fibre *Cosserat* strain measures, such that $\psi_{fibre}(\mathbf{U}^{(s)}, \mathbf{K}^{(s)}) = \psi_I(\mathbf{U}^{(s)}) + \psi_{II}(\mathbf{K}^{(s)})$. Assuming symmetry in cross fibre directions, they can be expressed as:

$$\psi_I(\mathbf{U}^{(s)}) = \frac{1}{2}\left(EA_f U_{ff}^2 + GA_f U_{tf}^2 + GA_f U_{nf}^2\right) \tag{5.4}$$

$$\psi_{II}(\mathbf{K}^{(s)}) = \frac{1}{2}\left(GI_1 K_{ff}^2 + EI_2 K_{tf}^2 + EI_2 K_{nf}^2\right) \tag{5.5}$$

where E is Young's modulus G is the shear modulus, I_1 and I_2 are the second moments of area corresponding to torsion and bending and A_f is the cross sectional area of the fibre bundle. In this sense, the characteristic length, l, is incorporated directly in the cross sectional area, $A_f = \frac{\pi l^2}{4}$ and the second moments of area $I_2 = I_1/2 = \frac{\pi l^4}{32}$. This allows us to express a variational principle as

$$\delta\Psi = \int_{\mathcal{B}} \{\boldsymbol{n} : \delta\mathbf{U} + \boldsymbol{m} : \delta\mathbf{K}\}\, \mathrm{d}V - W_{ext} \ , \tag{5.6}$$

where the force stress tensor, $\boldsymbol{n}$ (excluding the contributions from the incompressibility enforcement term) and the couple stress tensor, $\boldsymbol{m}$, given by

$$\boldsymbol{n} = \frac{\partial \psi_{ECM}}{\partial \mathbf{U}} + \frac{1}{A_f}\frac{\partial \psi_I}{\partial \mathbf{U}}$$

$$\boldsymbol{m} = \frac{1}{A_f}\frac{\partial \psi_{II}}{\partial \mathbf{K}}$$

are work conjugate to $\mathbf{U}$ and $\mathbf{K}$ respectively. Additionally the contributions from the fibre have been normalized with respect to the cross sectional area, limiting the internal length scale l, associated with the microspace, as a feature of the change of curvature strains only. It should be noted that $\mathbf{K}$ only has contributions from the fibre and as such coincides with $\mathbf{K}^{(s)}$, while $\mathbf{U}$ has contributions from both the fibre and the ECM and is fully set. This does not pose any problems with implementation as the positive definiteness condition is only required on the first stress tensor $\boldsymbol{n}$ and it's corresponding fourth order tangent stiffness tensors.

The linearisation of the stress tensors are fourth order stiffness tangent tensors, often referred to as "material elasticity tensors" or "constitutive tensors" , which relate strains into stress measures over discrete intervals. For the linear constitutive law, linearisation produces two unique constitutive tensors $\boldsymbol{\mathcal{H}}^{(1),(2)}$, given by

$$\boldsymbol{\mathcal{H}}^{(1)} = \frac{\partial \boldsymbol{n}}{\partial \mathbf{U}} = \frac{\partial^2 \psi_{ECM}}{\partial \mathbf{U}\partial \mathbf{U}} + \frac{1}{A_f}\frac{\partial^2 \psi_I}{\partial \mathbf{U}\partial \mathbf{U}} \tag{5.7}$$

$$\boldsymbol{\mathcal{H}}^{(2)} = \frac{\partial \boldsymbol{m}}{\partial \mathbf{K}} = \frac{1}{A_f}\frac{\partial^2 \psi_{II}}{\partial \mathbf{K}\partial \mathbf{K}} \tag{5.8}$$

5.2.1 Homogenization approach

In certain applications it may be preferable to utilize a homogenization approach instead of the method outlined above. In such a case one needs to introduce volume fractions vol_F and vol_M to weight the contributions from the fibre and the ECM accordingly. Total volume is preserved by enforcing $vol_F + vol_M = 1$. Additionally we no longer utilize $\mathbf{U}^{(m)}$, rather the fully set strain measure $\mathbf{U}$.

The stored energy function governing the behaviour of the matrix is extended to

$$\psi_{ECM}(\mathbf{U}) = \frac{1}{2}\left(\lambda\delta_{ij}\delta_{kl}U_{ij}U_{kl} + 2\mu\delta_{il}\delta_{jk}U_{ij}U_{kl}\right). \tag{5.9}$$

As a *St. Venant-Kirchhoff* material, $\psi_{ECM}(\mathbf{U})$ can inherit the incompressibility condition, especially in the formulations utilizing a *Poisson's* ration such that $\nu \to 0.5$. The stored energy function for the fibre remains unchanged as in Eq. (5.5). This allows us to express a variational principle as

$$\delta\Psi = \int_{\mathcal{B}} \{\boldsymbol{n} : \delta\mathbf{U} + \boldsymbol{m} : \delta\mathbf{K}\}\, \mathrm{d}V - W_{ext} = 0, \tag{5.10}$$

where the force stress tensor, $\boldsymbol{n}$ and the couple stress tensor, $\boldsymbol{m}$, are weighted by volume fractions and are given by

$$\boldsymbol{n} = vol_M \frac{\partial\psi_{ECM}}{\partial\mathbf{U}} + vol_F \frac{1}{A_f}\frac{\partial\psi_I}{\partial\mathbf{U}} \tag{5.11}$$

$$\boldsymbol{m} = vol_F \frac{1}{A_f}\frac{\partial\psi_{II}}{\partial\mathbf{K}}. \tag{5.12}$$

In this manner the stresses from the fibre and matrix "overlap" in specific directions and their combined contribution is weighted via the use of volume fractions. The fourth order constitutive tensors are developed in the same way.

Results of the linear constitutive law, for both approaches are presented in Chapter 7 under section 7.1.

5.3 Nonlinear elastic stored energy formulation

It is well known in that linear constitutive laws are fundamentally unsuitable for the modelling of biological tissue. Biological tissue exhibits highly nonlinear properties resulting from the complex fibre-collagen arrangement and composition inherent in the material. For example it has been shown for rat cardiac tissue, the arrangement of collagen strands surrounding fibre bundles are chaotic and sporadic in relaxed tissue, yet

under strain these collagen fibres are "stretched" into alignment with the muscle fibres [60, 151]. In the small strain range these fibres exhibit very little tension, allowing large strains to occur under relatively low loading conditions. Once the fibres align the tissue becomes increasingly stiffer at a rapid rate. This is phenomenon is illustrated in Figure 5.3. The majority of models today utilize nonlinear, exponential laws (often referred to as *Fung-type* exponentials) to capture this material nonlinearity. The exponential function is well suited to this type of deformation.

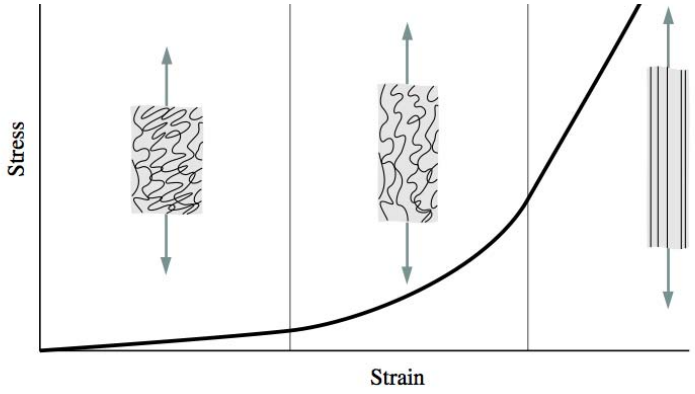

FIGURE 5.3: Schematic diagram reproduced from [60] of a typical (tensile) stress-strain curve for soft biological tissue showing the associated fibre morphology.

Consider the stored energy function of the material given by

$$\psi = \frac{1}{2}A\left(\exp^{BQ} - 1\right) + A_{comp}\left(J\,\ln J - J + 1\right). \tag{5.13}$$

Where A and B are stress scaling coefficients and Q is a function of the material strains, weighted by material parameters defined by

$$\begin{aligned} Q \;=\; & a_1 U_{ff}^2 + a_2(U_{tf}^2 + U_{nf}^2) + a_2\frac{I_1}{A_f}K_{ff}^2 + a_1\frac{I_2}{A_f}(K_{tf}^2 + K_{nf}^2) + \\ & b_1(U_{tt}^2 + U_{nn}^2) + b_2(U_{ft}^2 + U_{fn}^2 + U_{nt}^2 + U_{tn}^2). \end{aligned}$$

The material parameters a_i and b_i govern the material anisotropy for the fibre and matrix respectively. In this case, transverse isotropy has been modelled, requiring four material parameters. Introducing an additional material parameter a_3, to supplement the fibre anisotropy or allowing for an additionally defined flexural stiffness, would allow for an orthotropic material law.

For a given function Q there exists unique scaling coefficients A and B for the exponential Fung type stored energy function which can be shown explicitly.

Proof. Assume that there exists two pairs of scaling coefficients $\{A, B\}$ and $\{C, D\}$ that give the same strain energy potential. This implies that $\forall Q$,

$$Ae^{BQ} = Ce^{DQ}.$$

Using a Taylor expansion on both expressions yield

$$\sum_{n=0}^{\infty} \frac{AB^n e^{BQ}}{n!} Q^n = \sum_{n=0}^{\infty} \frac{CD^n e^{DQ}}{n!} Q^n \tag{5.14}$$

Equating coefficients based on the order of Q provides

$$Ae^{BQ} = Ce^{DQ} \tag{5.15}$$
$$ABe^{BQ} = CDe^{DQ} \tag{5.16}$$
$$AB^2 e^{BQ} = CD^2 e^{DQ} \tag{5.17}$$
$$\vdots \tag{5.18}$$
$$AB^\infty e^{BQ} = CD^\infty e^{DQ}. \tag{5.19}$$

Substitution of Eq. (5.15) into Eq. (5.16) shows that $B = D$. Then simple comparison shows $A = C$. Therefore, by contradiction A and B are a unique pair. □

For convenience and compactness, consider the parameter matrix for the stretch based strain U_{ij} and a corresponding material parameter matrix $\mathcal{A}$ given by

$$U = \begin{bmatrix} U_{ff} & U_{ft} & U_{fn} \\ U_{tf} & U_{tt} & U_{tn} \\ U_{nf} & U_{nt} & U_{nn} \end{bmatrix}, \qquad \mathcal{A} = \begin{bmatrix} a_1 & b_2 & b_2 \\ a_2 & b_1 & b_2 \\ a_2 & b_2 & b_1 \end{bmatrix}, \qquad \mathcal{B} = \frac{1}{A} \begin{bmatrix} a_2 I_1 & 0 & 0 \\ a_1 I_2 & 0 & 0 \\ a_1 I_2 & 0 & 0 \end{bmatrix}.$$

We can create similar corresponding matrices for K and a respective material parameters $\mathcal{B}$. Of course, for a one dimensional fibre, there would only be three components active in the change of curvatures strains K_{ff}, K_{tf} and K_{nf}. This allows us to compose

$$Q = \mathcal{A}_{ij} U_{ij}^2 + \mathcal{B}_{i1} K_{i1}^2. \tag{5.20}$$

Derivation of the force stress tensor $\boldsymbol{n}$ and the couple stress tensor $\boldsymbol{m}$ becomes straightforward using this matrix notation:

$$n_{ij} = \frac{\partial \psi}{\partial U_{ij}} = \mathcal{A}_{ij} U_{ij} ABe^Q \qquad \text{and} \qquad m_{ij} = \frac{\partial \psi}{\partial K_{ij}} = \mathcal{B}_{i1} K_{i1} ABe^Q \tag{5.21}$$

Four tangent stiffness tensors emerge from linearisation of the variation statement. These are given by the partial derivatives of these stress tensors by each of the strains **U** and **K**. These can be expressed as

$$\boldsymbol{\mathcal{H}}^{(1)}_{ijkl} = \frac{\partial n_{ij}}{\partial U_{kl}} \tag{5.22}$$

$$\boldsymbol{\mathcal{H}}^{(2)}_{ijkl} = \frac{\partial m_{ij}}{\partial K_{kl}} \tag{5.23}$$

$$\boldsymbol{\mathcal{H}}^{(3)}_{ijkl} = \frac{\partial n_{ij}}{\partial K_{kl}} \tag{5.24}$$

$$\boldsymbol{\mathcal{H}}^{(4)}_{ijkl} = \frac{\partial m_{ij}}{\partial U_{kl}} \tag{5.25}$$

Following the same process as the derivation of the stress tensors we can compose the tangent stiffness tensors as

$$\boldsymbol{\mathcal{H}}^{(1)}_{ijkl} = \mathcal{A}_{ij}\delta_{ik}\delta_{jl}ABe^{Q} + 2\mathcal{A}_{ij}U_{ij}\mathcal{A}_{kl}U_{kl}AB^{2}e^{Q} \tag{5.26}$$

$$\boldsymbol{\mathcal{H}}^{(2)}_{ijkl} = \mathcal{B}_{ij}\delta_{ik}\delta_{jl}ABe^{Q} + 2\mathcal{B}_{ij}K_{ij}\mathcal{B}_{kl}K_{kl}AB^{2}e^{Q} \tag{5.27}$$

$$\boldsymbol{\mathcal{H}}^{(3)}_{ijkl} = 2\mathcal{A}_{ij}U_{ij}\mathcal{B}_{kl}K_{kl}AB^{2}e^{Q} \tag{5.28}$$

$$\boldsymbol{\mathcal{H}}^{(4)}_{ijkl} = 2\mathcal{B}_{ij}K_{ij}\mathcal{A}_{kl}U_{kl}AB^{2}e^{Q} \tag{5.29}$$

5.3.1 Invariant based approach

Alternatively, we consider the invariant form of the nonlinear stored energy function expressed by Eq. (5.13), but with a modified Q defined by

$$\begin{aligned} Q &= b_1\,(tr(\mathbf{UM}_f))^2 + b_2\,(tr(\mathbf{UM}_t))^2 + b_3\,(tr(\mathbf{UM}_n))^2 + b_4\,(tr(\mathbf{U}^T\mathbf{UM}_f)) + \\ &\quad b_5\,(tr(\mathbf{U}^T\mathbf{UM}_t)) + b_6\,(tr(\mathbf{U}^T\mathbf{UM}_n)) + c_1\,(tr(\mathbf{KM}_f))^2 + c_4\,(tr(\mathbf{K}^T\mathbf{KM}_f)) \\ &= b_1\,J_4^2 + b_2\,J_5^2 + b_3\,J_6^2 + b_4\,J_7 + b_5\,J_8 + b_6\,J_9 + c_1\,L_4^2 + c_4\,L_7. \end{aligned} \tag{5.30}$$

This can also be expressed in index notation for convenience as

$$\begin{aligned} Q &= b_1\,U_{ff}^2 + b_2\,U_{tt}^2 + b_3\,U_{nn}^2 + b_4\,\left(U_{ff}^2 + U_{tf}^2 + U_{nf}^2\right) + b_5\,\left(U_{ft}^2 + U_{tt}^2 + U_{nt}^2\right) + \\ &\quad b_6\,\left(U_{fn}^2 + U_{tn}^2 + U_{nn}^2\right) + c_1\,K_{ff}^2 + c_4\,\left(K_{ff}^2 + K_{tf}^2 + K_{nf}^2\right)\ , \end{aligned} \tag{5.31}$$

where the three structural tensors are given by $\mathbf{M}_f = \mathbf{V}_f \otimes \hat{\mathbf{V}}_f$, $\mathbf{M}_t = \mathbf{V}_t \otimes \hat{\mathbf{V}}_t$ and $\mathbf{M}_n = \mathbf{V}_n \otimes \hat{\mathbf{V}}_n$. The strain invariants are defined as:

$$\begin{aligned}
J_1 &= tr\mathbf{U} \\
J_2 &= tr(\mathbf{U}^T\mathbf{U}) \\
J_3 &= tr(\mathbf{U}^3) \\
J_4 &= tr(\mathbf{U}\mathbf{M}_f) \\
J_5 &= tr(\mathbf{U}\mathbf{M}_t) \\
J_6 &= tr(\mathbf{U}\mathbf{M}_n) \\
J_7 &= tr(\mathbf{U}^T\mathbf{U}\mathbf{M}_f) \\
J_8 &= tr(\mathbf{U}^T\mathbf{U}\mathbf{M}_t) \\
J_9 &= tr(\mathbf{U}^T\mathbf{U}\mathbf{M}_n) \\
L_4 &= tr(\mathbf{K}\mathbf{M}_f) \\
L_7 &= tr(\mathbf{K}^T\mathbf{K}\mathbf{M}_f)
\end{aligned}$$

One can justify the exclusion of invariants J_1 and J_2 by noticing the following reduction

$$J_4 + J_5 + J_6 = \mathbf{U} : (\mathbf{M}_f + \mathbf{M}_t + \mathbf{M}_n) = \mathbf{U} : \mathbf{1} = J_1 \ , \tag{5.32}$$

showing that only three of the above mentioned invariants are linearly independent. A similar case exists relating J_7, J_8 and J_9 to J_2.

Using this invariant formulation we can express the force stress tensor as

$$\boldsymbol{n} = \frac{1}{2} AB \exp^{BQ} \frac{\partial Q}{\partial J_i} \frac{\partial J_i}{\partial \mathbf{U}} + \text{compressibility term} \tag{5.33}$$

and the couple stress tensor as

$$\boldsymbol{m} = \frac{1}{2} AB \exp^{BQ} \frac{\partial Q}{\partial L_i} \frac{\partial L_i}{\partial \mathbf{K}}. \tag{5.34}$$

The partial derivatives of the exponent Q can be compactly expressed as

$$\begin{aligned}
\frac{\partial Q}{\partial J_i}\frac{\partial J_i}{\partial \mathbf{U}} &= 2b_1\, J_4\, \mathbf{M}_f + 2b_2\, J_5\, \mathbf{M}_t + 2b_3\, J_6\, \mathbf{M}_n + 2b_4\, \mathbf{U}\mathbf{M}_f + 2b_5\, \mathbf{U}\mathbf{M}_t + 2b_6\, \mathbf{U}\mathbf{M}_n \\
\frac{\partial Q}{\partial L_i}\frac{\partial L_i}{\partial \mathbf{K}} &= 2c_1\, L_4\, \mathbf{M}_f + 2c_4\, \mathbf{K}\mathbf{M}_f \ .
\end{aligned}$$

Further details outlining the derivation can be found in the Appendix A.3.

Also, we consider the linearization of $\boldsymbol{n}$ and $\boldsymbol{m}$ as

$$\begin{aligned}\frac{\partial \boldsymbol{n}}{\partial \mathbf{U}} =& \frac{1}{2} AB^2 \exp^{BQ} \frac{\partial Q}{\partial J_a}\frac{\partial J_a}{\partial \mathbf{U}}\frac{\partial Q}{\partial J_b}\frac{\partial J_b}{\partial \mathbf{U}} + \frac{1}{2} AB \exp^{BQ} \frac{\partial Q}{\partial J_a}\frac{\partial^2 J_a}{\partial \mathbf{U}\partial \mathbf{U}} + \\ & \frac{1}{2} AB \exp^{BQ} \frac{\partial^2 Q}{\partial J_a \partial J_b}\frac{\partial J_a}{\partial \mathbf{U}}\frac{\partial J_b}{\partial \mathbf{U}} + \text{compressibility term} \end{aligned} \tag{5.35}$$

$$\begin{aligned}\frac{\partial \boldsymbol{m}}{\partial \mathbf{K}} =& \frac{1}{2} AB^2 \exp^{BQ} \frac{\partial Q}{\partial L_a}\frac{\partial L_a}{\partial \mathbf{K}}\frac{\partial Q}{\partial L_b}\frac{\partial L_b}{\partial \mathbf{K}} + \frac{1}{2} AB \exp^{BQ} \frac{\partial Q}{\partial L_a}\frac{\partial^2 L_a}{\partial \mathbf{K}\partial \mathbf{K}} + \\ & \frac{1}{2} AB \exp^{BQ} \frac{\partial^2 Q}{\partial L_a \partial L_b}\frac{\partial L_a}{\partial \mathbf{K}}\frac{\partial L_b}{\partial \mathbf{K}} \end{aligned} \tag{5.36}$$

$$\frac{\partial \boldsymbol{n}}{\partial \mathbf{K}} = \frac{1}{2} AB^2 \exp^{BQ} \frac{\partial Q}{\partial J_a}\frac{\partial J_a}{\partial \mathbf{U}}\frac{\partial Q}{\partial L_b}\frac{\partial L_b}{\partial \mathbf{K}} \tag{5.37}$$

$$\frac{\partial \boldsymbol{m}}{\partial \mathbf{U}} = \frac{1}{2} AB^2 \exp^{BQ} \frac{\partial Q}{\partial L_a}\frac{\partial L_a}{\partial \mathbf{K}}\frac{\partial Q}{\partial J_b}\frac{\partial J_b}{\partial \mathbf{U}} \,. \tag{5.38}$$

These are the same tangent stiffness tensors presented in Eqs. (5.22) - (5.25). The parameters for b_i and c_j can be found via comparison with the full index formulation given below:

$$\begin{aligned}\boldsymbol{\mathcal{H}}^{(1)}_{ijkl} =& AB \exp^{BQ} \left[\frac{B}{2} \left(\frac{\partial Q}{\partial J_a}\frac{\partial J_a}{\partial \mathbf{U}} \right)_{ij} \left(\frac{\partial Q}{\partial J_b}\frac{\partial J_b}{\partial \mathbf{U}} \right)_{kl} + \delta_{ik} \Big(b_4 \left(\mathbf{M}_f\right)_{jl} + b_5 \left(\mathbf{M}_t\right)_{jl} + b_6 \left(\mathbf{M}_n\right)_{jl} \Big) \right. \\ & \left. + b_1 \left(\mathbf{M}_f\right)_{ij} \left(\mathbf{M}_f\right)_{kl} + b_2 \left(\mathbf{M}_t\right)_{ij} \left(\mathbf{M}_t\right)_{kl} + b_3 \left(\mathbf{M}_n\right)_{ij} \left(\mathbf{M}_n\right)_{kl} \right] \\ & + \text{compressibility term} \end{aligned}$$

$$\boldsymbol{\mathcal{H}}^{(2)}_{ijkl} = AB \exp^{BQ} \left[\frac{B}{2} \left(\frac{\partial Q}{\partial L_a}\frac{\partial L_a}{\partial \mathbf{K}} \right)_{ij} \left(\frac{\partial Q}{\partial L_b}\frac{\partial L_b}{\partial \mathbf{K}} \right)_{kl} + \delta_{ik}\, c_4 \left(\mathbf{M}_f\right)_{jl} + c_1 \left(\mathbf{M}_f\right)_{ij} \left(\mathbf{M}_f\right)_{kl} \right]$$

$$\boldsymbol{\mathcal{H}}^{(3)}_{ijkl} = \frac{1}{2} AB^2 \exp^{BQ} \left(\frac{\partial Q}{\partial J_a}\frac{\partial J_a}{\partial \mathbf{U}} \right)_{ij} \left(\frac{\partial Q}{\partial L_b}\frac{\partial L_b}{\partial \mathbf{K}} \right)_{kl}$$

$$\boldsymbol{\mathcal{H}}^{(4)}_{ijkl} = \frac{1}{2} AB^2 \exp^{BQ} \left(\frac{\partial Q}{\partial L_a}\frac{\partial L_a}{\partial \mathbf{K}} \right)_{ij} \left(\frac{\partial Q}{\partial J_b}\frac{\partial J_b}{\partial \mathbf{U}} \right)_{kl}$$

with the partial derivative terms given by

$$\begin{aligned}\left(\frac{\partial Q}{\partial J_a}\frac{\partial J_a}{\partial \mathbf{U}} \right)_{ij} &= 2 \left(b_1\, J_4 \left(\mathbf{M}_f\right)_{ij} + b_2\, J_5 \left(\mathbf{M}_t\right)_{ij} + b_3\, J_6 \left(\mathbf{M}_n\right)_{ij} + b_4\, U_{ik} \left(\mathbf{M}_f\right)_{kj} + \right. \\ & \qquad \left. b_5\, U_{ik} \left(\mathbf{M}_t\right)_{kj} + b_6\, U_{ik} \left(\mathbf{M}_n\right)_{kj} \right) \\ \left(\frac{\partial Q}{\partial L_a}\frac{\partial L_a}{\partial \mathbf{K}} \right)_{ij} &= 2 \left(c_1\, L_4 \left(\mathbf{M}_f\right)_{ij} + c_4\, K_{ik} \left(\mathbf{M}_f\right)_{kj} \right) . \end{aligned}$$

Chapter 6

Cardiac mechanics

In this chapter, the basic functioning of the heart and all its constituents will be presented. The structural components of the heart with a focus on the left ventricle will be examined. The macro and micro specific considerations for modelling cardiac tissue are considered in detail and defining characteristics of our model are introduced.

6.1 Structure

Within the heart there are four main cavities through which blood passes. These are the left and right atria; and the left and right ventricles which are identified in Figure 6.1. The ventricles are larger than the atria as they pump blood out of the heart to the body and lungs whereas the atria pump blood into the ventricles via valves. The walls of the left ventricle are formed from muscular myocardium with the outer layer termed the epicardium and the inner layer the endocardium. The muscle tissue between the epicardium and endocardium is commonly referred to as the midwall. The bottom tip of the left ventricle is called the apex, while top of the left ventricle is near the base of the heart, not to be confused with the bottom.

The mitral valve controls the flow of blood passed from the left atrium to the left ventricle. A large artery, the aorta, connects the left ventricle to the major arteries that provide oxygenated blood to the rest of the body. Separating the left ventricle and the aorta is the aortic valve, which opens once the blood pressure in the ventricle rises above the blood pressure in the aorta.

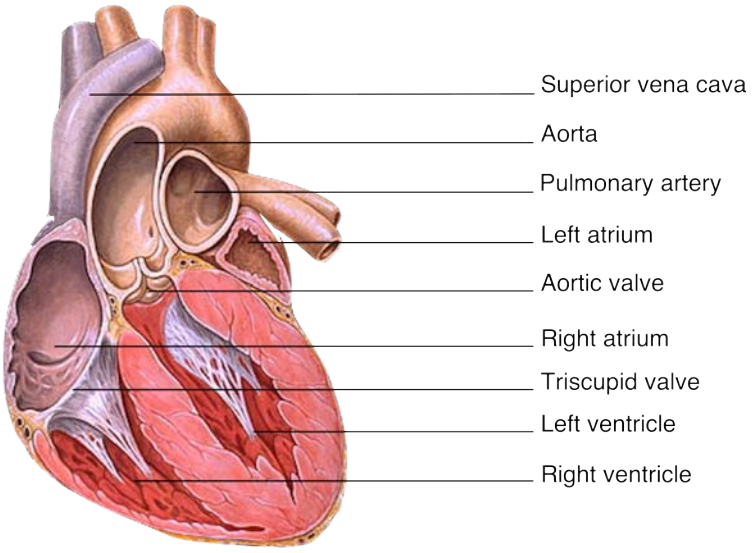

FIGURE 6.1: A labelled cross-section of a human heart

The physiological function of the heart can be accurately described using mechanical, chemical and electrical terms. For example, the electrocardiogram (ECG) is a common non-invasive diagnostic tool which monitors electrical changes on the skin caused by the depolarization of the heart. Ventricular pressure and cavity volume are commonly recorded and presented in medical journals as the benchmark gauges to analyse cardiac performance and health. Important clinical measurements utilized by clinicians, such as the stroke volume and the ejection fraction are derived from pressure-volume relations measured during cardiac function. At the beginning of diastolic filling the pressure is at it's lowest and steadily increases as the ventricle fills with oxygenated blood. The aortic valve remains closed through diastolic filling and during the start of systole, known as isovolumetric contraction, in order for the cavity to accumulate enough pressure that will enable a sufficient ejection through the entire blood vessel network of the body. A typical evolution of the ventricular pressure with respect to its volume is plotted for a whole heartbeat cycle, shown in Figure 6.2.

The left ventricle is the largest cavity in the heart, and most susceptible to myocardial infarctions. It is logically the favoured starting point of cardiac modelling and will be the focus of this study.

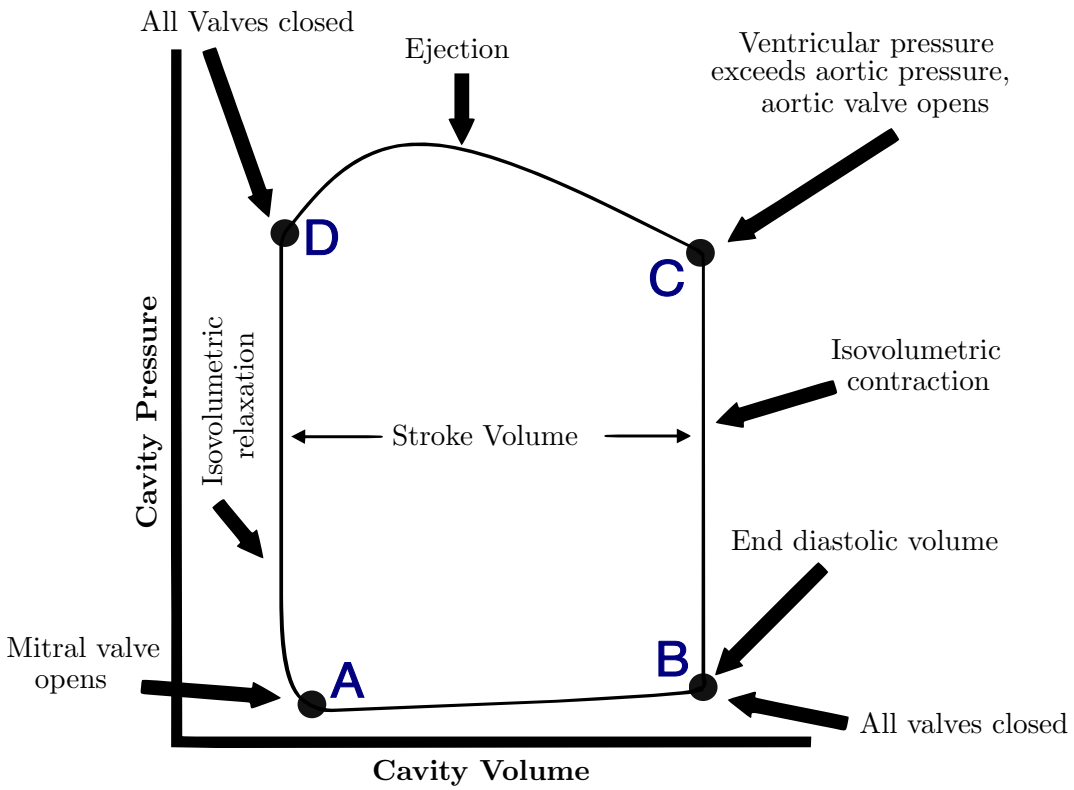

FIGURE 6.2: From A to B, the tissue response is passive as the ventricle expands during diastolic filling. The final filling volume at B is known as the end diastolic volume (EDV). Between B and C, the cardiac tissue activates while the aortic valve is closed causing an isovolumetric contraction, meaning that the cavity volume remains constant during this period. Through C to D, ejection occurs and the myocardium continue contracting till the ventricle is emptied. The end systolic volume (ESV) is obtained at D and corresponds to the same value at A. From D to A, the cardiac tissue relax, lowering the pressure inside but keeping volume constant

6.2 Geometry

6.2.1 Prolate spheroidal coordinates

A common simplification of the left ventricle geometry can be be expressed as a truncated ellipsoid, defined by the orthogonal prolate spheroidal coordinate system (η, θ, ϕ) [13, 110]. These coordinates are related to the Cartesian coordinate system in the following manner:

$$\begin{aligned} x &= C\sinh(\eta)\sin(\theta)\cos(\phi) \\ y &= C\sinh(\eta)\sin(\theta)\sin(\phi) \\ z &= C\cosh(\eta)\cos(\theta) \end{aligned} \tag{6.1}$$

The above formulation is suitable to model multiple left ventricle geometries of different sizes using C as a scaling factor and η to define the thickness of the myocardium wall. The variable $\theta \in [0, \pi)$, is used to determine the relative position of the base and apex (see Figure 6.3), and $\phi \in [0, 2\pi)$, to define a full 360^o geometry with a reasonable geometric likeness of the left ventricle.

The unit vectors of the prolate spheroid system in Cartesian coordinates can be obtained by differentiating (6.1) by η, θ and ϕ respectively, and grouping appropriate terms. This gives

$$\begin{aligned}
\boldsymbol{\eta} &= n_{\eta\theta\phi}\left(\cosh(\eta)\sin(\theta)\cos(\phi)\mathbf{e}_1 + \cosh(\eta)\sin(\theta)\sin(\phi)\mathbf{e}_2 + \sinh(\eta)\cos(\theta)\mathbf{e}_3\right) \\
\boldsymbol{\theta} &= n_{\eta\theta\phi}\left(\sinh(\eta)\cos(\theta)\cos(\phi)\mathbf{e}_1 + \sinh(\eta)\cos(\theta)\sin(\phi)\mathbf{e}_2 - \cosh(\eta)\sin(\theta)\mathbf{e}_3\right) \\
\boldsymbol{\phi} &= -\sin(\phi)\mathbf{e}_1 + \cos(\phi)\mathbf{e}_2.
\end{aligned}$$

Where $n_{\eta\theta\phi}$ is the normalising scaling factor given by

$$n_{\eta\theta\phi} = \frac{1}{\sqrt{\cosh^2(\eta)\sin^2(\theta) + \sinh^2(\eta)\cos^2(\theta)}}.$$

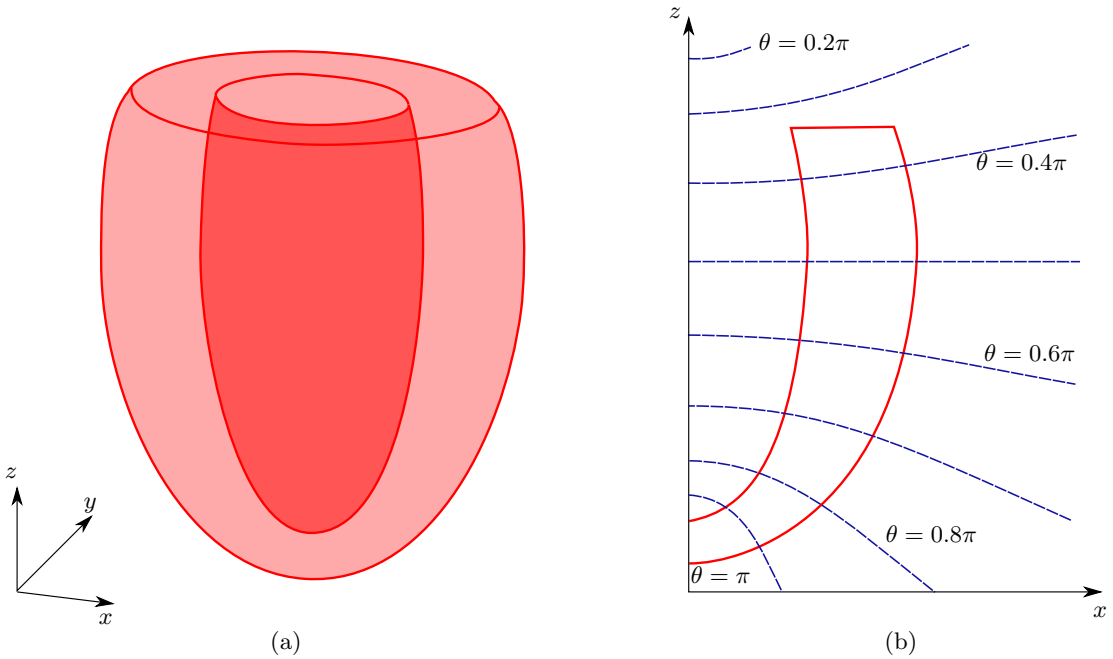

(a) (b)

FIGURE 6.3: The left ventricle geometry approximated by prolate spheroid coordinates. (a) Full three dimensional representation. (b) A two dimensional perspective of the ellipsoid achieved by setting $\phi = 0$. Profile shows the geometry from apex to base with the $\eta = 0.37$ to create the endocardium and $\eta = 0.68$ to create the epicardium.

6.2.2 Fibre orientation

The fibre orientation in the left ventricle has a critical influence on mechanical and electrical function [33, 112, 155]. The influence on shear strain in the circumferential and radial plane of the left ventricle is largely dominated by the fibre orientation [145]. However the description fibre orientation in the left ventricle is a highly complex and sophisticated task, which has been the subject of significant historical disagreement [16, 46]. This stems from the complex multi scale branching and merging that occurs on a cellular and micro scale, creating anisotropy features that change dramatically throughout the structure. The description of the cardiac structure is therefore a three dimensional network problem.

Myocytes are arranged along their axis to form myofibrils, which vary in orientation throughout the domain. We establish our fibre orientation $\mathbf{V}_f$ along the axis of these myofibrils which are bundled together by collagen in the ECM. It has been found that there is a distinct grouping of fibres in sheets, which are coupled via the ECM [83]. The following section outlines the description of an orthonormal fibre local coordinate system, that accurately portrays the mycocyte architecture of the left ventricle through the use of unit vectors describing the fibre, $\mathbf{V}_f$, sheet-tangent $\mathbf{V}_t$ and sheet-normal $\mathbf{V}_n$ directions at each material point.

To quantify the muscle fibre orientation we make use of the helix fibre angle α_h and transverse fibre angle α_t as illustrated in Figure 6.4. For a position $P(x, y, z)$ in the ellipsoid, α_h and α_t dictate the angles between the fibre orientation and the unit vector in the circumferential direction $\boldsymbol{\phi}$.

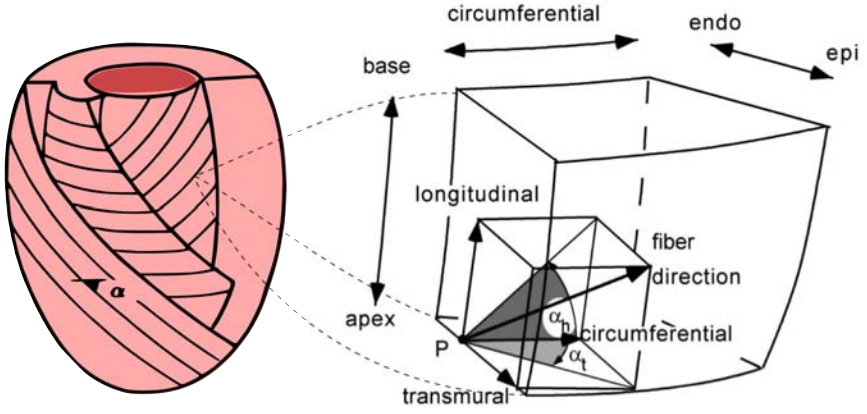

FIGURE 6.4: Illustration of the helix fibre angle α_h and transverse fibre angle α_t in the left ventricle [13, 111] .

Smooth mathematical functions for fibre orientation are needed for the computational model. For the helix fibre angle, we include the data set from the experimental studies of

[138] and [97]. Two data fits have been included for the purposes of this study. The first, a first order polynomial fit, is employed following the implementation of an optimization study carried out by [111]. It is important to note that the bulk of the data sets lie in the midwall region. The majority of curve fitting algorithms would produce fitted functions that track closely with the bulk of the data set (i.e the midwall) and might not accurately represent the fibre orientation at the epicardium and endocardium. This motivated the introduction of a the second curve fit, a first order trigonometric approach. The curve fitting and analysis was constructed using the curve fitting tools of MATLAB. As evident in the summary produced in Table 6.1 the trigonometric fit is an overall superior fit in addition to preserving the edge orientation of the fibres more sufficiently.

TABLE 6.1: Comparison of accuracy of the two fitted functions for the transmural course of the helix fibre angle

Type of fit	**SSE**	**R-Squared**	**RMSE**
1st Order Polynomial	13.84×10^3	0.875	13.586
1st Order Trigonometric	10.32×10^3	0.907	11.732

The data sets, and the two fitted functions are included in Figure 6.5.

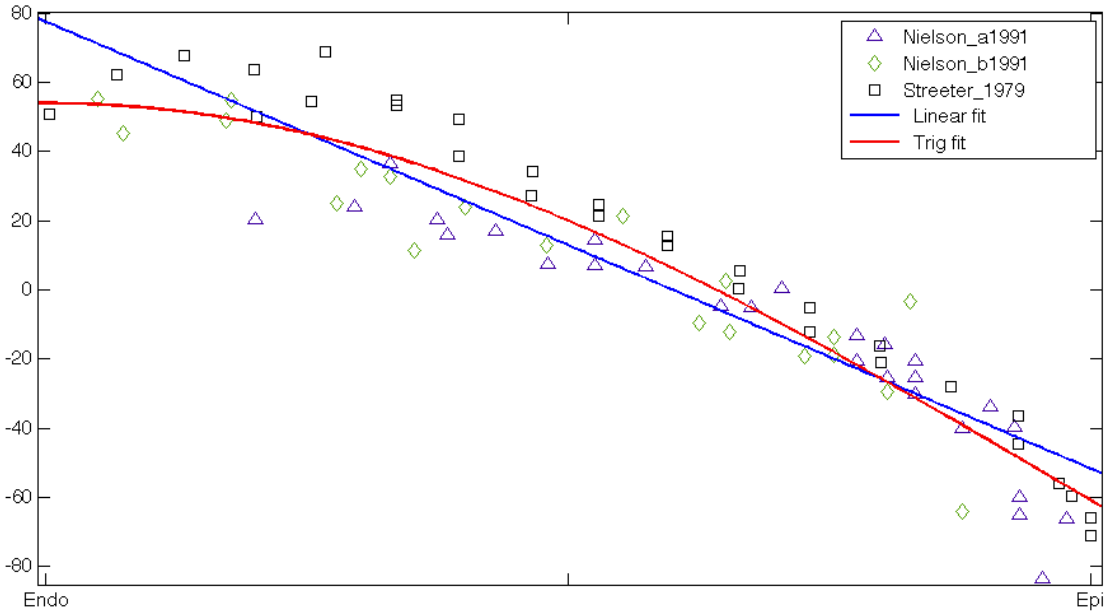

FIGURE 6.5: Transmural course of helix fiber angle α_h from (□) Streeter 1979, equatorial region of human LV; (△) Nielson *et al.* 1991 , equatorial region of canine LV; (◇) Nielson *et al.* 1991, adjacent more apical region of canine LV; (-) Fitted functions.

The lack of experimental data for the transmural angle α_t poses a large problem. Widely cited and used in mathematical models are the results taken from Rijcken et al. [111]. The paper presented the results of fibre orientation, obtained via an optimization routine

to produce a homogeneous fibre strain distribution in an ellipsoid finite element model undergoing ejection. There are some concerns surrounding this approach. Firstly, the premise of homogeneous fibre strain may be flawed. It was previously believed that the left ventricle fibres contracted or relaxed simultaneously. This misconception stems from the ways in which information about cardiac function was gathered in the past [16]. Secondly, there is a significant lack of quantitative data available to verify the model, self acknowledged by [111].

In light of these concerns we propose our own mathematical formulation. Our formulation is based on more recent data published in [14], where fibre orientation of canine left ventricles were captured using optimized Diffusion Tensor Imaging. The recorded angle α_h corresponds with our previously found results and the results for α_t provide sufficient information to model. The results are summarized graphically in Figure 6.6. In order to synthesise the transmural angle α_t as a smooth function, we introduce the

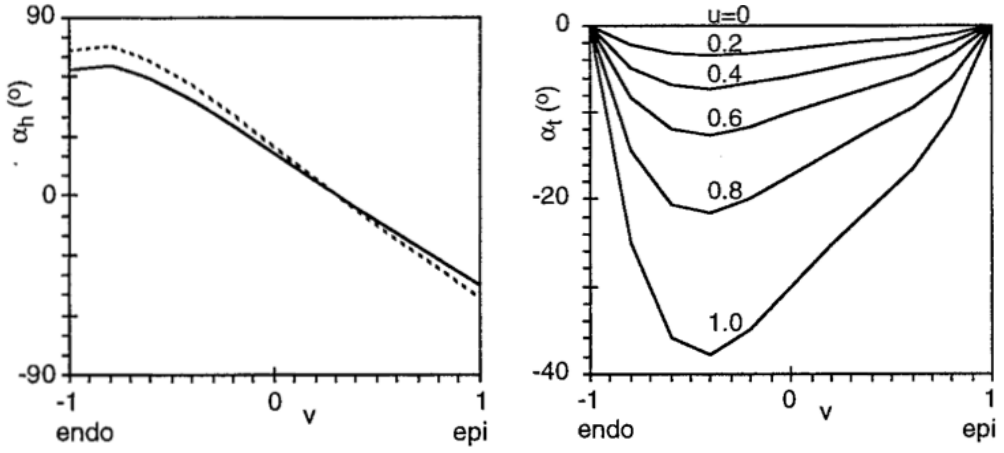

(a) (b)

FIGURE 6.6: Reference results for the helix fibre angle α_h and transverse fibre angle α_t from DTI MRI results [14], where v is the transmural coordinate that is -1 at the endocardium and 1 at the epicardium; and u is a longitudinal coordinate that is 0 at the equator and 1 at the apex.

following modelled functions

$$\alpha_t(\hat{\eta},\hat{\theta}) = -31\hat{\theta}|\hat{\theta}|^{0.6}\hat{\eta}\left(1-\frac{\ln(\hat{\eta})}{\ln(\hat{\eta}_{epi})}\right) \tag{6.2}$$

$$\hat{\theta} = \frac{\theta-\theta_{equator}}{\theta_{apex}-\theta_{equator}} \tag{6.3}$$

$$\hat{\eta} = 1.6160\frac{\eta-\eta_{endo}}{\eta_{epi}-\eta_{endo}}. \tag{6.4}$$

The transformation applied on η in Eq. (6.4) stems from the curve fitted form of the trigonometric approximation of α_h, which is found to be

$$\alpha_h(\hat{\eta}) = 110\cos(\hat{\eta}) - 56. \tag{6.5}$$

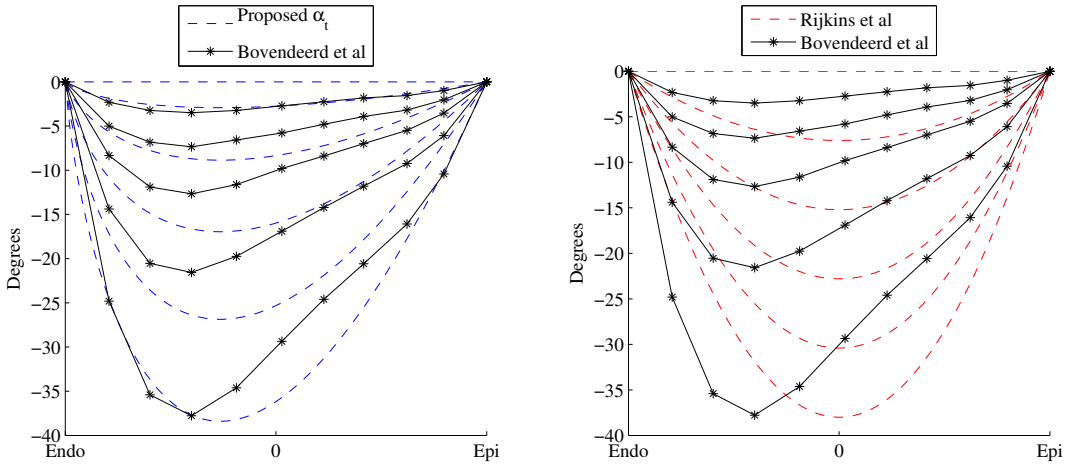

(a) Proposed α_t based on Bovendeerd *et al* 1999

(b) Optimized α_t from Rijkins *et al* 1999

FIGURE 6.7: Comparison of different approximations of the transmural angle α_t (given by dotted lines) to actual data (solid lines)

The mathematical representation that Rijcken et al. [111] derive for α_t is

$$\alpha_t(u, v) = -38u(1 - v^2), \tag{6.6}$$

where v is the transmural coordinate that is -1 at the endocardium and 1 at the epicardium; and u is a longitudinal coordinate that is 0 at the equator and 1 at the apex. Meaningfully transferring these solutions to the prolate spheroidal coordinates is easily achieved via trigonometric projections of α_h and α_t onto the relevant unit vectors specified in (6.2). For a position $P(x, y, z)$ in the ellipsoid, we can define the fibre orientation $\mathbf{V}_f{}^*$, before it is normalized as

$$\mathbf{V}_f{}^* = \tan(\alpha_t)\boldsymbol{\eta} + \tan(\alpha_h)\boldsymbol{\theta} + \boldsymbol{\phi}. \tag{6.7}$$

In order to establish an orthonormal basis system around the fibre orientation, we scale the fibre to a single unit length given by $\mathbf{V}_f$. This allows us to establish a normalized fibre orientation field throughout the domain of the truncated ellipsoid geometry as illustrated in Figure 6.8.

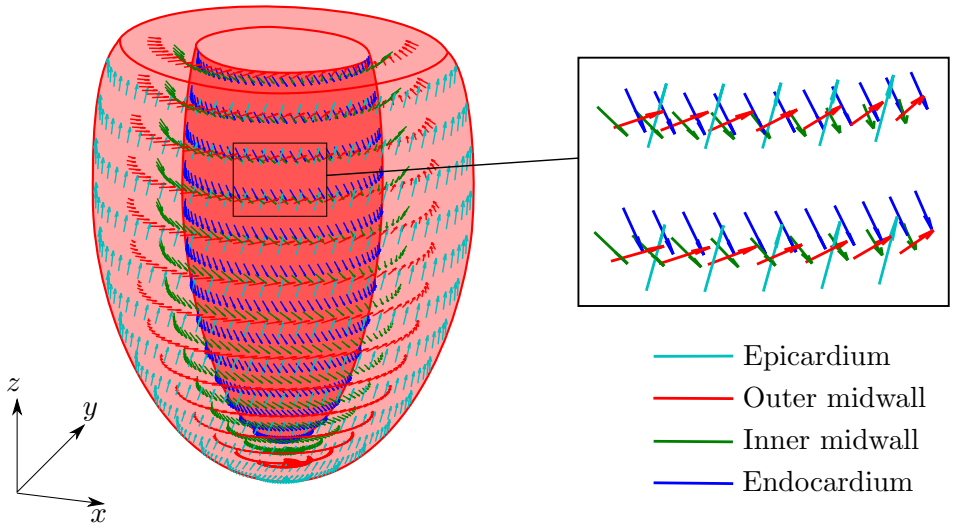

FIGURE 6.8: Schematic of fibre orientation plotted on half of the ellipsoid domain accompanied with a zoomed in section of the fibre orientation from equatorial region. Different colours correspond to distinct layers in the transmural direction.

This formulation of the fibre orientation is formulated in terms of the prolate spheroidal coordinates. However in order to obtain these, we need to establish a transform map from the Cartesian coordinate system. Unlike oblate spheroidal coordinates, prolate spheroidal coordinates are not degenerative, which means that there exists a unique reversible transform between them and the Cartesian coordinates. These can be considered inverse relations to Eq. (6.1). For a given x, y and z, one can find the prolate spheroidal coordinates from

$$\tan(\phi) = \frac{y}{x} \tag{6.8}$$

$$\cos(\theta) = \frac{d_1 - d_2}{2C} \tag{6.9}$$

$$\cosh(\eta) = \frac{d_1 + d_2}{2C}. \tag{6.10}$$

Where d_1 and d_2 are the focal points of the ellipse in the plane defined by ϕ and are given by

$$d_1^2 = (z + C)^2 + x^2 + y^2 \tag{6.11}$$

$$d_2^2 = (z - C)^2 + x^2 + y^2. \tag{6.12}$$

The full derivation can be found in the appendix in Section A.4.

6.3 Cardiac function

A more detailed presentation of the cardiac cycle is presented in this section. During the cardiac cycle, significant changes in ventricular volume, pressure and chemical composition occur. These changes are divided into distinct stages, characterized by contractile behaviour of the ventricle: while the ventricle is contracting, it is classified as systole, when it is passive it is classified as diastole.

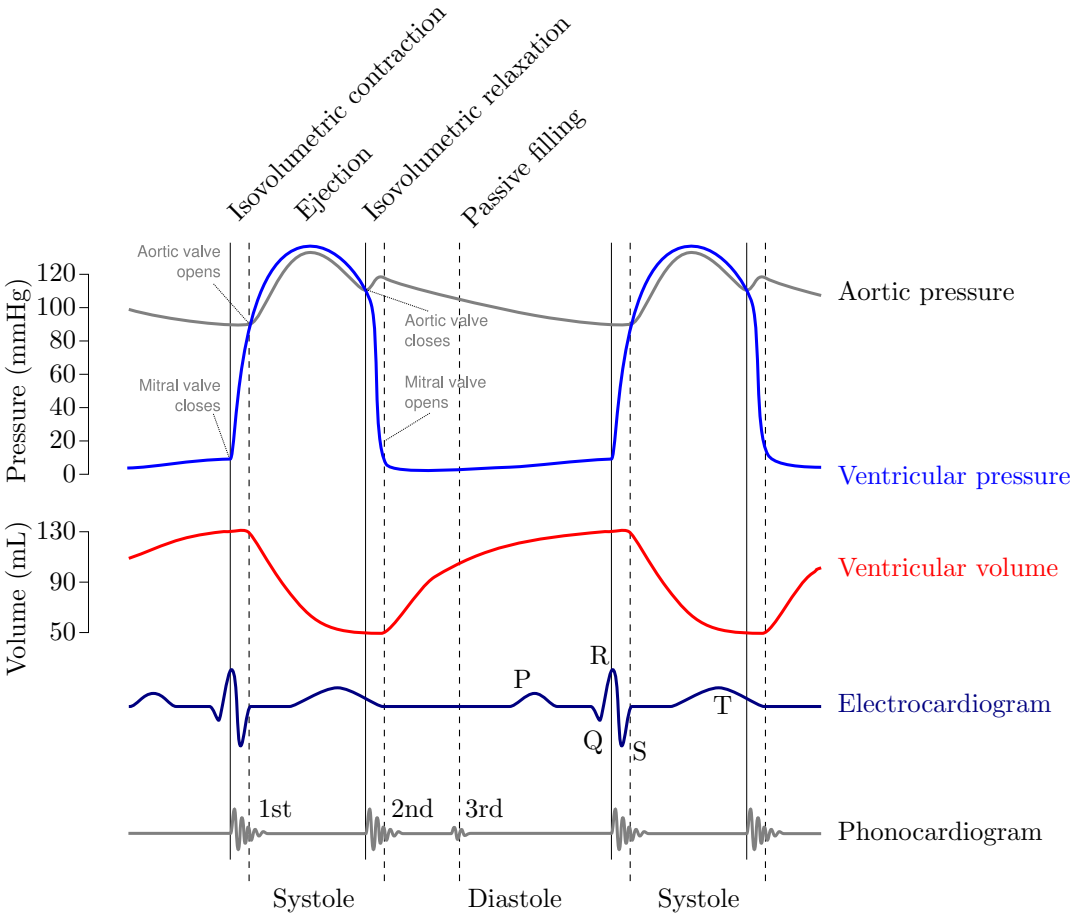

FIGURE 6.9: A simplified Wiggers diagram, showing the cardiac cycle in the left ventricle. In the electrocardiogram: wave "P" corresponds to atrial depolarization, waves "QRS" correspond to ventricular depolarization, and wave "T" corresponds to ventricular repolarization. In the phonocardiogram: The sound labelled 1st contributes is the reverberation of blood from the sudden closure of the mitral valve and the sound labelled "2nd" contributes is the reverberation of blood from the sudden closure of the aortic valve. [41]

Diastole and systole can be further divided into two phases. The four main phases for the left ventricle can be identified as follows:

- Passive filling: The mitral valve opens, allowing blood to fill the ventricle. The cavity volume increases as more blood flows into the ventricle and the pressure increases accordingly. The material behaves completely passively in this phase.

- Isovolumetric contraction: The ventricle contracts with the mitral valve and aortic valve closed. The cavity volume remains constant or nearly constant since all valves are closed and the pressure in the cavity increases due to the contraction of the ventricle. Active tension is introduced in this phase and continuously increases at a rapid pace.

- Ejection: Once the pressure within the cavity reaches the same pressure as in the aorta, the aortic valve opens and blood is ejected from the ventricle. The cavity volume decreases as blood is expelled from the contracting left ventricle. The pressure in the cavity first increases further due to the compliance of the aorta and then decreases as the rate of ejection decreases. The active tension reaches a peak in this phase and starts to tail off.

- Isovolumic relaxation: Once the cavity ceases to contract further the aortic valve closes and the ventricle relaxes. The cavity volume remains constant or nearly constant as all the valves are closed. The pressure decreases due to the relaxation of the ventricle. The active tension declines to zero and by the end of relaxation the material is once again in a fully passive state.

The end systolic volume (ESV) is defined as the cavity volume at end of ejection. The end diastolic volume (EDV) is defined as the cavity volume immediately prior isovolumetric contraction. The stroke volume is as the amount of blood expelled during systole (i.e. the difference between end diastolic volume and end systolic volume). The ejection fraction is defined as the stroke volume divided by the end diastolic volume.

$$\mathrm{EF} = \frac{(EDV - ESV)}{EDV} \tag{6.13}$$

Another commonly used metric to measure healthy systolic function is fractional shortening (FS). This is given as the percentage change in the diameter at end diastole (EDD) and the diameter at end systole (ESD). The measurements are taken at the equator and on the endocardium. The formula is given by

$$\mathrm{FS} = \frac{(EDD - ESD)}{EDD} \ . \tag{6.14}$$

6.4 Passive mechanics behaviour

The passive mechanical properties of the myocardium has been detailed in Chapter 5. For comparison, a secondary passive constitutive model will be presented. The model was introduced by Usyk et al. [147] and models the myocardium as a hyperelastic nonlinear Fung-type stored energy function

$$\Psi = A\frac{\left(e^{Q}-1\right)}{2} + A_{comp}(J \cdot ln\, J - J + 1), \tag{6.15}$$

with $Q = b_{ff}E_{ff}^2 + b_{nn}E_{nn}^2 + b_{tt}E_{tt}^2 + b_{tn}(E_{nt}^2 + E_{tn}^2) + b_{ft}(E_{ft}^2 + E_{tf}^2) + b_{fn}(E_{fn}^2 + E_{nf}^2)$. The material stiffness parameters b_{ij} are multiplied with corresponding components E_{ij} from the Green strain tensor and, in this way, govern the anisotropy, while A is used as global stress scaling factor. The second term enforces the incompressibility condition. The practical difference between our model presented in the previous chapter and this one is the inclusion of the change curvature strains in the *Cosserat* continuum. In order to be comparable with our transversely isotropic model Eq. (6.15) has to be modified in an appropriate manner. This is achieved by setting $b_{nn} = b_{tt}$ and $b_{fn} = b_{ft}$ and calibrating the model with reduced material parameters.

6.5 Active mechanics behaviour

A key aspect of modelling the mechanics of the heart is describing the active contraction of cardiac tissue. Contraction occurs on a cellular level when the sarcomere, the contractile unit of the myocyte, develops tension and contracts due to changes in the intracellular calcium concentration level. The contraction of each individual myocyte causes the overall contraction of the myocardium. To model this contraction, we employ a homogenization approach, following the active stress model of Guccione et al. [49], where the total stress is the combined components from active and passive material behaviour.

The active stress model requires a constitutive law that describes the dynamics of tension development due to changes in the cell, be they mechanical such as stretch, or chemical such as intracellular calcium concentration. This constitutive law defines the active tension, T_A as a function of the stretch and time. The resulting active tension is transformed into an active stress acting in the fibre direction.

Tension development is initiated when an electrical impulse passes over the sarcomere causing calcium ion channels to open and increasing intracellular calcium concentration. The increase in intracellular calcium concentration causes a cyclical binding of myosin

heads with actin and the subsequent sliding and overlapping of the myofilaments. Adenosine triphosphate supplies the energy for contraction of the myocyte. The overlapping of these myofilaments causes the contraction of the myocyte.

In order to stay consistent with the passive theory model the active approach needs to be formulated in $\mathbf{U}$ and $\mathbf{K}$, i.e. we consider a nonlinear active stress distribution over the fibre cross section (non-homogeneous active fibre stress over the bundle cross section). This is achieved by the following ansatz:

$$T_A = f(\mathbf{U} + z\mathbf{K}) = f(\bar{\mathbf{U}})\,. \tag{6.16}$$

$f(\bar{\mathbf{U}})$ can be evaluated via Taylor series and integration over the cross section:

$$\begin{aligned} T_A(\bar{\mathbf{U}}, t) &= \int_{-\frac{l}{2}}^{\frac{l}{2}} f(\bar{\mathbf{U}}, t)|_{z=0} + z^2 \frac{\partial^2 f}{\partial \bar{\mathbf{U}} \partial \bar{\mathbf{U}}}|_{z=0} \frac{\partial \bar{\mathbf{U}}}{\partial z} \frac{\partial \bar{\mathbf{U}}}{\partial z}\, dz = \\ &= \mathrm{d}\, f(\bar{\mathbf{U}}, t)|_{z=0} + \frac{l^3}{12} \frac{\partial^2 f}{\partial \bar{\mathbf{U}} \partial \bar{\mathbf{U}}}|_{z=0}\, \mathbf{K}^2\ , \end{aligned} \tag{6.17}$$

where l denotes the diameter of the bundle. As $l \ll 1$ we consider contributions resulting from curvature strains as negligible and remove them from the consideration as a valid simplification without influencing the mechanics of the problem.

In the active stress formulation the total force stress $\boldsymbol{n}$ is defined as the sum of a passive force stress $\boldsymbol{n}_P$ and an active stress $\boldsymbol{n}_A$ so that

$$\boldsymbol{n} = \boldsymbol{n}_P + \boldsymbol{n}_A. \tag{6.18}$$

The passive stress is taken from the passive mechanical law so that when there is no active stress the myocardium simply behaves passively. The active stress is assumed to act only in the fibre direction $\mathbf{V}_f$. In this sense the active stress can be defined by the active tension parameter T_A, projected in fibre orientation via the use of the structural tensor

$$\boldsymbol{n}_A = \boldsymbol{f}(\mathbf{U},\, t) = T_A(\mathbf{U},\, t)\, \mathbf{M}_f. \tag{6.19}$$

Following the formulation of Guccione et al. [49], we introduce a function for the active tension based on chemical and physical properties of the myocardium undergoing contraction. This model was derived from biophysical considerations of calcium dynamics and crossbridge formation resulting from experimental data. The active tension is

defined as

$$T_A = T_{max} \frac{Ca_0^2}{Ca_0^2 + ECa_{50}^2(l_s)} C_t(l_s, t), \tag{6.20}$$

where C_t represents the time transient dependent on time and sarcomere length, ECa_{50}^2 represents the calcium concentration at which tension is 50%, Ca_0 is the peak intracellular calcium concentration, l_s is the sarcomere length and T_{max} is the maximum tension developed.

The current sarcomere length is a function of $\mathbf{U}$ and the original sarcomere length l_{s_0}, given by

$$l_s = l_{s_0} J_4. \tag{6.21}$$

Which simply exploits the current stretch of the material point in the fibre orientation as $J_4 = tr(\mathbf{U}\mathbf{M}_f)$. As such, the linearization of the stress tensor $\boldsymbol{n}_A$ needed for the strain energy approach is given by

$$\mathcal{H}^A = \frac{\partial \boldsymbol{n}_A}{\partial \mathbf{U}} = \frac{\partial \boldsymbol{n}_A}{\partial l_s} \frac{\partial l_s}{\partial J_4} \frac{\partial J_4}{\partial \mathbf{U}}, \tag{6.22}$$

which complement the other tangent stiffness tensors from the passive mechanics constitutive laws. To further develop the active tension we define the functions $ECa_{50}^2(l_s)$ and $C_t(l_s, t)$ in Eq. (6.20) as

$$C_t(l_s, t) = \frac{1}{2}\left[1 - \cos \omega(l_s, t)\right] \tag{6.23}$$

$$ECa_{50}^2(l_s) = \begin{cases} \frac{(Ca_0)_{max}}{\sqrt{e^{B(l_s - l_0)} - 1}}, & \text{if } l_s > l_0 \\ 0, & \text{if } l_s < l_0. \end{cases} \tag{6.24}$$

Where B is a constant and l_0 is the sarcomere length below which there is no active tension developed. The time dependence of the active tension is described by the function ω, which is given by

$$\omega = \begin{cases} \pi(t - u)/t_0, & \text{if } 0 \leq t < t_0 \\ \pi(\frac{t - u - t_0}{t_r(l_s)} + 1), & \text{if } t_0 \leq t < t_0 + t_r \\ 0, & \text{if } t_0 + t_r \leq t. \end{cases} \tag{6.25}$$

where t_0 is the time to peak tension, u is the depolarisation time (equivalently the starting time of contraction) and t_r is the duration of the relaxation period described as a function of the sarcomere length

$$t_r = m l_s + b. \tag{6.26}$$

The active tension parameters presented in Guccione are reproduce in Table 6.2 and are fitted for a cylindrical representation of the left ventricle.

TABLE 6.2: Parameters for the active tension model used in [49].

Parameters	Units	Guccione
T_{max}	kPa	135.7
Ca_0	μM	4.35
$(Ca_0)_{max}$	μM	4.35
B	μm^{-1}	4.75
l_0	μm	1.58
t_0	ms	100
m	$s\mu m^{-1}$	1.0489
b	ms	-1.429

To validate the model, we reproduce the results shown in Guccione et al. [49], which demonstrate the active tension as a function of time for multiple sarcomere length choices in the deformed configuration. The full active tension cycle was reproduced for $t \in (0, 1000)\ ms$. These are presented in Figure 6.10.

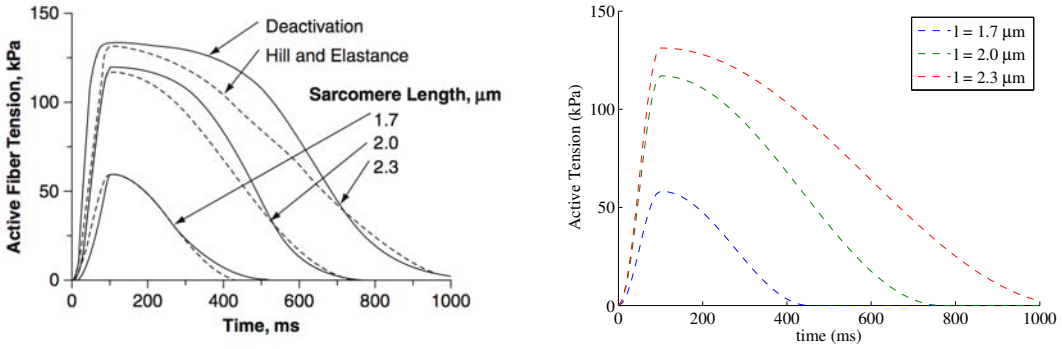

(a) (b)

FIGURE 6.10: Comparison between Guccione et al. [49] and our own implementation of active tension as a function of time for multiple sarcomere lengths. (a) Graph taken directly from Guccione et al. [49]. Comparison of isometric twitches predicted by the authors "deactivation" model and their "Hill" and "elastance" models at a range of sarcomere lengths. Our interest lies in reproducing the "Hill" and "elastance" model results, displayed by the dotted lines. (b) Reproduction of active tension results, for verification purposes. Modelling was performed in MATLAB using parameters from Table 6.2

Additional care must be taken for the choices of l_{s_0}, that is, the sarcomere length in the unloaded case. Literature values place the unloaded sarcomere length in the canine heart between the range of $2.0 - 2.28\mu m$ [80, 137]. However Guccione et al. [49] uses a constant sarcomere length l_{s_0} of $2.04\mu m$.

6.6 Boundary conditions

To model the cardiac cycle it is essential to specify boundary conditions that reflect the physiological function as close as possible, without introducing unnecessary complications. These boundary conditions can be divided into two categories: Dirchlet and Neumann. Dirchlet boundary conditions are required to prevent rigid body motion and to constrain the base of the heart. Neumann boundary conditions are required to simulate the blood filling the cavity which causes pressure to act on the endocardium of the left ventricle. The boundary conditions are best presented in conjunction with the corresponding phases of the cardiac cycle.

Throughout the full cycle

The inner ring at the base of the ellipsoid is occupied by the mitral and aortic valves. These valves govern the flow of blood in and out of the ventricle. The valves are relatively stiff and undergo very little deformation which motivates the constraint that the ring at the base of the ellipsoid model will undergo no displacement [78], and in the case of the *Cosserat* continuum, no rotation either such that

$$\mathbf{u} = \mathbf{0} \text{ on } \partial\mathcal{B}_D \qquad \text{and} \qquad \boldsymbol{\gamma} = \mathbf{0} \text{ on } \partial\mathcal{B}_D. \tag{6.27}$$

Additionally, the full base of the ellipsoid is fixed in the z-direction such that $u_z = 0$, providing a reference for deformation and strain, illustrated in Figure 6.11.

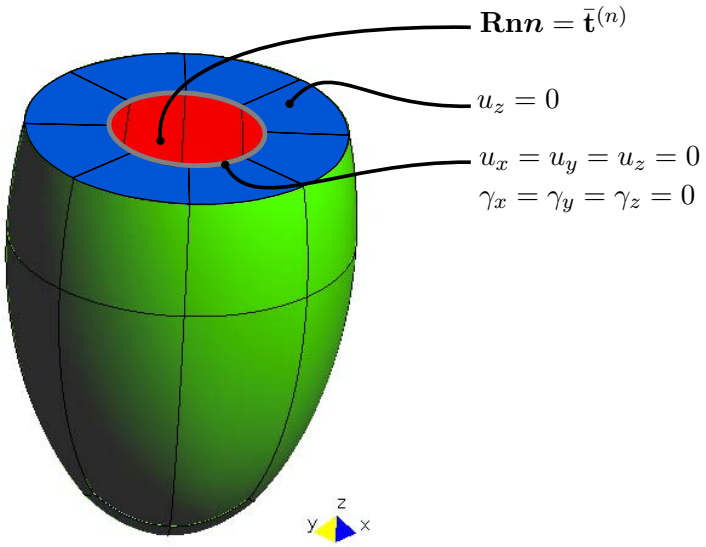

FIGURE 6.11: Boundary conditions enforced on the model geometry for the diastolic filling.

Passive filling

As blood fills the left ventricle the cavity volume increases and the endocardium experience pressure increases at a relatively proportionate rate. This phase is modelled by introducing a uniform pressure acting on the surface of the endocardium with normal $\mathbf{n}$

$$\mathbf{R}nn\mathbf{n} = \bar{\mathbf{t}}^{(\mathbf{n})} \text{ on } \partial\mathcal{B}_N. \tag{6.28}$$

These boundary conditions are expressed visually in Figure 6.11. There is no time dependency, but the nonlinearity of the problem requires the use of a Newton Raphson iterative scheme to solve the system of equations. The variational formulation is solved for incrementally increased pressures starting from $0kPa$ up until end diastolic pressure $1kPa$. The resulting deformed cavity solved at each loading step provides a set of pressure-volume data which can be compared with experimental results for quantitative analysis.

Isovolumetric contraction

In this stage of the cycle, the cavity volume V remains constant (the valves are closed while the cavity is full with a nearly incompressible fluid). The pressure in the cavity increases due to the contraction of the ventricle. This is caused by the introduction of active tension in the system. In this phase the cavity may deform but experiences no volume change. In this sense, the required pressure on the inner surface of the cavity is obtained iteratively with the additional requirement that $\Delta V = 0$. The active tension increases with time and as such the variational formulation is transient. The external work due to pressure, $p(t)$, which acts on the surface of the endocardium in the current configuration, at timestep i is given by

$$\int_{\partial\mathcal{B}_N} \mathbf{t}^{(\boldsymbol{\nu})} \cdot \delta\mathbf{u} \; da = \int_{\partial\mathcal{B}_N} p\boldsymbol{\nu} \cdot \delta\mathbf{u} \; da. \tag{6.29}$$

Where $\boldsymbol{\nu}$ is the normal to the surface da. In order to relate this to the formulation of external work in the material configuration presented in Eq. (3.12), we utilize Eq. (2.12) to produce

$$\int_{\partial\mathcal{B}_N} p\boldsymbol{\nu} \cdot \delta\mathbf{u} \; da = \int_{\partial\mathcal{B}_N} pJ\mathbf{F}^{-T}\mathbf{n} \cdot \delta\mathbf{u} \; dA. \tag{6.30}$$

Ejection

The cavity volume decreases as blood is expelled from the contracting left ventricle. The same formulation for the previous phase is used, however for ejection, the volume

decreases with time such that $\Delta V_n \neq 0$. The calculation of ΔV is found through solving for the flow rate I_{ao} and aortic pressure P_{ao}, of the three element Windkessel model [154]. This is expressed as the differential equation

$$(CR_0)\frac{dI_{ao}}{dt} + \left(1 + \frac{R_0}{R}\right) I_{ao} = (C)\frac{dP_{ao}}{dt} + \left(\frac{1}{R}\right) P_{ao}. \tag{6.31}$$

Where C, the arterial compliance, R, the peripheral resistance and R_0, the flow resistance, are material parameters.

The target volume increment obtained is then utilized to find an appropriate pressure. The Neumann conditions remain the same as the previous phase, with the time dependence of the problem still being controlled by the active tension model. Ejection begins when the pressure in the left ventricle exceeds the pressure in the aorta. Once the cavity pressure drops below this threshold, the aortic valve closes ending the ejection phase.

Isovolumic relaxation

Once the cavity ceases to contract further the aortic valve closes and the ventricle relaxes. The cavity volume remains constant, similar to the Isovolumetric phase. The boundary conditions are almost exactly the same to isovolumetric phase except now the pressure decreases with time, as the active tension declines to zero.

Cardiovascular disease

In a healthy functioning heart the coronary arteries supply the myocardial tissue with oxygenated blood. Acute myocardial infarction (MI), more commonly known as a heart attack, occurs when blood flow from a coronary artery is restricted to the point that insufficient blood flow reaches the heart tissue causing ischemia, and myocyte cell death [70]. This is usually the result from a build up of fat deposits or blood clotting that occupies the whole cross section of the blood vessel, restricting blood flow. The myocardium cells dependant on the supply of oxygenated blood and nutrients downstream of the blockage subsequently die, forming a scar of dead cells which hampers cardiac function.

The size and mechanical properties of the infarct (which change during the healing process) govern the level of impairment the heart function [23, 56, 106]. The infarct can negatively affect the heart function in a number of ways. Some key functional impairments are:

1. A higher stress measurement in the infarction region [53], which exposes the region to the risk of rupturing.
2. A stiffer infarct region directly affects diastolic performance, limiting the cavity volume [11].
3. A compliant infarct limits the systolic function, lowering the stroke volume [11].
4. Bulging may occur at the infarct and border region, resulting in ventricular remodelling and permanent structural changes in the ventricle dimensions [105].

Since the scar of the myocardial infarction changes with time, the associated physiological and mechanical properties of each stage will be elaborated, by making use of the work presented in Holmes et al. [56].

Acute Ischemia: The acute ischemia stage is an early phase of the infarct process that lasts for a few hours, during which the overall ventricular compliance increases. The scar starts its formation and any loading condition influences its final shape. The wall at this region undergoes thinning and stretching during this period. Due to the myocardial cell death, the infarct region behaves only as a passive nonlinear viscoelastic material (quite similar to the normal passive behaviour of normal heart tissue) with higher stresses. At the end of the process, the scar is much stiffer than healthy tissue.

Necrotic: In the next few days following the MI, the infarct starts to heal. Fibroblast and collagen are deposited in this area to support the growth of healthy tissue. Necrotic stage represents the most critical phase of an infarct, as the infarct has the highest risk of rupturing during this period. A mild thinning still takes place as the dead cells start to leave the region resulting in a small increase in wall stress.

Fibrotic: The fibrotic stage is associated with dramatic increases in fibroblast and collagen deposits in the infarct region. This whole process can take up to a few weeks or even months. During this time, the infarct region becomes very stiff [53], limiting the compliance of the surrounding healthy myocardium during the diastolic phase. Stiffness of the infarct region correlates to the amount of collagen content in the region.

Remodelling: The remodelling is an on going process of the healing mechanism, with no definitive end. Structurally the infarct scar begins to shrink and occupies a reduced percentage of the ventricular wall. The amount of collagen content continues to increase, albeit at a reduced rate, while the stiffness of the infarct starts to decrease. The infarct region will remain stiffer than the surrounding myocardium, however ventricular function does improve with time.

Chapter 7

Results and discussion

The primary goal of this study is to investigate the performance of a suitable *Cosserat* fibre continuum approach in the application of cardiac mechanics.

In this chapter the results of several cardiac mechanics simulations are presented. First the calibration of the material parameters are considered. This was achieved by comparing numerical simulation to appropriate experimental results found in the literature. In the case of the nonlinear constitutive law an optimization algorithm was employed to ensure the closest fit to experimental results was achieved.

The resulting pressure and volume relationships, deformation modes and stress analysis are discussed and compared to the literature.

7.1 Linear model

7.1.1 Homogenized approach

The following section presents the results corresponding to the material model introduced in Section 5.2.1. To model the fibres as one dimensional *Cosserat* rods homogenised within a three dimensional ECM space, we will need to be able to separate the material properties into their respective components. While there is experimental data available for cardiovascular tissue; most notably Demer and Yin [28] and Dokos et al. [30], who performed biaxial and shearing experiments respectively, the data sets proved unsuitable for linear model parameter calibration due to the highly nonlinear material behaviour.

Rather, we calibrated our model using a previously verified computational model of the rat left myocardium [82]. Calibration employed specific computational experiments

investigating simple tension, simple shear and four point bending. The boundary conditions for each experiment are illustrated in the Figures 7.1 - 7.3 and are given by the following problem descriptions outlined below.

Axial tension: The specimen tissue started as cube with dimensions $1mm \times 1mm \times 1mm$. The tension experiment is Dirichlet controlled specifying displacement constraints on two opposite faces of the cube and leaving the remaining faces as free surfaces. Following the illustration in Figure 7.1, the first Dirichlet condition specifies a uniform displacement in the x-direction of $0.01mm$ (1% of the cube's width). On the opposite surface, the cube is fixed in the x-direction to prevent rigid body translation. Additionally, the rotational degrees of freedom are fixed on this surface.

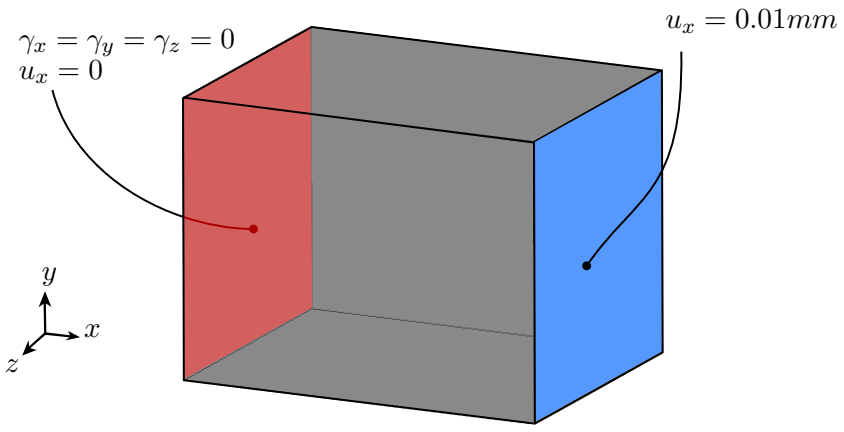

FIGURE 7.1: Axial tension: Illustration of the axial tension experiment. The red surface parallel to the zy-plane was fixed while the blue surface was extended in the x-direction.

Simple shear: The specimen tissue started as cube with dimensions $1mm \times 1mm \times 1mm$. The shear experiment is also Dirichlet controlled. The first Dirichlet condition is prescribed on the top surface, with normal in the y-direction. This is the displacement constraint specifying a uniform displacement in the x-direction of $0.01mm$ (1% of the cube's width) across the whole top surface. The bottom of the cube was fixed in all directions and rotations, to prevent rigid body displacements. Further Dirichlet conditions on the top face and on two parallel side faces prevent the cube from contracting in the y-direction, ensuring the correct deformation occurs.

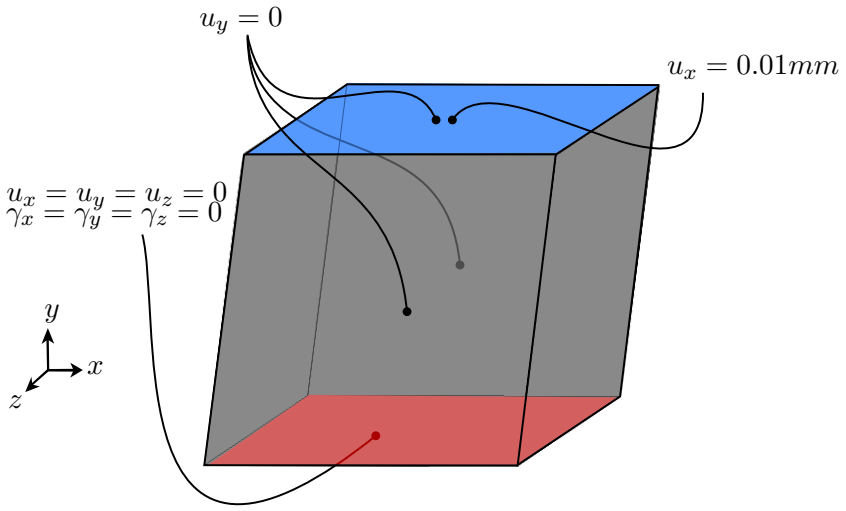

FIGURE 7.2: Simple shear: Illustration of the simple shear experiment. The red surface parallel to the zx-plane was fixed while the blue surface was extended in the x-direction.

Four point bending: The specimen tissue started as rectangular prism with dimensions $9mm \times 1.5mm \times 1.5mm$. Dirichlet and Neumann constraints were prescribed to ensure pure bending deformation occurred. Dirichlet conditions on one outer surface parallel with the cross section of the beam (i.e the yz-plane) fixed rotation deformation about the x and y axis. Additionally, secondary Dirichlet conditions fixed the line segments highlighted in Figure 7.3, in the y-direction, to resist the loading and ensure bending deformation occurs. The highlighted points on the closer side of each line segment was fixed in the z-direction to prevent any spurious rotation of the body. Additionally one of the points was also fixed in the x-direction. On the top surface, spaced equally from the centre, four point loads of $-0.02kPa$ were applied in the y-direction. The loading was imposed to ensure a midpoint deflection of 2.5% of the beam's length was achieved.

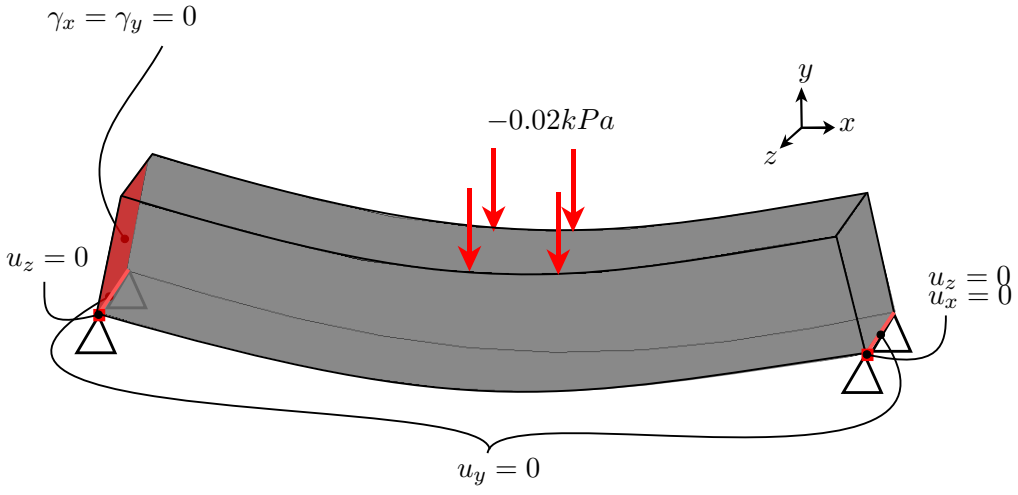

FIGURE 7.3: Pure bending: Illustration of the pure bending experiment.

It should be noted that rotation boundary conditions only apply to the experiments using the *Cosserat* fibre continuum, and without them the computational experiments were ill defined.

The samples of comparison tissue specimens were composed utilizing the constitutive implementation of Usyk et al. [148]. The strain energy function is detailed in Section 6.4, and the material parameters from the model are presented in Table 7.1 below.

TABLE 7.1: Strain energy function coefficients for the comparative "reference" material used to calibrate the linear *Cosserat* fibre material model.

Parameter	Value
b_{ff}	9.2
b_{tt}	2.0
b_{nn}	2.0
b_{ft}	6.4
b_{fn}	6.4
b_{nt}	1.0

The indices in Table 7.1 refer to components aligned with fibre axis, f, sheet-tangent axis t, and sheet-normal axis, n. Additionally the scaling parameters for healthy tissue $A = 1\,kPa$ and $A_{comp} = 100\,kPa$ were used. For more details on this model and it's calibration, one can consult [82].

The corresponding *Cosserat* fibre model was successfully calibrated in each experiment (simple tension, simple shear and four-point bending) to within a tolerance of 0.05% of comparable stresses (or in the case of bending, with midpoint deflection).

The following parameters are a result of the healthy tissue calibration:

TABLE 7.2: Material properties for the linear *Cosserat* fibre constitutive law, modelling healthy cardiac tissue.

Parameter	Symbol	Fibre	EC matrix
Volume fraction	vol	67.6%[22]	33.3%
Axial stiffness	E (kPa)	10.82	7.10
Shear Stiffness	G (kPa)	4.49	2.37
Characteristic length	l	0.59	-

It should be noted that the condition of near incompressibility is assumed for the isotropic ECM, as such Poisson's ration ν is modelled as 0.4999. This allows us to calibrate for only E_{ECM} and calculate G_{ECM} accordingly.

Unlike classical formulations, *Cosserat* fibre continuum theory accounts for the influence of neighbouring material points through the introduction of change of curvature strains and couple stresses in the kinematics and constitutive laws of the problem. These

contributions are scaled by the characteristic length l which is a direct and elegant method of including information about the micro structure.

To further illustrate this, we consider the benchmark test of the beam bending example outlined above for multiple values of the characteristic length, which is presented in Section 7.1.2.

7.1.2 Non-homogenized approach

The non-homogenised approach removes the need for volume fractions. As a result, we can calibrate material properties relating the deformation of "fibre specific" deformation modes directly to the fibre bundle's material properties. Additionally the computation requirements become significantly more streamlined; there is no need to loop through the various contributions and homogenise.

These advantages make the non-homogenised approach preferable in performing computational analysis. Additionally, as the material is no longer homogenised, it becomes necessary to model the incompressibility separately as opposed to the homogenised approach, whereby the incompressibility is handled via the isotropic ECM. The full stored energy function is given by Eq. (5.2). The calibration procedure of the constitutive law was carried out in the same manner as outlined in the previous section. The non-homogenised *Cosserat* fibre model was successfully calibrated to within a tolerance of 0.05% of comparable stresses (or in the case of bending, with midpoint deflection). The material parameters for healthy tissue is presented in Table 7.3.

TABLE 7.3: Material properties for non-homogenized linear *Cosserat* fibre constitutive law, modelling healthy cardiac tissue.

Parameter	Symbol	Fibre	EC matrix
Axial stiffness	$E \ \ (kPa)$	18.389	3.12
Shear Stiffness	$G \ \ (kPa)$	2.996	1.37
characteristic length	l	0.339	-
Incompressibility	A_{comp}	20.0	-

Of particular interest is the effect the characteristic length has on the resulting deformation of the problem. The four point beam bending example outlined in the previous section (illustrated in Figure 7.3), introduced flexural strains under deformation. Changing the characteristic length scales the stiffness contributions in the constitutive laws corresponding to flexural strains, and as a result, we should see decreases deformation with increases in l. To investigate this, while still remaining in the small strain range, we employed incremental loading from $0 - 0.02\ kPa$ with multiple experiments with different values for the characteristic length l.

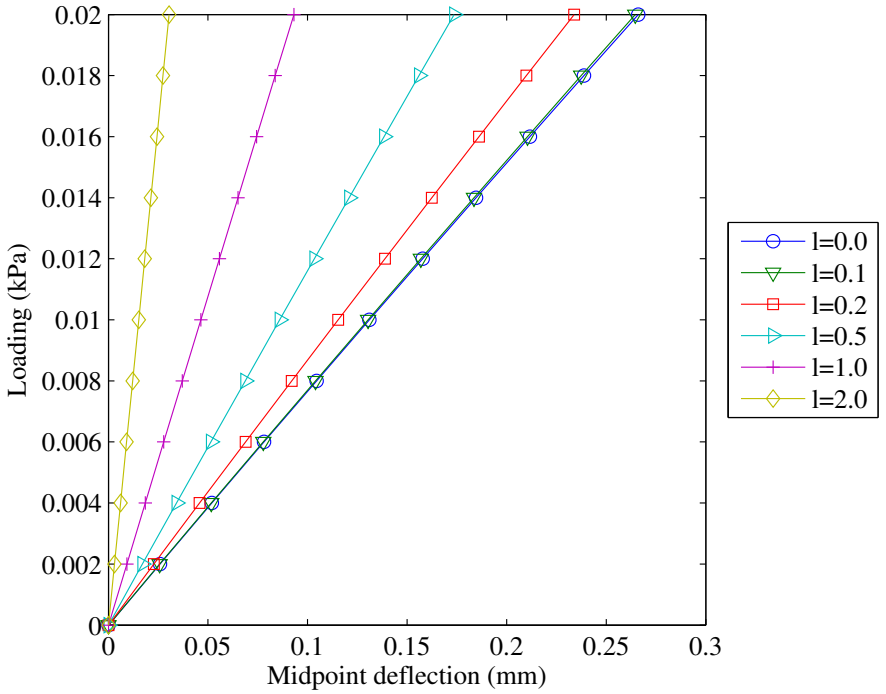

FIGURE 7.4: Midpoint deflection results for multiple choices of characteristic length l undergoing loading in a typical four point beam bending experiment. Results are presented for loads ranging from $0 - 0.02kPa$. As the results are presented in absolute deflection, the far right line (—○—) corresponds to the *least* stiff response.

The full set of results are displayed in Figure 7.4. These results very clearly illustrate that for increases in the values of l, the material becomes stiffer. This verifies that a measure of the micro space is being successfully integrated into the macro behaviour of the material. For the sake of comparison, we include the reference case where $l = 0.0$, i.e the higher order terms are removed from the kinematics and constitutive laws of the problem description. This allows as us to clearly identify and compare the influence of the higher order stiffness parameters in the kinematics and constitute laws governing the deformation.

One could consider that for *very* small choices of l, the influences are negligible. Also, noticing the non uniform changes in deflection for increases in l, motivates a more thorough investigation into the relationship between the stiffening of the beam and the size of l.

We explore a larger range of values for l for the same problem description (i.e loading from $0 - 0.02\ kPa$) and for each experiment analyse the average change in strain for the full loading period. In this sense we can meaningfully identify and quantify the change in stiffness as a function of the length scale. The results are presented in Figure 7.5.

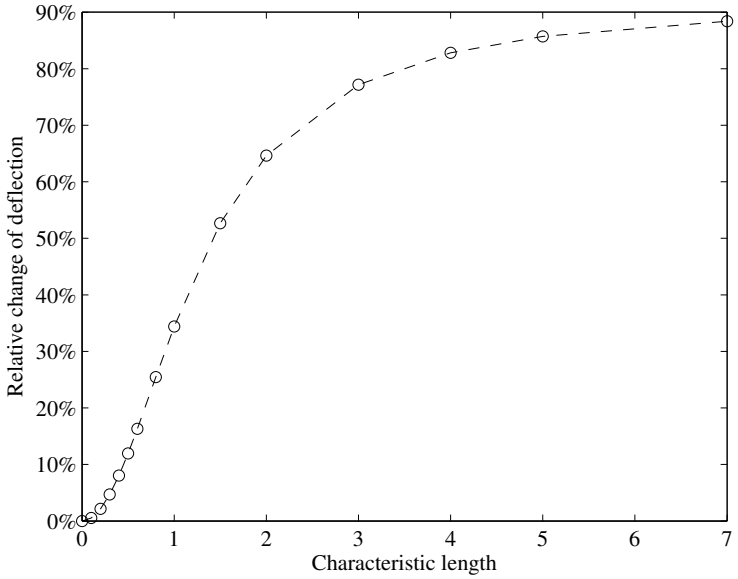

FIGURE 7.5: Influence the size of the chosen characteristic length on the overall change in midpoint deflection to the classical case. Results presented are averaged over the full loading cycle $0 - 0.02kPa$.

The results in Figure 7.5 follow what one should expect in this type of problem. For small values of l, near the reference case whereby the nonlinear contributions are first noticed, the increase of l has an almost exponential affect. However once l starts getting too large, the stiffness of the beam dominates the problem and the resulting deformation of the beam tends towards a zero deformation case which corresponds to a 100% change in strain.

Application to cardiac mechanics

The problems outlined above are applicable to sample specimens, and perhaps isolated portions of cardiac tissue. The next phase of computational experiments must explore the application of the linear constitutive law on a more complex structure. For the next experiment, we investigate modelling the diastolic filling stage of the cardiac cycle with this linear *Cosserat* fibre constitutive law. We wish to determine the extent to which the linear model is able to capture and model realistic cardiac function.

Passive filling refers to the stage in diastole where the left ventricle is filled with oxygenated blood. As the cavity increases, due to the inflow of blood, the cavity exerts pressure on the endocardium, causing the entire structure to dilate and expand. Additionally, the left ventricle experiences mild torsional deformation (which is more predominant at the apex), and an overall extension [15, 108, 110]. The end diastolic pressure (EDP) for

the adult rat has been recorded to be in the range $0.44 - 2.0kPa$ [24, 38, 67, 127, 146], but the majority of data suggests the mean to be valued closely to $1kPa$.

The experimental data sets of Herrmann et al. [55], Omens et al. [101] and Cingolani et al. [21] are used to validate and verify the computational model results. Fibre orientation for the computational results are described in Eqs. (6.5) - (6.7). Boundary conditions of the problem description are outlined in Section 6.6, and correspond to the illustration in Figure 6.11. As an initial investigation, a coarse mesh given by 315 particles and corresponding to 1830 degrees of freedom, was chosen. The computational model was subjected to pressure loading up until $1.6kPa$. The linear model, Eq. (5.2), was able to experience significant deformation, well within the range of experimental results, and to a degree was able to capture appropriate deformation expected in this stage of cardiac function. Figure 7.6 shows the pressure volume relationship for the loading experiment. Positions A-D have been marked on the figure and further analysis is presented at these points.

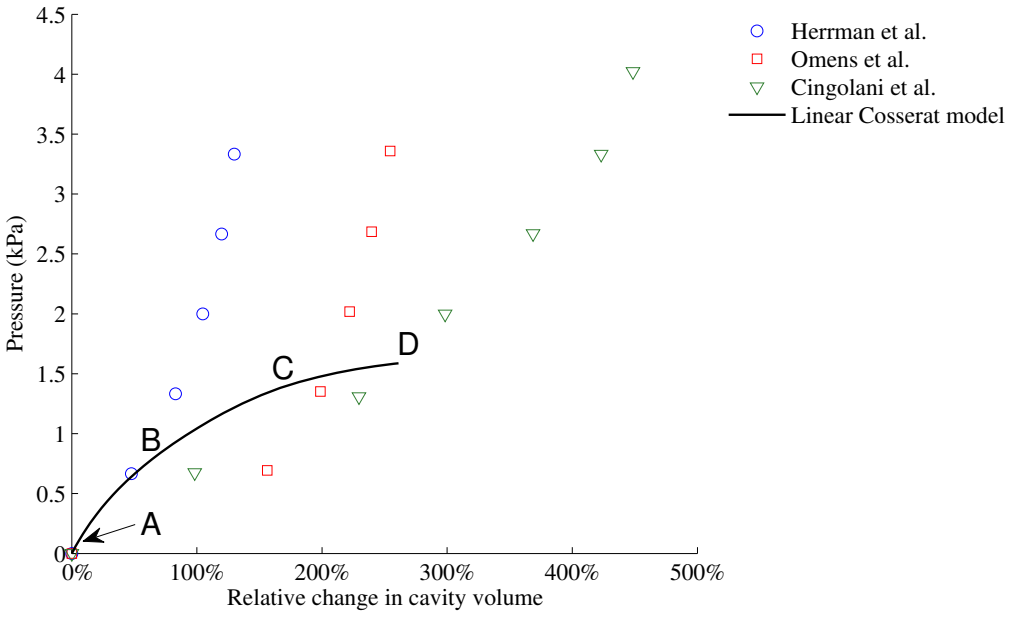

FIGURE 7.6: Passive material response of an ellipsoid model of the rat left ventricle. The *Cosserat* fibre model implemented with a linear non-homogenised constitutive law (Eq. (5.2)) was used and calibrated to provide results that best reflect the experimental results provided by Herrmann et al. [55], Omens et al. [101] and Cingolani et al. [21]. Labelled positions A-D have been chosen for more in depth analysis.

In Figure 7.6 we see the model starting in the undeformed case (A), and increasing in volume and pressure through positions (B-D). Figure 7.7 captures the deformation of the model at the labelled stages, and clearly illustrates ventricular dilation and extension. Figure 7.8, displaying only half of the geometry, is able to better illustrate the

torsional deformation. These deformation modes exhibited by the model are encouraging and meet the qualitative expectations for a cardiac model. While the correct deformation modes are captured, and the results of the pressure volume experiment fall within the experimental range, the linear constitutive model is fundamentally unsuitable for modelling biological tissue.

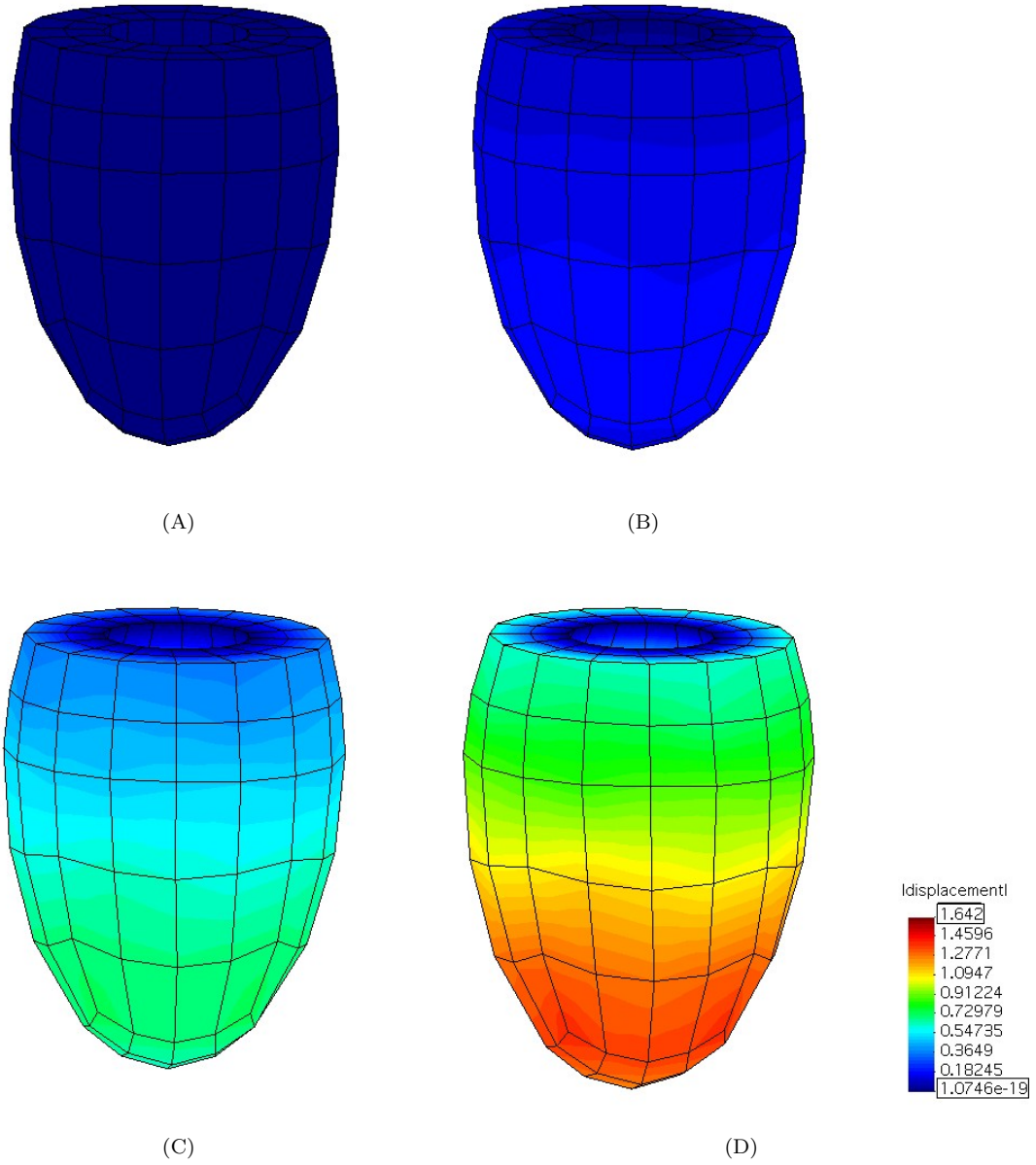

FIGURE 7.7: Displacement plots of the computational model of the left ventricle undergoing diastolic filling at various stages (A-D) corresponding to positions labelled in Figure 7.6.

The relationship between pressure and volume is dominated by the geometry of the problem, with the volume expanding at an almost cubic rate with respect to pressure. This contradicts experimental results that show cardiac tissue becomes increasingly stiffer

for larger strains. Physiologically the perimysial collagen fibres, in the near unloaded state are wavy, and allow for the material to deform easily under initial loading. While deforming, these fibres straighten and become resistive to further stretching, making the material increasingly difficult to deform [54]. This type of material behaviour usually results an almost exponential stress-strain relationship.

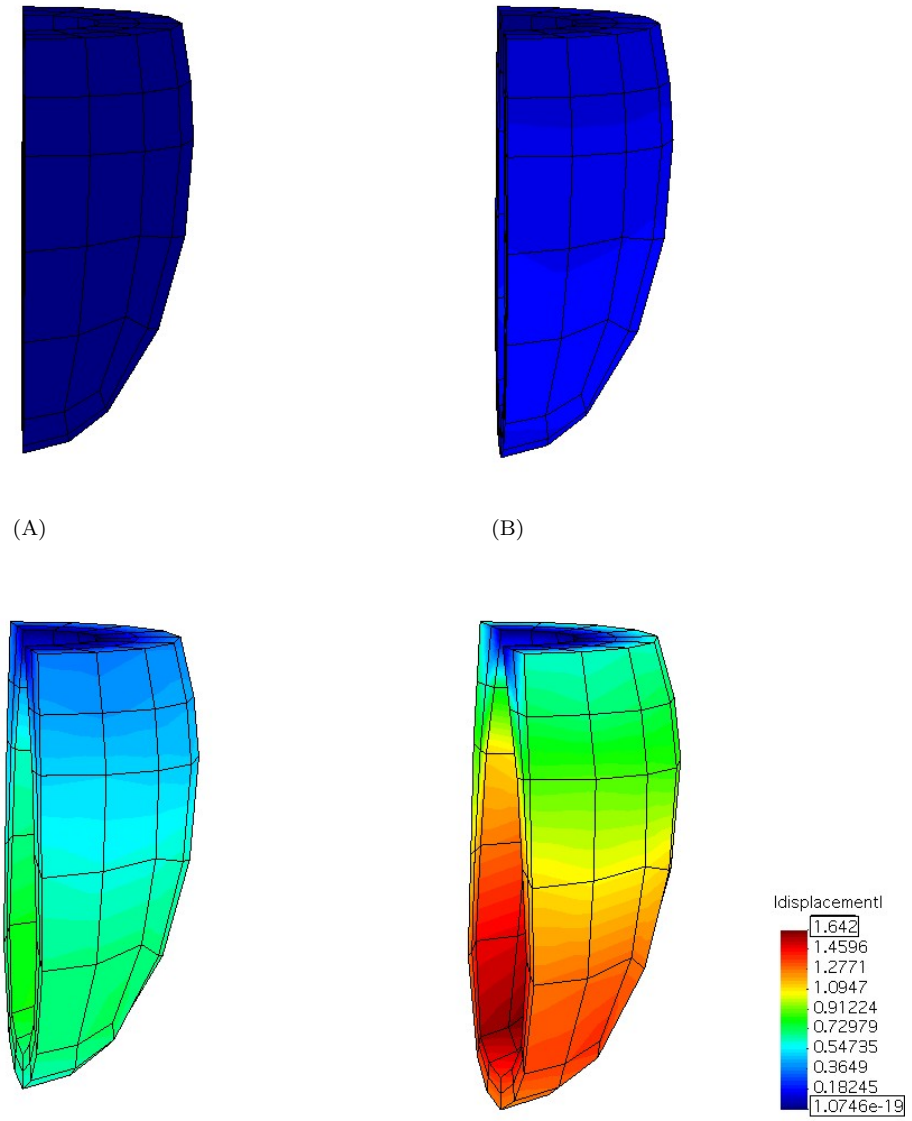

FIGURE 7.8: Displacement plots of one half of the computational model of the left ventricle undergoing diastolic filling at various stages (A-D) corresponding to positions labelled in Figure 7.6.

We can conclude from this experiment that the linear model may be able to capture small strain behaviour correctly but it is not suitable for complex and meaningful cardiac mechanics problems. This motivates the need for the nonlinear constitutive law

introduced in Section 5.3 and the abandonment of further analysis into the use of the linear constitutive law.

7.2 Nonlinear model

A generalized continuum problem with nonlinear constitutive laws applied to a nonlinear geometry like the left ventricle is a sophisticated and complex problem. Even in the passive state, stresses are coupled including influences from both **U** and **K**. In the active state, time dependence is introduced into the problem, as well as a coupled electromechanical responses dependant on fibre orientation, sarcomere length and time. The systolic phase is further divided into isovolumetric contraction and ejection, with each phase introducing additional complexities.

Passive response

The procedure and accompanying methods introduced to calibrate the linear constitutive law were introduced as a means to overcome the lack of experimental data available in the small strain range. This is no longer a problem for the nonlinear model Eq. (5.13), as it is suitable for large strain deformation. It is therefore appropriate that the calibration of the nonlinear model uses experimental data sets for cardiac tissue directly. The computational experiments investigating simple tension, simple shear and four point bending (Figures 7.1 - 7.3), can be utilized to explore that the model exhibits nonlinear behaviour and, in the case of bending, that changes of the characteristic length appropriately influence the passive mechanical response of the model.

Prior to calibration, the material parameters given in the Niederer and Smith [96] paper were adapted for the use of our model. This was done by setting the material stiffness for shear strains relating to the ECM as homogeneous. As none of the curvature strains are activated in the simple shear and simple tension, the characteristic length choice for these problems is trivial and set to 0.0. These parameters are presented in Table 7.4.

The deformation for simple tension and simple shear were performed and nonlinear material behaviour was definitely present. Simple plots illustrating the nonlinear relationship between stress and strain are presented in Figure 7.9.

The four point beam bending analysis presented for the linear model is repeated for the nonlinear model. The only difference in experimental design was to increase the

TABLE 7.4: Material properties for nonlinear *Cosserat* fibre constitutive law, modelling cardiac tissue.

Parameter	Symbol	Value
Principle fibre modulus	a_1	9.20
Shear fibre modulus	a_2	3.70
Principle matrix modulus	b_1	2.00
Shear matrix modulus	b_2	2.00
Characteristic length	l	0.00
Stress Scaling 1	A	0.30
Stress Scaling 2	B	1.00
Incompressibility	A_{comp}	20.0

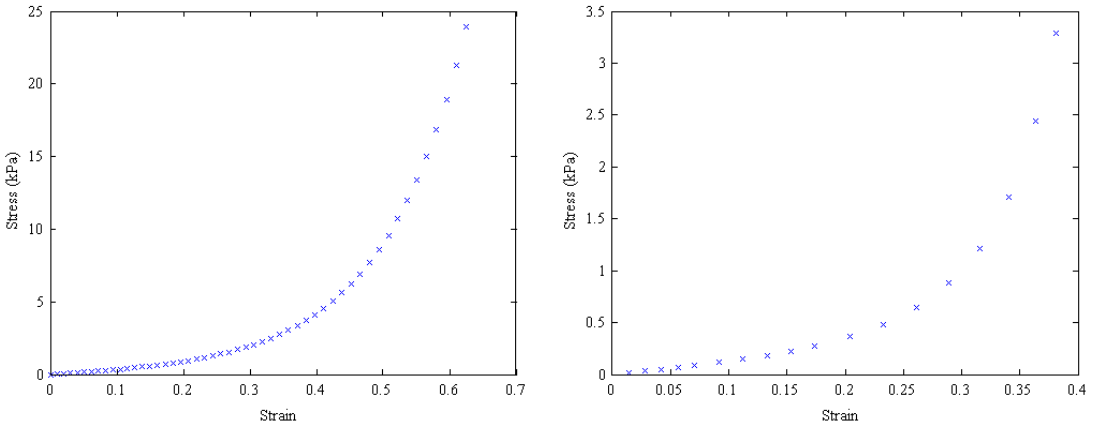

(a) Principle stress-strain relationship for the tension block experiment.

(b) Shear stress-strain relationship for the shear block experiment.

FIGURE 7.9: Nonlinearity expected in the material response is validated when analysing the stress strain relationships exhibited during shear and axial deformation.

loading to ensure deformation in the nonlinear strain range. This corresponded to incremental loading from $0 - 0.16\ kPa$ for multiple experiments with different values for the characteristic length l.

The full set of results are displayed in Figure 7.10. These results illustrate the findings for the nonlinear case: that a measure of the micro space, is being successfully integrated into the macro behaviour of the material. Additionally, the nonlinearity of the material is prominently displayed in the results. For larger displacements, exponential loading increments are required to produce further deformation.

The relationship between the size of the characteristic length l and the stiffening affect on the beam is explored as it was for the linear case. The results are presented in Figure 7.11 and show that the same behaviour exists in the nonlinear case as we encountered in the linear case (see Figure 7.5). One does note that the size of l has a slightly less dramatic influence than the linear case, (the slope of the graph for $l < 2.0$ does not

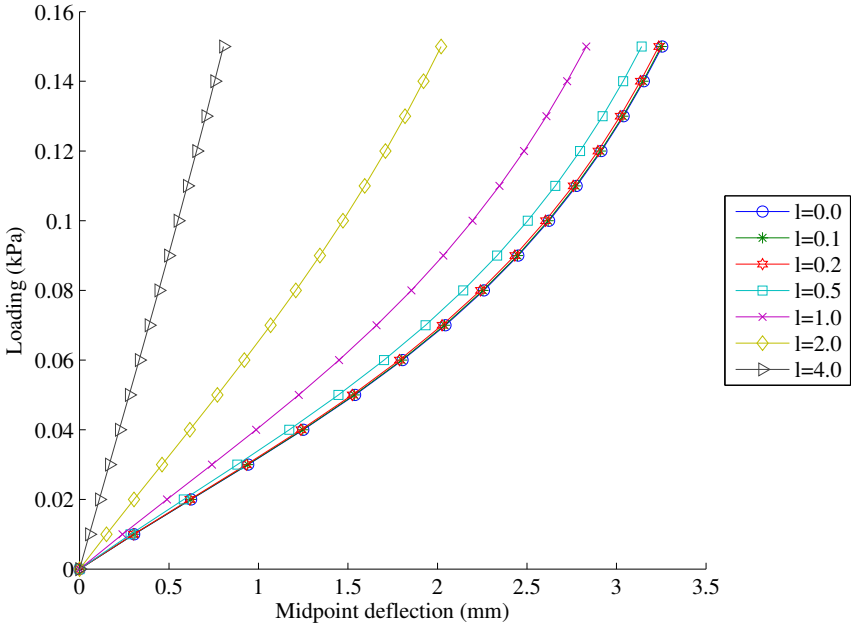

FIGURE 7.10: Midpoint deflection results for multiple choices of characteristic length l undergoing loading in a typical four point beam bending experiment. Results are presented for loads ranging from $0 - 0.15kPa$. As the results are presented in absolute deflection, the far right line (—○—) corresponds to the *least* stiff response.

increase as rapidly as the linear case). In the linear case the inclusion of l, introduced nonlinear kinematics into the problem. In the nonlinear case, the inclusion of l merely increases the nonlinearity of the problem.

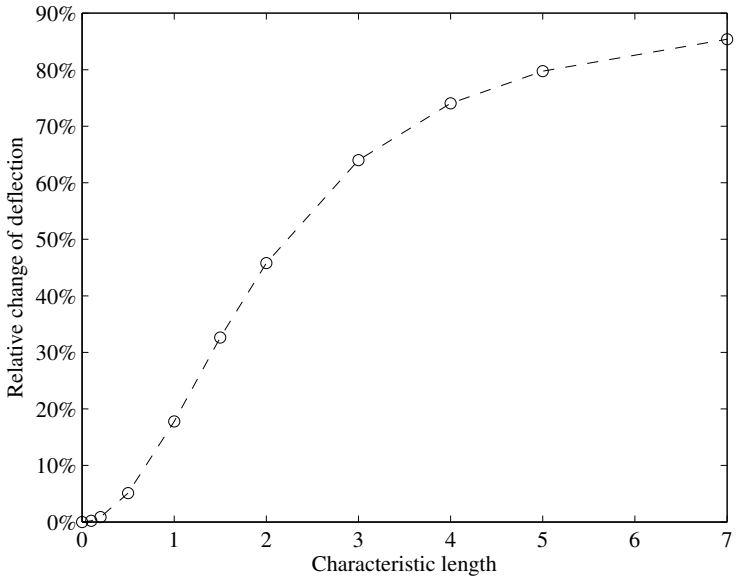

FIGURE 7.11: Influence the size of the chosen characteristic length on the overall change in midpoint deflection to the classical case. Results presented are averaged over the full loading cycle $0 - 0.15kPa$.

Finally, a stress analysis of the problem illustrates that couple stresses $\boldsymbol{\xi}$, given by Eq. (3.22) exist only in the one dimensional fibre space. With the fibre aligned along the x-direction, the only significant couple stress is the component of the tensor ξ_{xy} which corresponds with bending in the y direction. Analysis of the effective couple stress given by $(1.5\boldsymbol{\xi} : \boldsymbol{\xi})^{\frac{1}{2}}$, in Figure 7.12 shows this, as it has an almost identical stress profile as ξ_{xy}, which is to be expected in a bending problem.

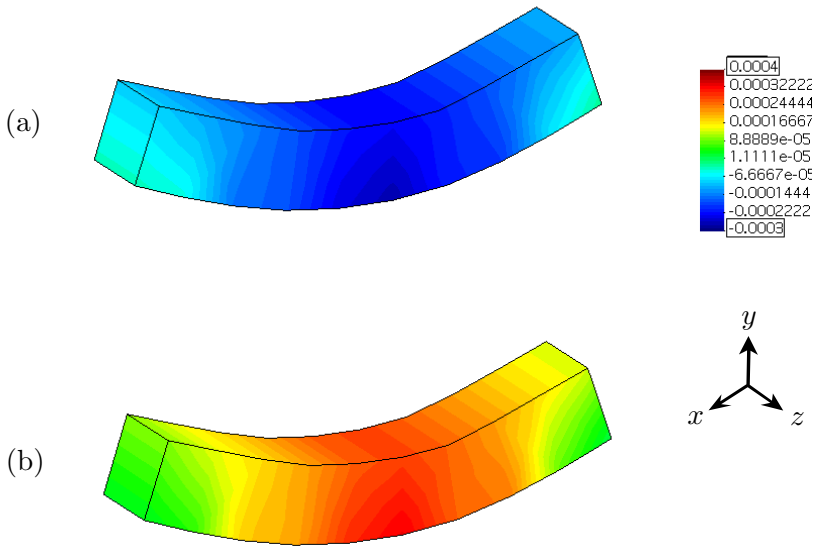

FIGURE 7.12: Sample specimen from the bending experiment. (a) Contour plot of the couple stress ξ_{xy} given in kPa. (b) Contour plot of the effective couple stress given in kPa.

Similar results are found for torsion experiments. Consider the same beam in the previous example with a problem description of pure torsion.

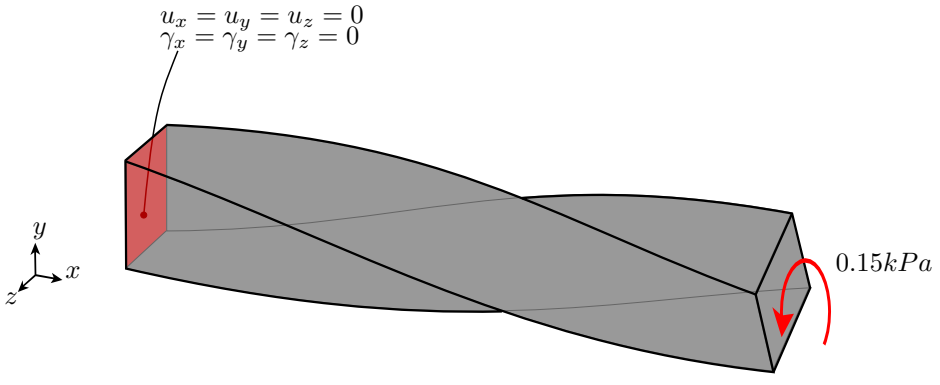

FIGURE 7.13: Pure torsion: Illustration of the pure torsion experiment.

Pure torsion: The specimen tissue started as rectangular prism with dimensions $9mm \times 1.5mm \times 1.5mm$. Dirichlet and Neumann constraints were prescribed to ensure simple torsion occurred as illustrated in Figure 7.13. Dirichlet conditions on one

outer surface parallel with the cross section of the beam (i.e the yz-plane) fixed all displacement and rotation deformation (i.e. $u_x = u_y = u_z = \gamma_x = \gamma_y = \gamma_z = 0$). On the opposite end of the beam, across the surface, a surface moment of $1.5kPa$ was applied counter clockwise. In this experiment, the only significant change of curvature strain corresponds to the fibre experiencing torsion (i.e. K_{ff}).

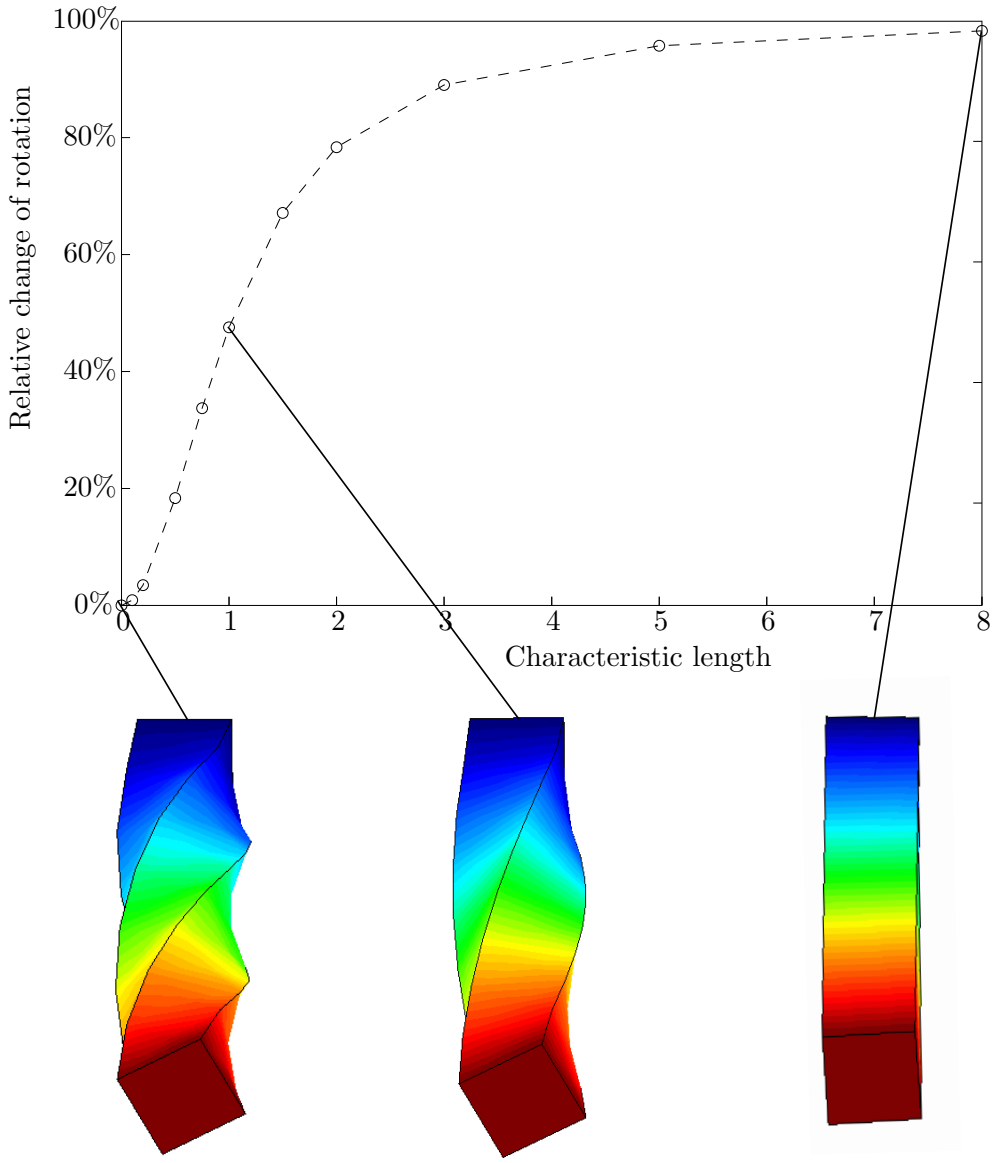

FIGURE 7.14: Influence the size of the chosen characteristic length on the twisting of a beam. Results are presented for a final load of $0.15kPa$, and are accompanied with the deformed configuration for various choices of l.

In Figure 7.14, the effect of the characteristic length l is once again illustrated. It is important to note that the increase in l only increases the material stiffness when

higher order strains are activated during deformation (i.e. the deformation of the beam undergoing tension in the direction of the fibre, would not be affected by changes in l).

Additionally, the tissue specimens undergoing torsion experienced contraction during twisting, which is an encouraging material response. Contraction under twisting is not experienced in all elastic solids, as shown by the original work of Poynting [107], however this type of behaviour, also known as a *reverse Poynting* effect, has been experimentally observed for specimens of rabbit papillary muscles [62].

Calibration

The proposed transverse isotropic model in Eq. (5.13) has four material anisotropy parameters a_1, a_2, b_1 and b_2; two stress scaling parameters A and A_{comp}, relating to material stress and incompressibility respectively; an exponential scaling parameter B; and the characteristic length l which is a feature of the micro structure.

The availability of experimental data suitable for the calibration of cardiac tissue is limited. The most comprehensive study investigating orthotropy was performed by Dokos et al. [30] in which cubic sections cut from a porcine left ventricle were subject to shear loads. The experiment was performed to include all six combinations of fibre orientation and shear deformation as illustrated in Figure 7.15. We utilize a common assumption that one mammalian specific cardiac material behaves in a similar manner to other mammalian cardiac tissue [31], this assumption will allow us to calibrate the material anisotropy parameters (l, a_1, a_2, b_1 and b_2) directly using the shear experiments. To be thorough in our material parameter calibration we would need to apply a secondary calibration to obtain the remaining "scaling" parameters to fit animal specific models using experimental data pertaining directly to the animal in question. In this sense the scaling parameters A and B are considered specific material parameters for a given species. The other material parameters l, a_1, a_2, b_1 and b_2 are considered universal cardiac tissue parameters that govern the anisotropy and include a feature of the micro structure, these remain unchanged from species to species.

The data of Dokos et al. [30], see Figure 7.18(a), indicate that the shear response is stiffest when the plane orthogonal to the fibre direction is extended, least stiff when the plane orthogonal to the normal direction is extended (this can be viewed as the deformation of sheets sliding over each other) and has intermediate stiffness when the plane normal to the sheet direction is extended. We follow the approach of Holzapfel and Ogden [58], who noticed that the ordering of the labels fn and fs in the original result of Dokos et al. [29] (see page 5, Figure 6 of [30]) is inconsistent with the data shown in the other figures presented in that paper. To rectify this, we have switched

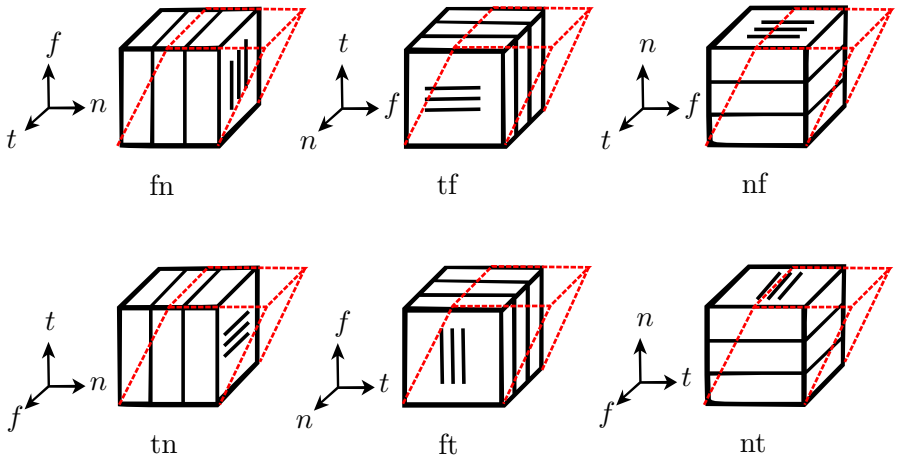

FIGURE 7.15: Sketches of six possible modes of shear for orthotropic myocardium defined with respect to the fibre axis f, sheet-tangent axis t and sheet-normal axis n. The modes are designated (ij), where $i, j \in \{f, t, n\}$, corresponding to shear in the ij plane with shear in the j direction. Thus, the first letter in (ij) denotes the normal vector of the face that is shifted by the simple shear, whereas the second denotes the direction in which that face is shifted. The modes in which the fibres are stretched are (fn) and (ft).

the labels of fs and fn in Figure 7.18(a) to match the data sets used in Holzapfel and Ogden [58].

For the special case of calibrating transverse isotropy, we recognise that the total combinations of fibre orientation and shear deformation reduces to three possible cases as put forward in Figure 7.16.

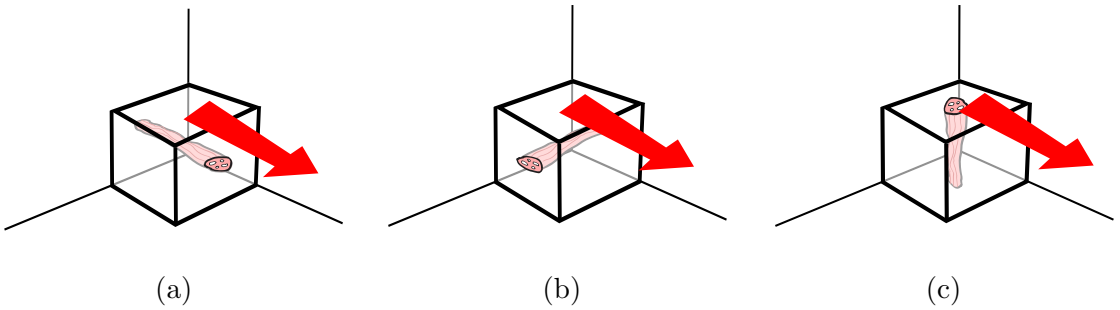

FIGURE 7.16: Sketches of the three possible modes of shear for transverse isotropic myocardium: (a) A transverse plane shifted towards the fibre direction, (b) a transverse plane shifted towards the other transverse plane and lastly (c) the fibre plane shifted towards a transverse plane.

The specimen cubes used in the shear experiments of Dokos et al. [30], had a natural variation in the fibre orientation. The cube dimensions were $3mm \times 3mm \times 3mm$, extracted from the midwall of the left ventricle and rejected if there was a change in fibre orientation amounting to more than 30° across the cube. In order to represent this in our shear experiments, and following the work of Hussan et al. [66], we specify a mean fibre orientation in our cube and allow for that orientation to vary. The variation

of the fibre orientation is considered a smooth function of one transverse direction. This results in the fibre direction on one side of the cube orientated $+15^{o}$ from the mean direction and -15^{o} on the opposite side.

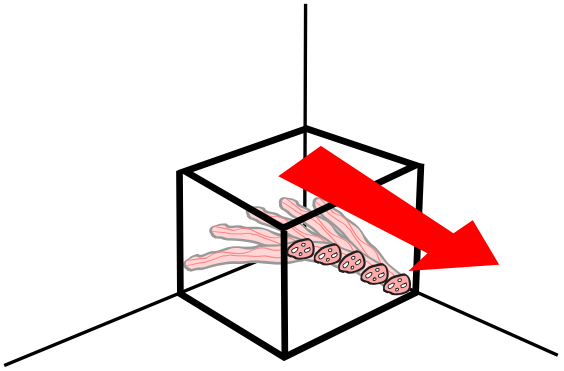

FIGURE 7.17: Illustration of the varying fibre orientation throughout the cube. Mean fibre orientation is established by varying the fibre direction slightly to match the material experiments.

The varying fibre orientation is a necessary requirement in order to calibrate for the characteristic length l, as it introduces bending strain in the deformation of the cube.

In order to calibrate the transverse isotropic case we are forced to combine the original data sets into the relevant three cases outlined in Figure 7.16. The combined data sets were constructed by fitting an exponential function to pairs of data using a MATLAB's built in curve fitting algorithm. The data sets were equally weighted using the least root mean square fit produced the resulting "midline" data set. The full data sets and the corresponding midline data sets are shown below in Figure 7.18.

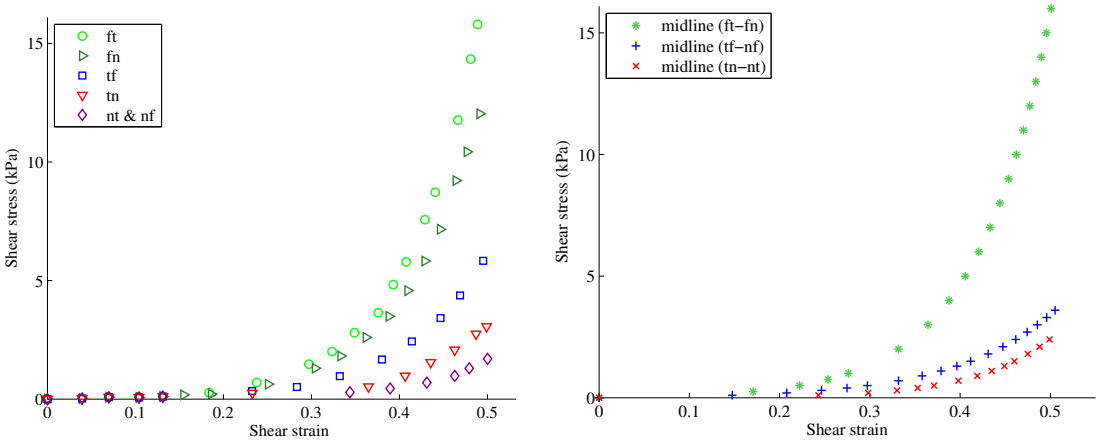

(a) (b)

FIGURE 7.18: (a) The original data sets on orthotropic myocardium, all six shearing modes present [30]. (b) Corresponding combined "midline" data sets needed for transverse isotropic material calibration.

The computational reproduction of the experiments are designed to reproduce the experimental design in [30] as accurately as possible. Using the same specified dimensions ($3mm \times 3mm \times 3mm$) each cube is fixed at the bottom with respect to all displacements, while the top surface experiences shear displacements amounting to 50% of the cube's length (also represented as 0.5 shear strain). The top and bottom surface were glued to plates, in the shearing device used by Dokos, and as such while shearing the top surface, the displacements in the remaining directions remain fixed. Additionally, we impose appropriate rotational boundary conditions on the top and bottom surface, resulting in all rotations being constrained along the top and bottom surface. The boundary conditions on the experiments are illustrated in Figure 7.19.

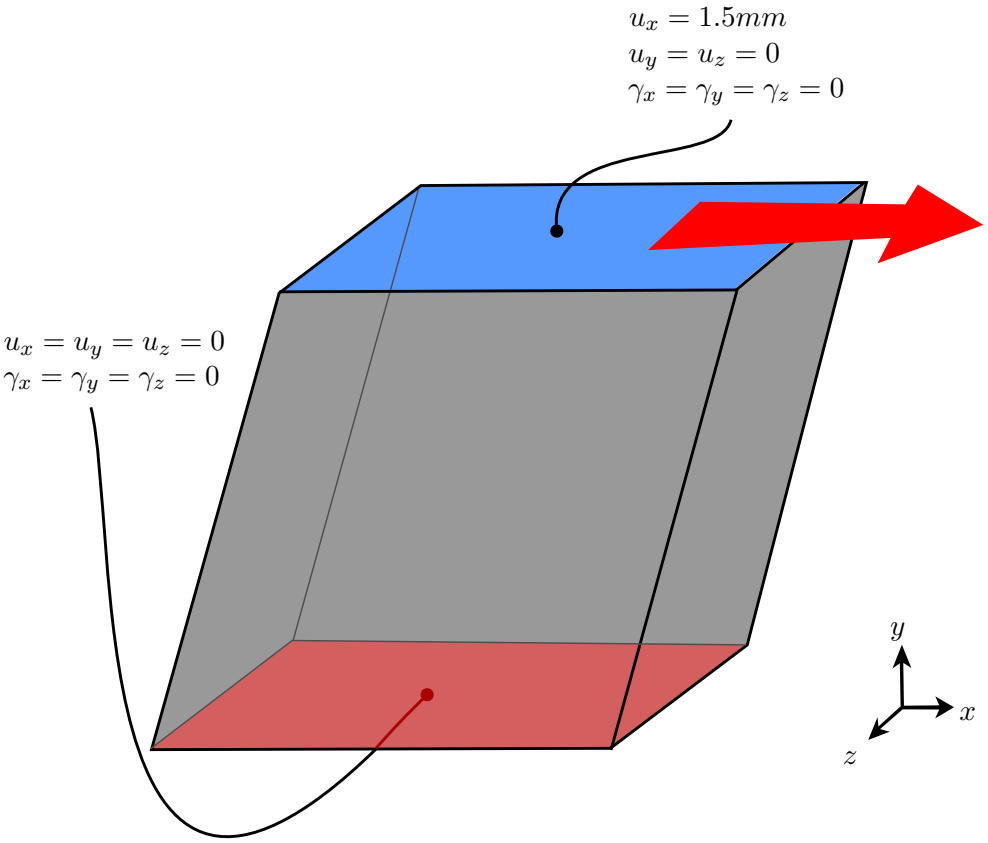

FIGURE 7.19: Illustration of the Boundary conditions replicating the Dokos shearing experiments. Mean fibre orientation differs with each of the three experiments, corresponding to the cases outlined in Figure 7.16

7.2.1 Optimization algorithm utilized in calibration

Research done in the Computational Continuum Mechanics Group, UCT, established an optimization scheme based on the Bounded Levenberg-Marquardt algorithm or BLVM [84]. For a detailed account of the optimization and corresponding implementation one is directed to [37].

Material parameter identification is found via minimization of a cost function, expressing the difference between experimental data points and corresponding simulation results. Initial material parameters choices need to specified, including constraints on the reasonable parameter choices.

Identification of material parameters involves minimization of this cost function below a specified tolerance. While the cost functions remains above this tolerance, new parameter choices are computed, via the use of a gradient based optimization algorithm. This process is illustrated in Figure 7.20.

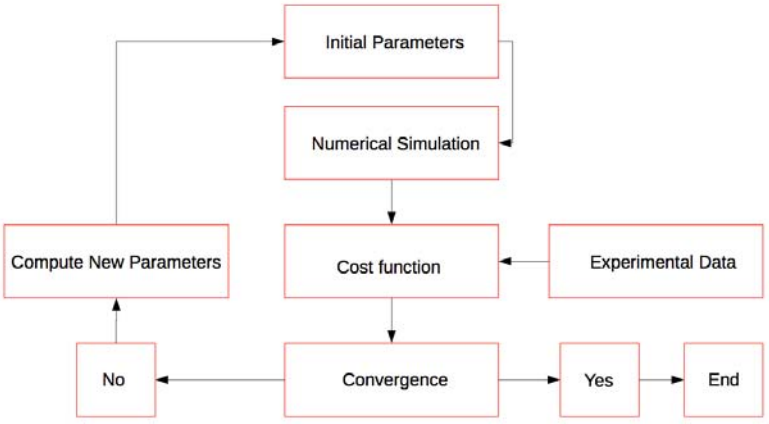

FIGURE 7.20: Schematic representation of updating procedure in the Levenberg Marquardt based optimization algorithm.

For the calibration of the nonlinear *Cosserat* fibre model, the optimization algorithm was applied separately to the three cases outlined in Figure 7.16. This forced the author to perform multiple rounds of calibration to identify suitable parameters. After the first iteration of calibration, any consistent results across the three experiments was taken as a successfully calibrated parameters and was fixed, or tightly constrained, for the successive rounds of calibration. All parameters were subject to calibration through the optimization routine, except for B and A_{comp} which were both set to 1.00. It would be redundant to calibrate for B in such a problem and simple shear is volume preserving and as such A_{comp} plays no role.

There may exist multiple pairs of material parameters and associated characteristic lengths, that fit the shear data experiments. Unfortunately without additional experimental data, a unique value for l cannot be determined with complete confidence. As no such suitable data exists, l is calibrated to achieve the lowest possible residual in the optimization routine.

7.2.2 Calibration results

The *Cosserat* fibre model is able to reproduce the experimental results for porcine myocardium relatively well. The resulting fitted model, plotted alongside the data sets used are shown in Figure 7.21. The fitted parameters are presented in the Table 7.5.

TABLE 7.5: Material properties for nonlinear *Cosserat* constitutive law, fitted to Dokos et al. [30] shear experimental data for porcine cardiac tissue.

Parameter	Symbol	Value
Principle fibre modulus	a_1	52.380
Shear fibre modulus	a_2	28.090
Principle matrix modulus	b_1	18.112
Shear matrix modulus	b_2	16.480
Characteristic length	l	0.6622
Stress Scaling 1	A	0.10
Stress Scaling 2	B	1.00
Incompressibility	A_{comp}	1.00

It should be noted that that simple fitting of exponential parameters for a Fung-type potential may lead to ill formulated stored energy problems, specifically with regards to convexity [61, 63]. The convexity of the of the stored energy potential, ensures positive definiteness of the tangent stiffness matrix in the element-free Galerkin implementation. This is an essential feature to ensure reliability of the computational results. It has been shown rigorously that a necessary and sufficient condition to ensure positive definiteness, is to enforce that Q is positive definite [40]. This can be achieved simply by enforcing the condition that the parameters A, B, a_1, a_2, b_1 and b_2 are strictly positive.

It was shown in Section 5.3 that for a given function Q, the stress scaling parameters A and B are unique and should be easily found through an optimization routine. Now that we have found the material anisotropy parameters (l, a_1, a_2, b_1 and b_2), we can employ the diastolic filling example as an optimization problem to calibrate the remaining scaling parameters against experimental data.

A critical point to draw attention to, is the inclusion of l as a material parameter. Unlike a classical formulation our model has now been calibrated with a feature of the micro structure implicit in the formulation. This feature places a higher dependency on the multi scale physics of the problem as opposed to phenomenological approaches. To elucidate the influence the calibrated characteristic length has, consider the analysis presented for the beam bending and torsion deformation, Figures 7.11 and 7.14. A characteristic length $l = 0.6622$, would change the midpoint deflection in the bending problem by roughly 8%, and change the deformed configuration in the torsional problem by almost 20%.

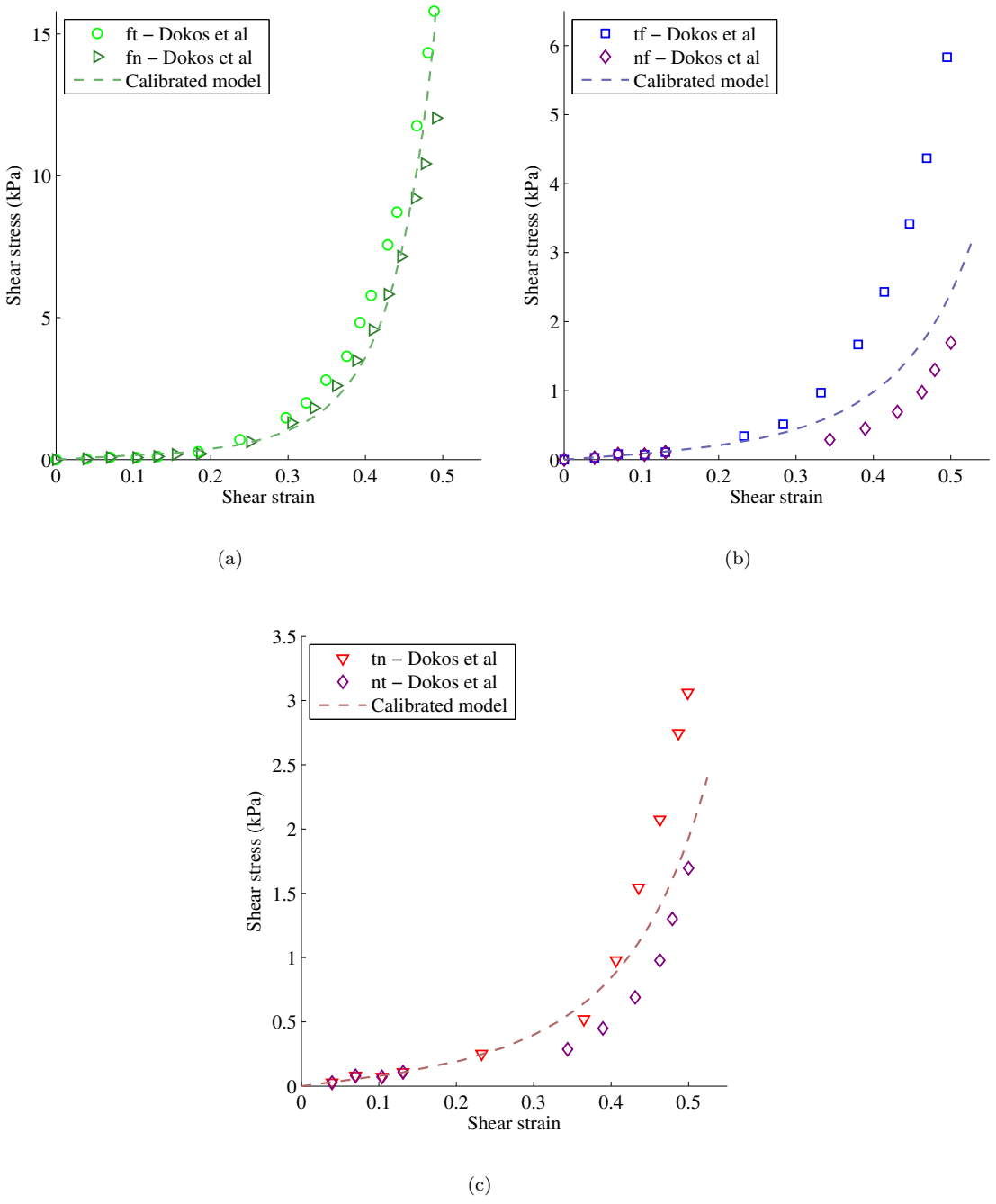

FIGURE 7.21: Material response of calibrated nonlinear *Cosserat* fibre model (dashed lines) alongside the combined data sets from Dokos et al. [30]. (a) The fibre plane shifted towards a transverse plane, (b) a transverse plane shifted towards the fibre direction and lastly, (c) a transverse plane shifted towards the other transverse plane.

Consider Figure 7.22, the calibrated *Cosserat* fibre model result for the shear experiment of a cube extending the plane normal to the fibre in the transverse direction is presented alongside the classical case (i.e $l = 0.0$). The classical case is less stiff, as one would expect. One could recalibrate the classical case to coincide more closely with the

experimental data, but in this sense one would be placing a larger dependence on local features, i.e that the stress at the material point is solely governed by first order strains.

The *Cosserat* fibre continuum theory, accounts for the influence of neighbouring material points through introducing higher order strains (i.e the change of curvature strains along a fibre) into the kinematics and constitutive laws of the problem. These contributions, scaled by l, provide a direct and meaningful way of including the micro structure and more accurately representing the material.

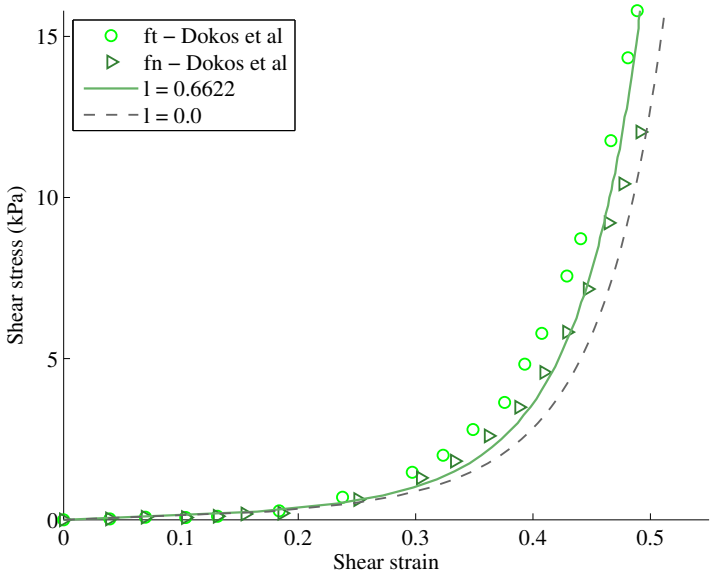

FIGURE 7.22: Material response of calibrated nonlinear *Cosserat* fibre model alongside the classical case for the same material parameters.

7.2.3 Passive filling in the rat left ventricle

As with the linear constitutive law, we utilize the pressure volume relationship in the diastolic left ventricle. A large number of studies quantify this relationship using various techniques in isolated, supported and in-vivo hearts for various species. The three rat studies of Herrmann et al. [55], Omens et al. [101] and Cingolani et al. [21] are used to validate and verify the computational model results. For comparison purposes, the ventricular volume has been transformed into a percentage volume change relative to the volume of the unloaded cavity, for which the cavity pressure is zero. Besides the change to the constitutive law, the problem description remains unchanged to the linear case, whereby the boundary conditions are outlined in Section 6.6 with the corresponding schematic in Figure 6.11.

Initial investigation revealed that the nonlinear constitutive model produced the qualitative pressure volume relationship one would expect. Prior calibration, mesh convergence analysis was performed to identify any mesh dependant influences in the computational model. The pressure volume relationship was explored for various mesh refinements ranging from the most coarse, 66 particles, to the most refine, 1565 particles. Each computational model was subjected to pressure loading that resulted in a final deformed configuration exceeding a 200% increase in cavity volume.

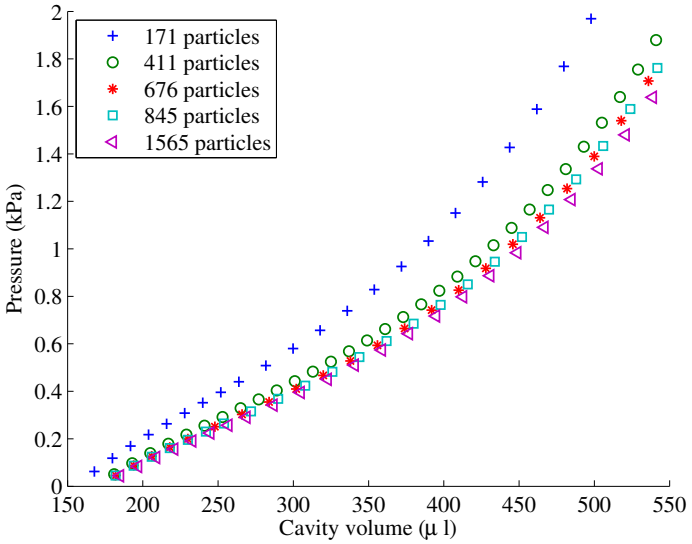

FIGURE 7.23: Convergence analysis using the pressure volume relationship the left ventricle cavity experiences during passive filling. Only key results are presented and cavity volume is presented without any transformations.

The core results of the convergence analysis are presented in Figure 7.23, showing the differences between solutions decreases dramatically when refining the meshes. Figure 7.24 shows sample meshes from the convergence analysis. It was found that the solutions were most effected by refinements in the radial direction (creating more layers between the endocardium and the epicardium).

A relatively fine mesh, corresponding to 676 particle was chosen for the purposes of calibration. As our convergence analysis shows, the mesh will provide reasonably close solutions to the converged solution, but also allow for more efficient computational analysis. This is an essential factor to consider when using the *Cosserat* fibre continuum approach as the system has to be solved for 3912 degrees of freedom, whereby the classical continuum would have almost half the computational requirements.

The model was subjected to loading up to $25mmHg$ $(3.5kPa)$ to match the loading conditions of the experimental data sets [21, 55, 101]. The characteristic length l as well as the four material anisotropy terms a_1, a_2, b_1 and b_2 were taken from previously

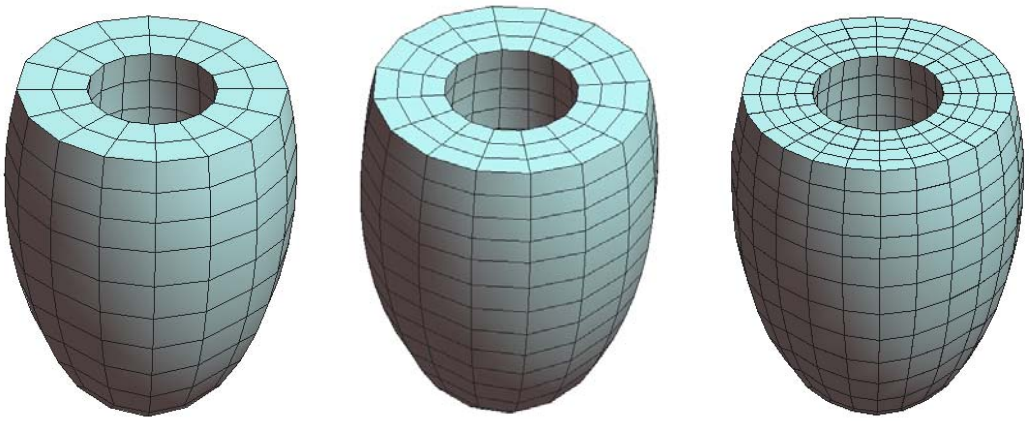

(a) 411 particles (b) 845 particles (c) 1565 particles

FIGURE 7.24: Three sample meshes used in the analysis of mesh dependency and convergence. The particle density is roughly twice as populated from mesh (a) to (b) and again through to (c).

calibrated shear experiments based on the experimental data of Dokos et al. [30]. The resulting stress scaling parameters A and B were calibrated using the pressure volume relationship. Taking into account the large variance of biological tissue results, we subject the calibration to the mean of the data sets.

TABLE 7.6: Material properties for nonlinear *Cosserat* constitutive law, calibrated using a levenberg marquad optimization algorithm with the shear experimental datasets of Dokos et al. [30] and the mean pressure volume relationship of the rat left ventricle from the datasets of Herrmann et al. [55], Omens et al. [101] and Cingolani et al. [21].

Parameter	Symbol	Value
Principle fibre modulus	a_1	52.380
Shear fibre modulus	a_2	28.090
Principle matrix modulus	b_1	18.112
Shear matrix modulus	b_2	16.480
Characteristic length	l	0.6622
Stress Scaling 1	A	0.45
Stress Scaling 2	B	0.15
Incompressibility	A_{comp}	0.50

The resulting calibrated model results are shown in Figure 7.25. Positions A-D have been marked on the figure and further analysis is presented at these points. The model was able to reproduce the experimental mean with great accuracy, resulting in a calibrated fit with $R^2 = 0.9955$. The full fitting and deviation metrics are presented in Table 7.7.

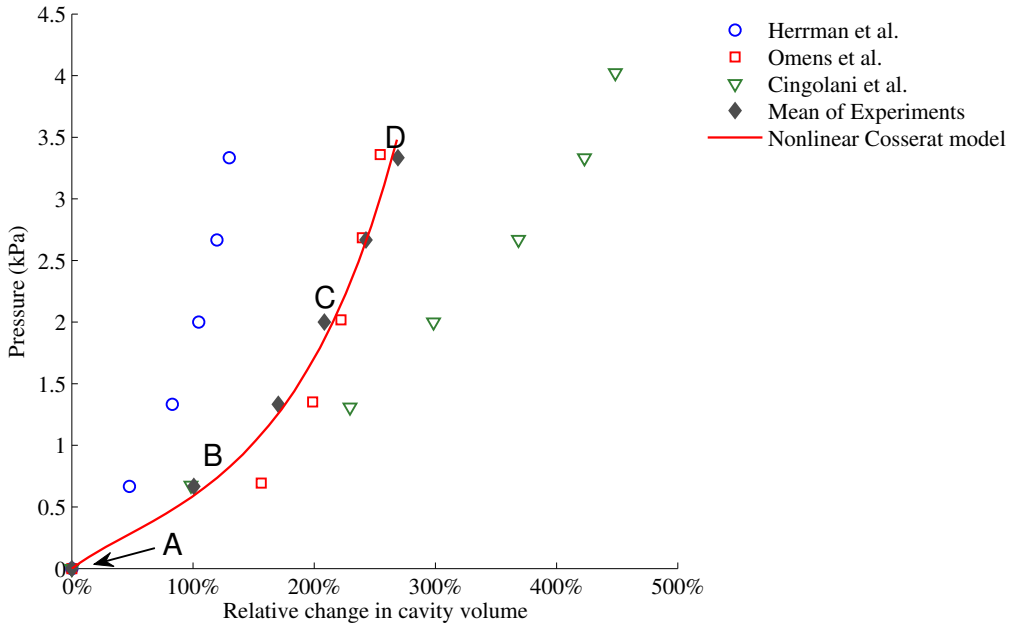

FIGURE 7.25: Passive material response of an ellipsoid model of the rat left ventricle. The *Cosserat* fibre model implemented with a nonlinear non-homogenised constitutive law was used and calibrated fit the mean experimental data results provided by Herrmann et al. [55], Omens et al. [101] and Cingolani et al. [21].

TABLE 7.7: Quantitative analysis of the calibrated nonlinear *Cosserat* fibre model provides satisfactory fitting measures to the mean data values of [55], [101] and [21].

Measure	**SSE**	**R-Squared**	**RMSE**
Correlation to mean experimental data	0.0227	0.9955	0.0616

The final calibrated material parameters for the rat left ventricle are presented in Table 7.6. The corresponding material parameters for the invariant based approach, utilized in the computational experiments is easily identified through comparison. There is limited experimental data available for mechanical analysis of the rat left ventricle, however sufficient computational studies exist, to which we can compare our results. Humphrey and Yin [64] performed detailed stress and strain analysis on passive left ventricular function. The study showed that peak strains are experienced at the endocardium wall. This was also independently shown by Guccione et al. [50], and compared reasonably well with experimental data. Additionally, the study showed that the peak stresses occurred between the endocardium wall and the midwall. Costa et al. [26] details the peak stress of cardiac tissue to be at 40% of the wall depth from the endocardium, albeit the analysis was for scarred tissue.

In the subsequent mechanical analysis, it becomes useful to utilize the effective stress and effective strain measures given by

$$\sigma_{eff} = (1.5\boldsymbol{\sigma} : \boldsymbol{\sigma})^{\frac{1}{2}} \qquad \text{and} \qquad E_{eff} = (1.5\boldsymbol{E} : \boldsymbol{E})^{\frac{1}{2}}. \tag{7.1}$$

Both our strain and stress results, produce qualitatively agreeable results. While the entire left ventricle dilates and mildly twists, the endocaridum experiences the most pronounced strain.

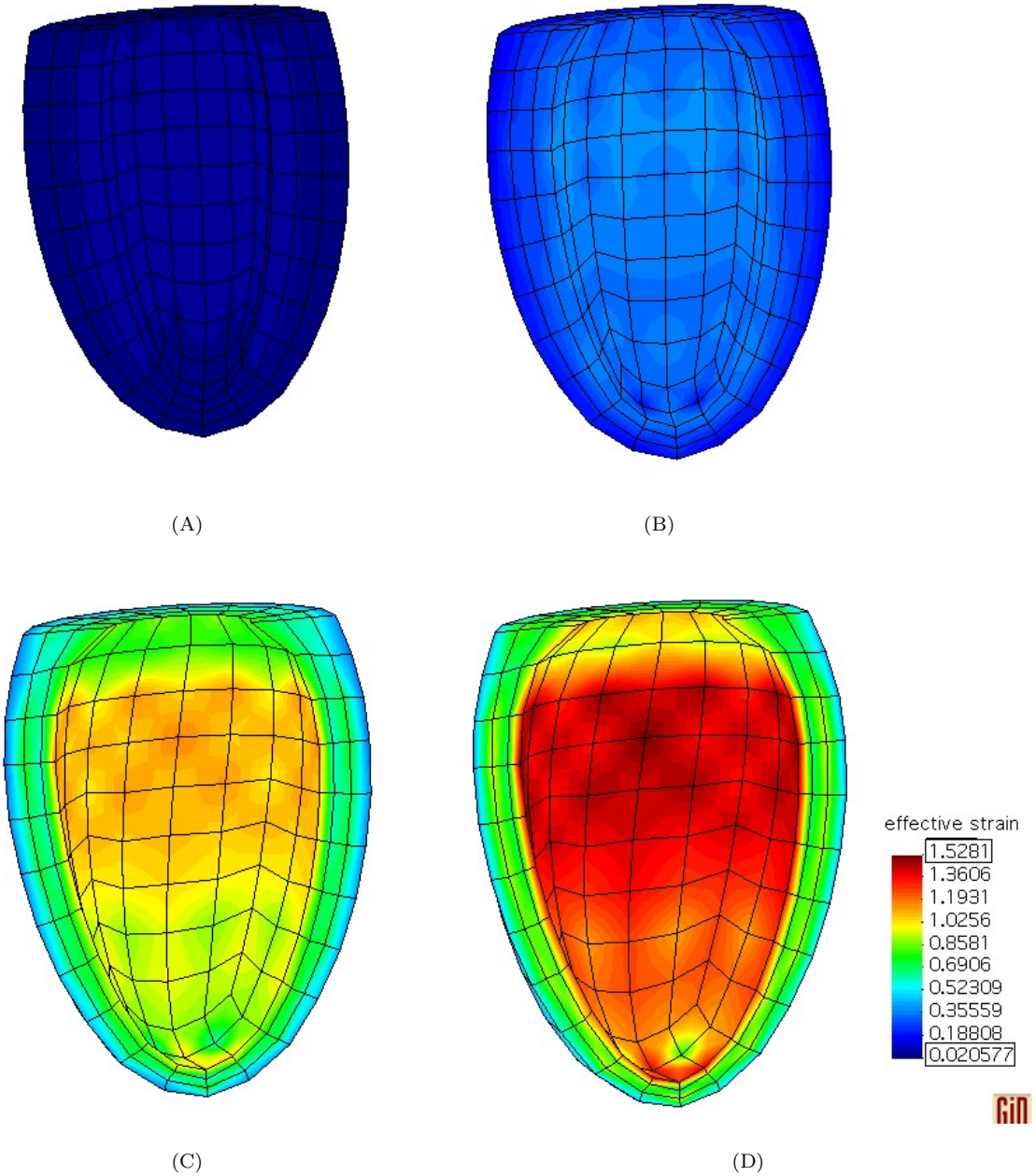

FIGURE 7.26: Effective strain plotted on the deformed configuration of the computational model of the rat left ventricle undergoing diastolic filling at various stages (A-D) corresponding to positions labelled in Figure 7.25.

High strain regions are localized to the upper midwall of the endocardium and are clearly illustrated in Figure 7.26. Midwall peak stress is also a defining feature of our computational model. This result is consistent throughout the longitudinal profile of the geometry (ie. from base to apex).

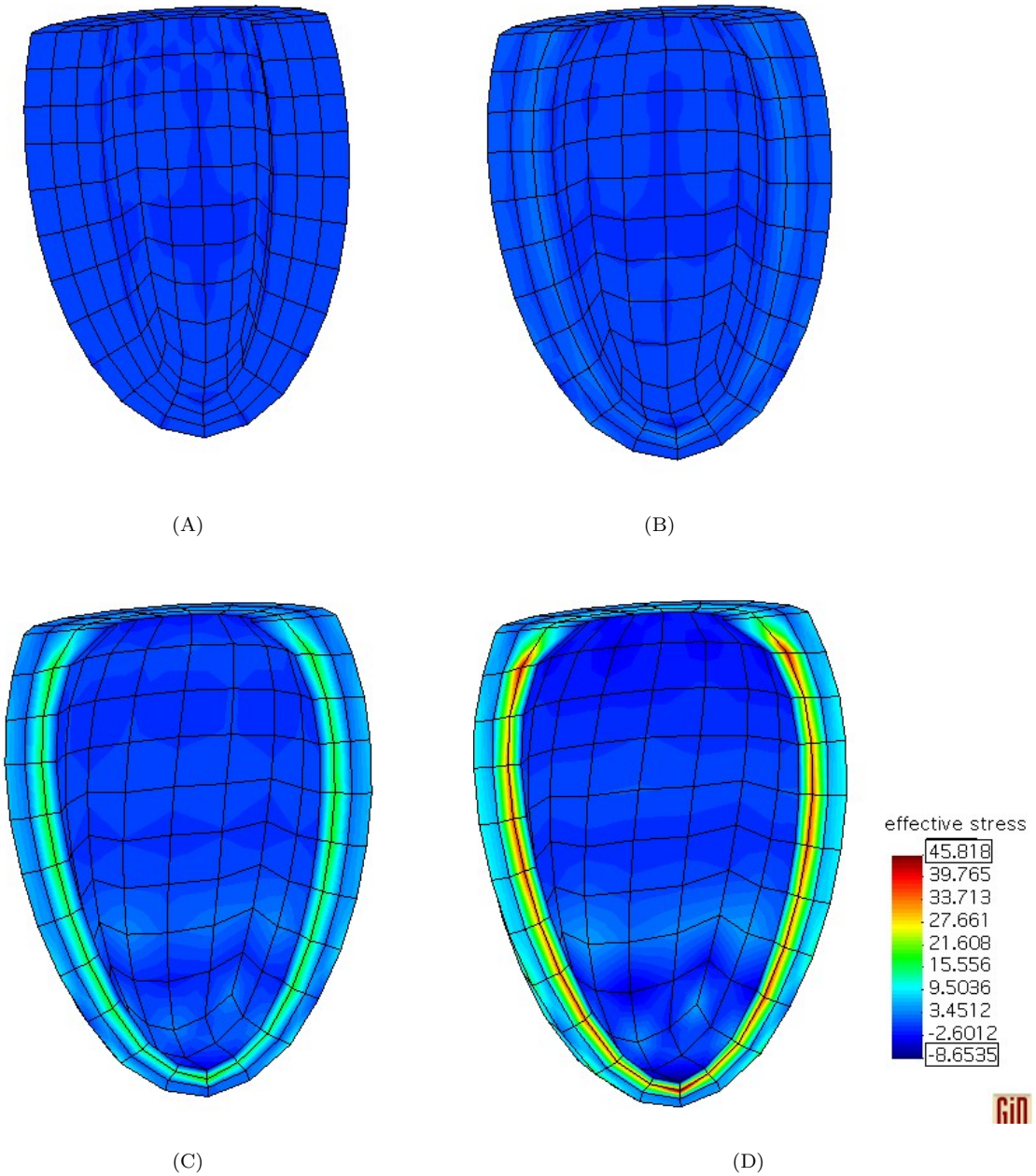

FIGURE 7.27: Effective stress (kPa) plotted on the deformed configuration of the computational model of the rat left ventricle undergoing diastolic filling at various stages (A-D) corresponding to positions labelled in Figure 7.25.

The peak stress at the midwall is a result of fibre orientation and contributions from circumferential strain. Strains in fibre direction are the single largest contributor to the

overall stress and at the midwall, the fibre orientation coincides with the circumferential direction, resulting in significant circumferential stress.

In Figure 7.28, the effective couple stress is plotted over half the domain of the left ventricle at positions (A-D) from Figure 7.25. Here we see the couple stress contributions to be significantly lower than the force stress contributions.

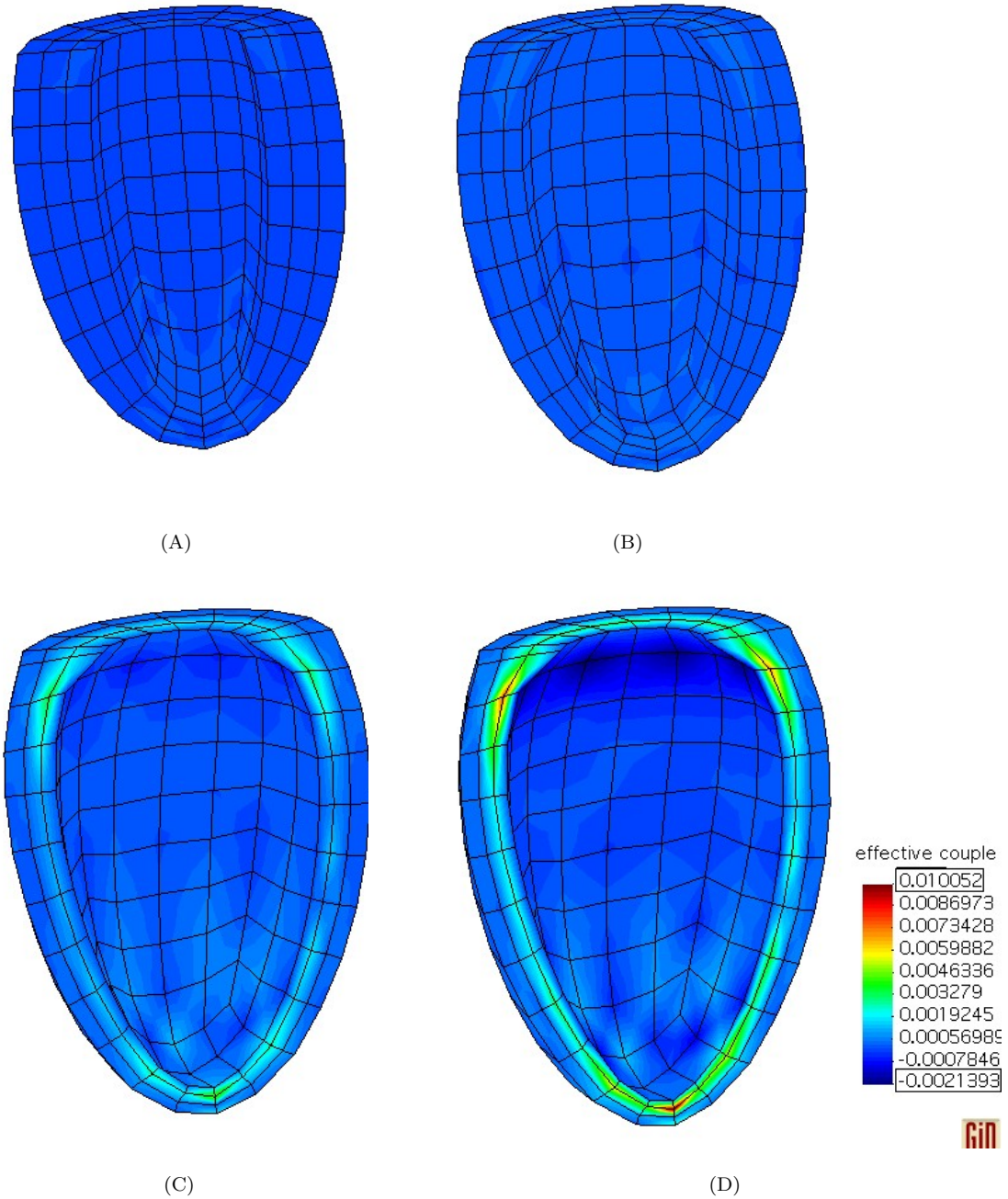

FIGURE 7.28: Effective couple stress plotted on the deformed configuration of the computational model of the rat left ventricle undergoing diastolic filling. Material parameters correspond to Table 7.6 and the plots are given at various stages (A-D) corresponding to positions labelled in Figure 7.25.

7.2.4 Passive filling in the canine left ventricle

Sometimes it is more desirable to utilize the canine left ventricle in cardiac modelling. Using the larger geometry provides a study that can be related better to the human left ventricle. Additionally, in some areas of cardiovascular research, like active tension models, the body of literature and available studies are better developed for the canine geometry and structure. Research done in the Computational Continuum Mechanics Group, UCT, has resulted in a calibrated nonlinear hyperelastic, transversely isotropic Cauchy model based on the canine cardiac cycle [37]. This model, which is verified against the results of Kerckhoffs [72], follows the formulation proposed in Eq. (6.15) and will be used to compare the results from the *Cosserat* fibre model. The material parameters for the strain energy function are given in Table 7.8.

The *Cosserat* material parameters were calibrated to give the closest fit to the experimental data from Kerckhoffs [72]. Keeping a consistent approach to previous analysis, the volume data is presented in percentage volume change from the unloaded state. The resulting pressure volume curve for passive filling is presented in Figure 7.29 and the corresponding material parameters are presented in Table 7.9. A mesh corresponding to 363 particles was utilized, in order to be consistent with the calibrated Cauchy results [37].

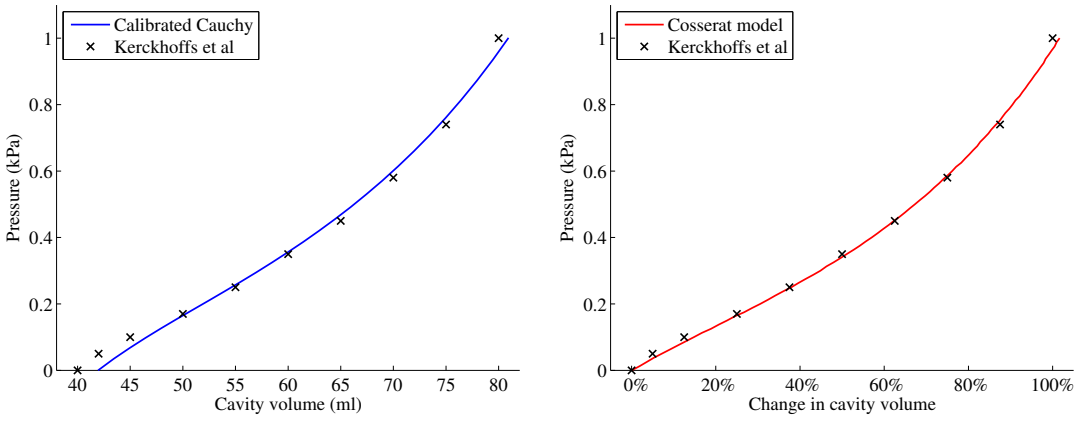

(a) (b)

FIGURE 7.29: (a) *Cosserat* fibre model results for the passive filling of the canine left ventricle. (b) Simulated results from a calibrated Cauchy model. Both models are plotted alongside the original data points to which the model was calibrated [72].

While both models have the same initial volume of $41.9ml$, the end diastolic volumes of the two models are slightly different due to the different approaches in representing the cavity volume data. The *Cosserat* fibre model has an end diastolic volume of $84.5ml$ compared with the $80.9ml$ end diastolic volume for the Cauchy model. McCulloch et al.

[89] gives the standard deviation of volume at the given pressure as 5% for a single experiment, while the differences between multiple studies on the canine left ventricle can have a much larger differences [94]. The difference between the *Cosserat* fibre and Cauchy models, approximately 4%, is within the range of standard deviation and close enough to serve as a comparison.

TABLE 7.8: Material parameters for the Cauchy model.

Parameter	Value
A (kPa)	0.292
A_{comp} (kPa)	100.3
b_{ff}	5.79
b_{tt}	6.89
b_{nn}	3.74
b_{fs}	12
b_{fn}	6.67
b_{sn}	6.67

TABLE 7.9: Material parameters for the *Cosserat* model.

Parameter	Value
A (kPa)	0.20
B	0.335
A_{comp}(kPa)	0.5
a_1	52.380
a_2	28.090
b_1	18.112
b_2	16.480
l (mm)	0.6622

Using the calibrated material parameters presented in Table 7.9, mesh convergence analysis was performed to identify any mesh dependant influences in the computational model. The pressure volume relationship was explored for various mesh refinements ranging from the most coarse, 66 particles, to the most refine 1299 particles. Each computational model was subjected to pressure loading up until 2.0 kPa. The full results of the convergence analysis are presented in Figure 7.30, showing the differences between solutions decreases dramatically with mesh refinement.

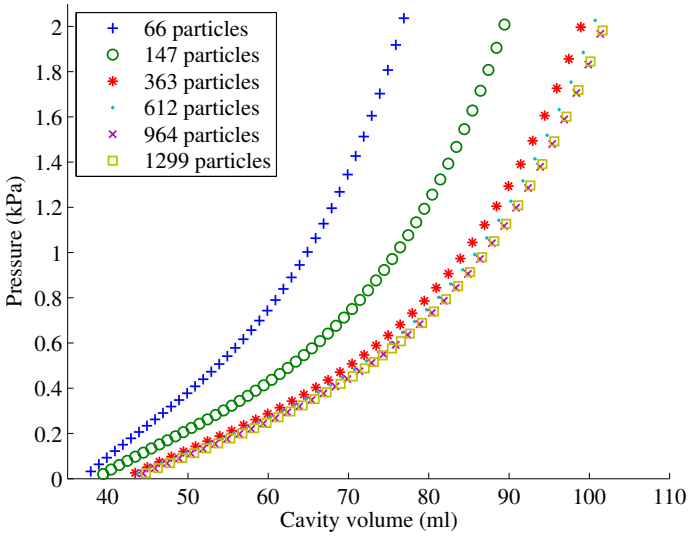

FIGURE 7.30: Convergence analysis using the pressure volume relationship the canine left ventricle cavity experiences during passive filling.

To model diseased states of the left ventricle during passive filling, we introduce a model geometry with an infarction. Mathematically, this will be a portion of the geometry that inherits different material parameters, depending on the diseased state we wish to model. The boundary conditions of the problem remain unchanged. Two diseased cases will be explored for the passive filling stage:

1. Acute ischemia. The initial hours immediately following an acute myocardial infarction. In this period, the infarct area becomes less stiff. The infarct area experiences larger strains, and the pressure volume curve of the left ventricle shifts to the right (corresponding to a more compliant cavity) [11, 56].

2. Fibrotic Stage. This stage is characterized by dramatic increase of collagen in the infarct region resulting in stiff infarct region. The diastolic filling capacity is consequently reduced [56].

To simulate this, we employ the approach of [75] and appropriately modify the stress scaling material parameter A in order to represent the regional stiffness changes of the infarct. For acute ischemia, $A_{infarct} = 0.5A_{healthy}$ and for the fibrotic stage $A_{infarct} = 2A_{healthy}$. Additionally in the fibrotic stage, the infarct region has lost significant myocte cells due to ischemia. As a result, we lower the characteristic length l as a means to represent this significant loss of fibre bundles in the area. A relatively fine mesh corresponding to 964 particles, was selected to better define the infarct region.

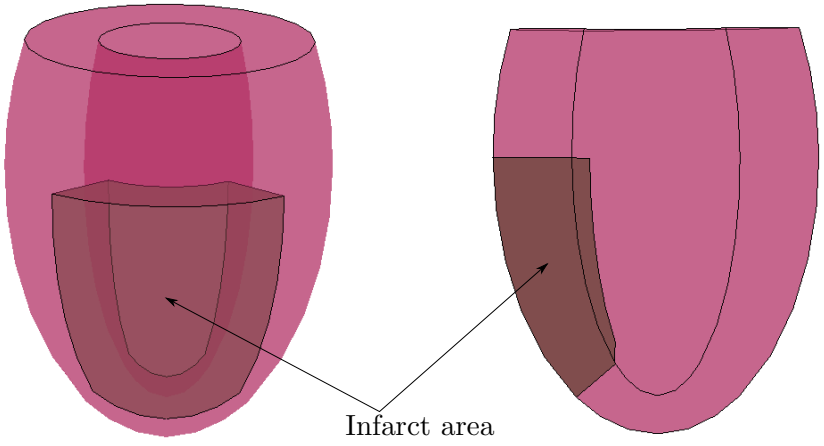

FIGURE 7.31: Schematic of the canine left ventricle with an infarction situated on the cavity wall. The infarct fraction is 14.14% of total cavity mass.

The first result we find is that the cavity's ability to reach a healthy end diastolic volume is compromised by the infarct. In the acute ischemic case, the cavity volume increases

and in the fibrotic case the cavity volume shrinks. This result is in good accordance with literature findings [11, 53, 56].

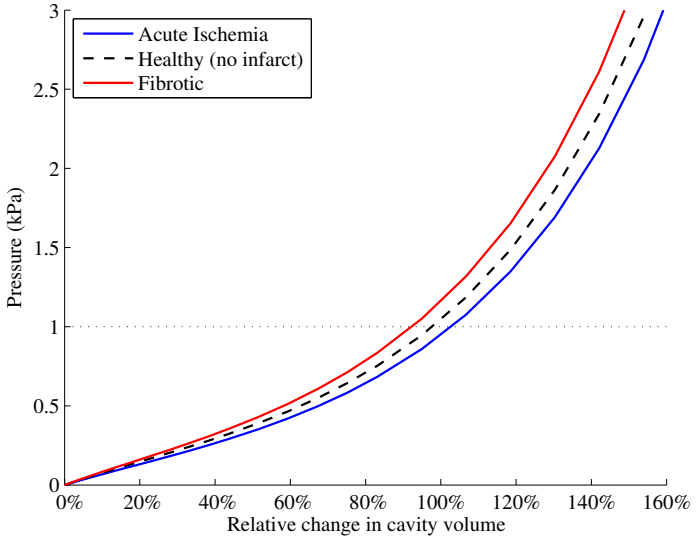

FIGURE 7.32: Pressure volume results during passive filling of the diseased canine left ventricle. Compliance of the left ventricle due to infarct stiffness is relevant at all stages of passive filling.

It should be noted that the changes to cavity volume are noticeable throughout the passive filling stage, made clear by Figure 7.32. The infarct increasingly affects the compliance of the left ventricle throughout the loading.

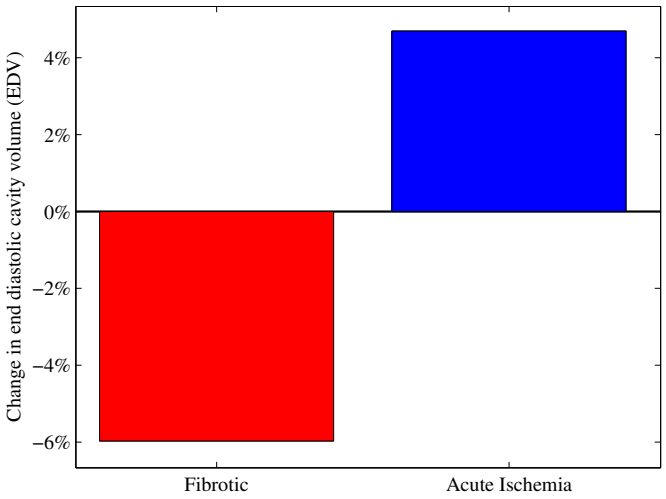

FIGURE 7.33: Percentage changes in end diastolic volume, relative to the healthy case. End diastolic pressure was taken to be $1kPa$.

Figure 7.33 shows that for an infarct of moderate size (14% of myocardium volume), the changes to end diastolic volume are relatively marginal. The fibrotic case reduces the cavity volume by 5.97% and the acute ischemic case increases cavity volume by 4.69%. This however is not completely indicative of cardiac dysfunction. A strain analysis would be the best indication to show the extent the infarct and the surrounding tissue is being compromised, i.e one could identify deformation and strains that could impair cardiac function.

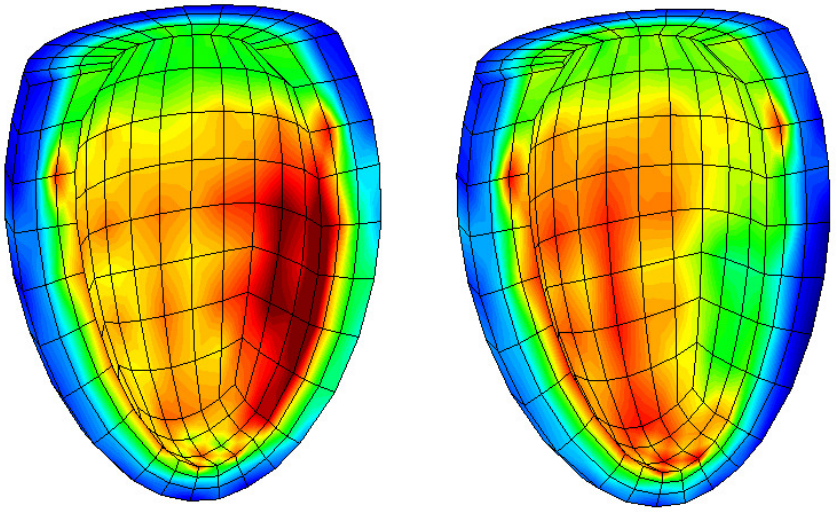

(a) Acute Ischemia

(b) Fibrotic

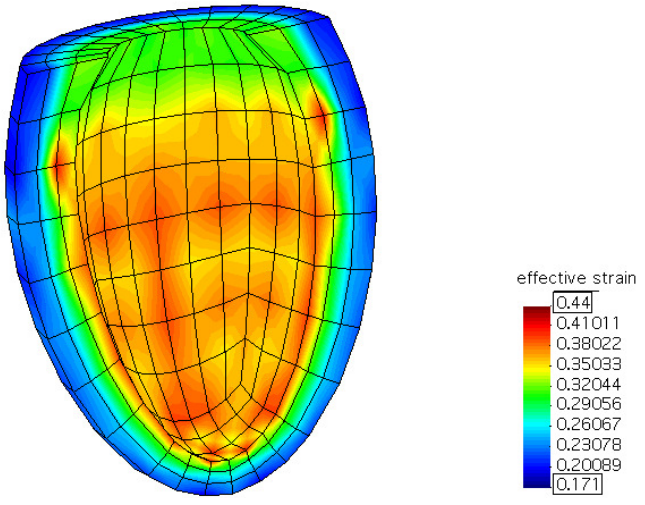

(c) Healthy

FIGURE 7.34: Strain contour plots over half of the left ventricle for the diseased and healthy cases, at end diastolic pressure ($1kPa$). The division of the left ventricle was chosen to bisect the infarct and reveal the transmural strain profile through the infarct.

In Figure 7.34 the strain profile is shown for the acute ischemic, fibrotic and the healthy case. The diseased cases reveal large strain gradients between the infarct and healthy tissue. The most dramatic changes appear on the endocardium surface. In both diseased cases, the surrounding tissue compensates for the infarcted region, increasing the strain gradients between healthy and diseased tissue. In the case of acute ischemia, the infarct region experiences mild bulging and significant strains. This corresponds with the physiologically response of the acute ischemic left ventricle, found in literature. The higher strains, and bulging of the infarct, place the region at the risk of permanent structural changes and even the risk of rupture. This corresponds well with literature findings. Batts et al. [8] found that 80% of all left ventricle free wall ruptures occur in the first week.

7.2.5 Systole in the canine left ventricle

As detailed in Section 6.3, systole is the portion of the cardiac cycle whereby the ventricle contracts and subsequently performs ejection. This phase of the cardiac cycle introduces active tension into the model, which in turn, introduces a transient component into the computational modelling. The systolic phase of cardiac function introduces a more complex deformation in the left ventricle than the passive filling stage [104, 110], especially with regard to torsion [108, 116]. The complex development of stress, strain and the accompanying deformed configurations of the left ventricle in systole, present experiments that would quantify the influence of the *Cosserat* fibre model in a more meaningful manner. Additionally, in order to evaluate basic cardiac function, one would need to be able to reproduce experiments that include systolic function.

The active tension model introduced in Section 6.5 is utilized for modelling systole. The material parameters for the active tension model were chosen in accordance with those presented in Guccione et al. [49]. Modifications were necessary as the Guccione parameters were modelled using a cylindrical representation of the left ventricle, and our model is an ellipsoid which offers a more realistic geometry (and is far more common in studies over the last 15 years).

The parameters are presented in Table 7.10 alongside the original material parameters of Guccione et al. [49] and those used in the Cauchy model.

TABLE 7.10: Active Material parameters for the *Cosserat* fibre model, presented alongside the Cauchy material parameters and the original material parameters from Guccione et al. [49].

Parameter	Cauchy model	Guccione model	*Cosserat* model
Ca_0 (μM)	4.35	4.35	4.35
$(Ca_0)_{\max}$ (μM)	4.35	4.35	4.35
l_0 (μm)	1.58	1.58	1.58
l_{s_0} (μm)	$1.78 - 1.91$	2.04	2.06
t_0 (ms)	100	100	100
m ($\mathrm{s} \cdot \mu\mathrm{m}^{-1}$)	1.0489	1.0489	1.0489
B ($\mu\mathrm{m}^{-1}$)	2.48	4.75	2.48
$T_{\max}$ (kPa)	136.9	135.7	170.0

The first four parameters presented in Table 7.10, represent physically measurable quantities with meaningful connections to quantities found in cardiac tissue (i.e the calcium concentration and sarcomere length quantities), and as such, care was taken not to deviate or change these parameters too much from the original work of Guccione et al. [49]. Equal care was given to the transient terms that govern when active tension occurs, t_0 and the period of deactivation m. $T_{\max}$ is a scaling parameter over the entire active tension function, Eq. (6.20), that coincides with the maximum allowable active tension, and B is a scaling parameter that acts on the exponential component of the active tension function, Eq. (6.24). As such B and $T_{\max}$ were chosen as the most suitable parameters to adjust in order to achieve a qualitatively reasonable active tension development for the model. Additional care must be taken for the choices of l_{s_0}, that is, the sarcomere length in the unloaded case. Literature values place the unloaded sarcomere length in the canine heart between the range of $2.0 - 2.28\mu m$ [80, 137]. However Guccione et al. [49] uses a constant sarcomere length l_{s_0} of $2.04\mu m$.

A three element Winkessel model, see Eq. (6.31), was utilized for the purposes of controlling the ejection portion of the systole. The same material parameters from the calibrated Cauchy model, were found suitable for the *Cosserat* fibre model, with the exception of R_0, the flow resistance, which controls the initial slope of ejection. These calibrated Cauchy Windkessel parameters and corresponding *Cosserat* fibre Windkessel parameters are presented in Table 7.11.

The Windkessel material parameters of the calibrated Cauchy model were derived from computational experiments using a mesh with refinement corresponding to 363 particles. The convergence results of pressure volume relationship in Figure 7.30, show that a 363 particle mesh is reasonably close to the converged solution. Furthermore, the computational requirements of a generalized model result in substantial computational time.

TABLE 7.11: Three element Windkessel parameters for the *Cosserat* fibre and the Cauchy model.

Parameter	Cauchy model	*Cosserat* fibre model
C $(\frac{\text{mm}^3}{\text{kPa}})$	4476.2	4476.2
R $(\frac{\text{kPa·s}}{\text{mm}^3})$	8.13×10^{-5}	8.13×10^{-5}
R_0 $(\frac{\text{kPa·s}}{\text{mm}^3})$	6.43×10^{-6}	5.43×10^{-6}

These factors motivate the selection of a 363 particle mesh for further experiments. Further refinement would demand significantly larger computational time (i.e weeks), while

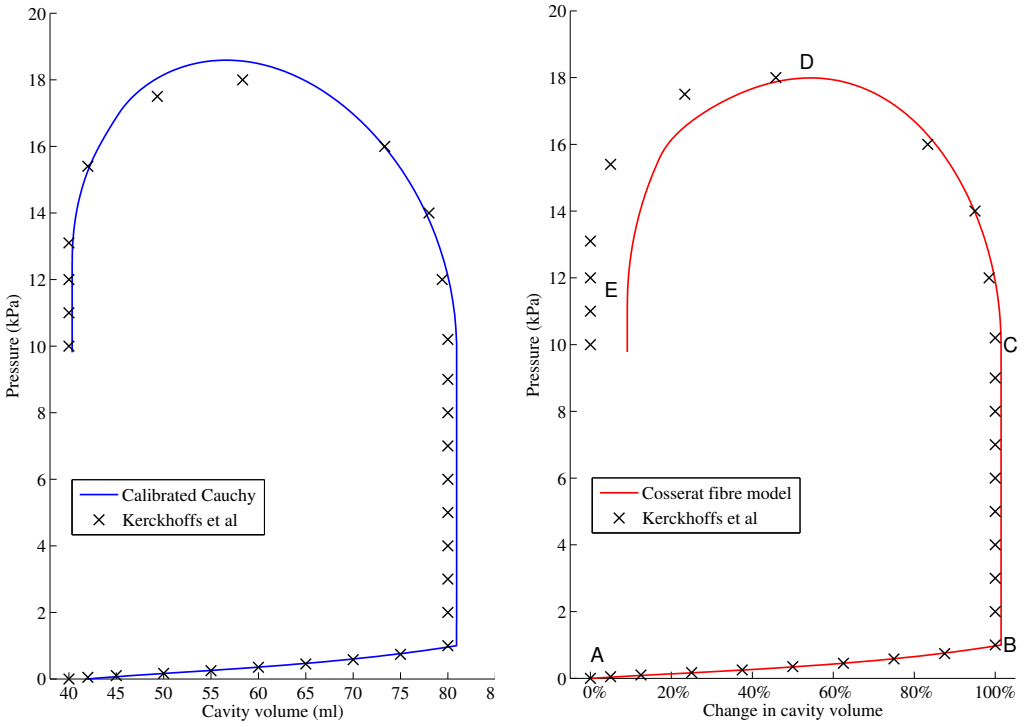

(a) (b)

FIGURE 7.35: The pressure volume loop for the canine left ventricle presented from passive filling from the unloaded configuration to end ejection shown for (a) Simulated results from a calibrated Cauchy model, and (b) Simulated results *Cosserat* fibre model. Both models are plotted alongside the original data points to which the model was calibrated [72].

The global pressure volume relation is presented in Figure 7.35. While the *Cosserat* fibre model does not match the computational results of Kerckhoffs [72] as closely as the calibrated Cauchy model for the end of ejection, it does provide clinical measures, both qualitatively and quantitatively, that are in line with literature values and acceptable in terms of healthy cardiac function. These clinical measures are subsequently discussed in detail.

The first stage of systole, isovolumetric contraction (IVC) is characterized by constant cavity volume while the ventricle undergoes rapid contraction. This results in an increasing cavity pressure and a torsional response in the ventricle geometry [16, 110]. Additionally this stage is associated with a shortening of the minor axis [16, 109], resulting in a more "cylindrical" geometry from the end diastolic configuration. These clinically measured features are captured significantly well by our computational model: in Figure 7.35 the qualitative pressure volume relation is preserved and well illustrated, in Figures 7.36(b)-(c) the narrowing along minor axes (x direction and y direction) and the torsional response in the computational model is clearly illustrated. This rapid increase in torsional deformation, is a result of the local anisotropic description of the material, the global fibre orientation description and the initiation of active tension acting along the fibre orientation throughout the left ventricle. The torsional deformation continues throughout the ejection period, specifically with increases to the endocardium surface, as the ventricle cavity decreases. This can be seen by comparing the scaled vector arrows and grid lines on the inner surfaces of Figures 7.36(c)-(e) which correspond to the endocardium. By the end of ejection there is a slight decrease in twisting on the epicardium, which will be addressed subsequently.

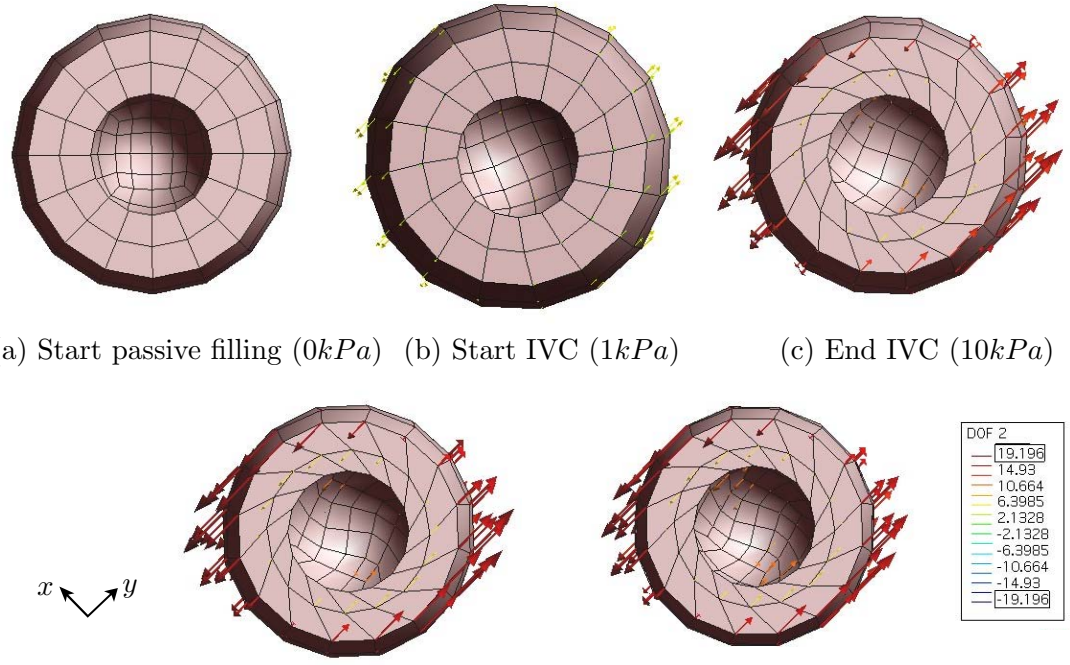

(a) Start passive filling ($0kPa$) (b) Start IVC ($1kPa$) (c) End IVC ($10kPa$)

(d) Mid ejection ($18kPa$) (e) End ejection ($12kPa$)

FIGURE 7.36: Deformed configurations corresponding to positions labelled A - E in Figure 7.35, viewed along the major axis (i.e z direction). Displacements in the y direction, represented by scaled arrows are plotted throughout the canine left ventricle.

This global counter clockwise twisting of the left ventricle through out the IVC and ejection phase is in line with MRI findings [17, 130] and other computational models

[5, 141]. A more detailed analysis, however would not provide significant insight as a single ventricle model, as used for this study, is incompatible with clinically measured metrics of torsion such as Russel [116]. The right ventricle mass and the structural stiffness it provides is unaccounted for in our model.

In Figure 7.37 the effective stress is plotted on the deformed configuration for positions labelled A - E in Figure 7.35. Consistent with the earlier results in the passive rat left ventricle, the spacial distribution of stress is consistently highest at the midwall. This result is consistent throughout the longitudinal profile of the geometry. The peak stress of the model is experienced mid ejection, and coincides with the peak active tension. The stress state at the end of ejection is dramatically reduced, due to the reduced active tension. As the active tension in the model continues to decrease, the stresses that result from the incompressibility penalty term begin to have a more predominant role. As a result the left ventricle begins to untwist on the epicardium surface.

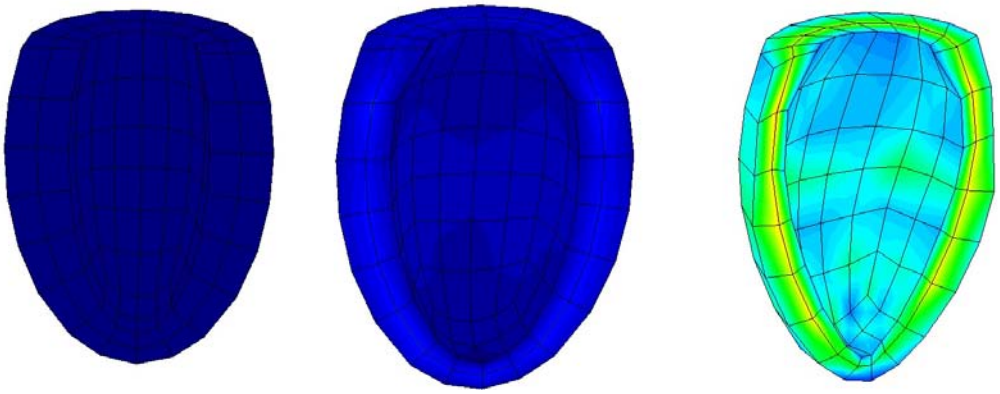

(a) Start passive filling (b) Start IVC (c) End IVC

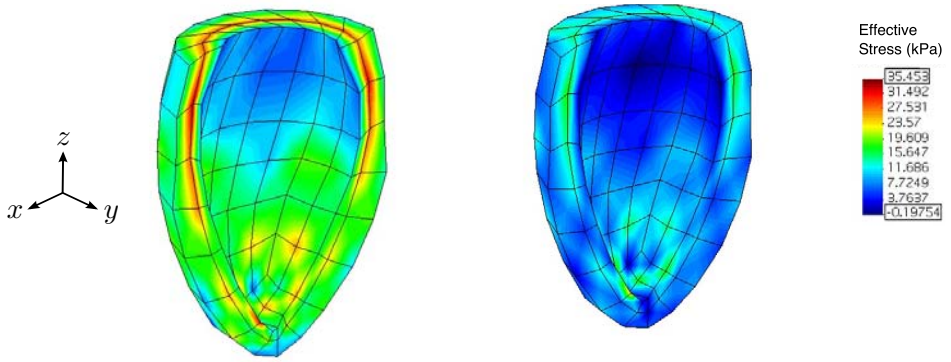

(d) Mid ejection (e) End ejection

FIGURE 7.37: Effective stress for the *Cosserat* fibre model plotted on half of the domain of the canine left ventricle during the cardiac cycle. Deformed configurations corresponding to positions labelled A - E in Figure 7.35.

The active tension development provides the largest contribution to the overall stress

of the left ventricle during systole. In Figure 7.38 the active tension is plotted on the deformed configuration for the various stages throughout the cardiac cycle. The developed active tension model is directly related to the timing of the cardiac cycle and the sarcomere length, which in turn is a function of the strains of the left ventricle.

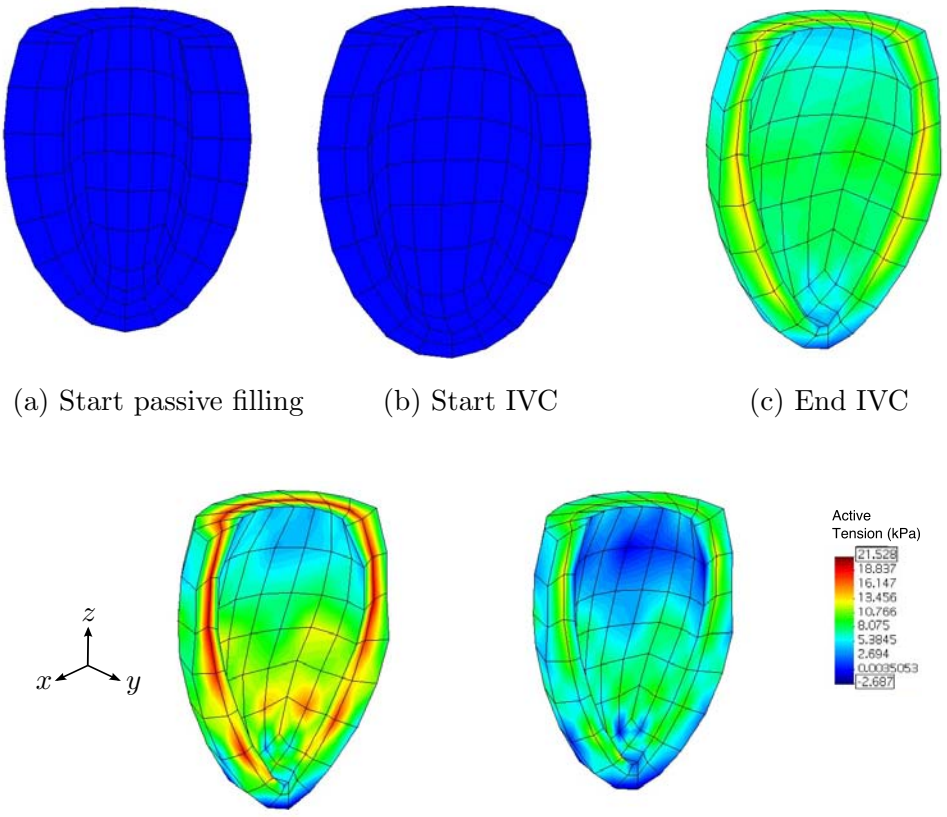

(a) Start passive filling (b) Start IVC (c) End IVC

(d) Mid ejection (e) End ejection

FIGURE 7.38: Active tension for the *Cosserat* fibre model plotted on half of the domain of the canine left ventricle during the cardiac cycle. Deformed configurations corresponding to positions labelled A - E in Figure 7.35.

In Figure 7.39, a more detailed analysis of the active tension and corresponding sarcomere lengths are presented alongside each other. Positions along the base, equator and lower region are presented to elucidate the development of active tension in the *Cosserat* fibre model. Important measurements with respect to the timing of the cardiac cycle are summarised in Table 7.12.

TABLE 7.12: Timing of the active tension model during the systolic phase of the canine left ventricle.

Position in cardiac cycle	Time (ms)
End passive filling / Start IVC	81
End IVC / Start ejection	106
Mid ejection	133
End ejection	308

Sarcomere lengths in Figure 7.39, reach a peak at the end of diastole, at the start of isovolumetric contraction they experience a steady and decline in length. This decline continues into ejection until peak active tension is reached, after which the sarcomere lengths seem to stabilise. Near the end of ejection, and into the early stage of isovolumetric relaxation, the sarcomere lengths start to increase in length. The range of sarcomeres at the end of diastole is between $2.15\mu m - 2.4\mu m$, this is within close proximity with literature values, which present a range of sarcomere lengths for the canine between $2.17\mu m - 2.23\mu m$ [48, 117] and computational results which have an even larger range

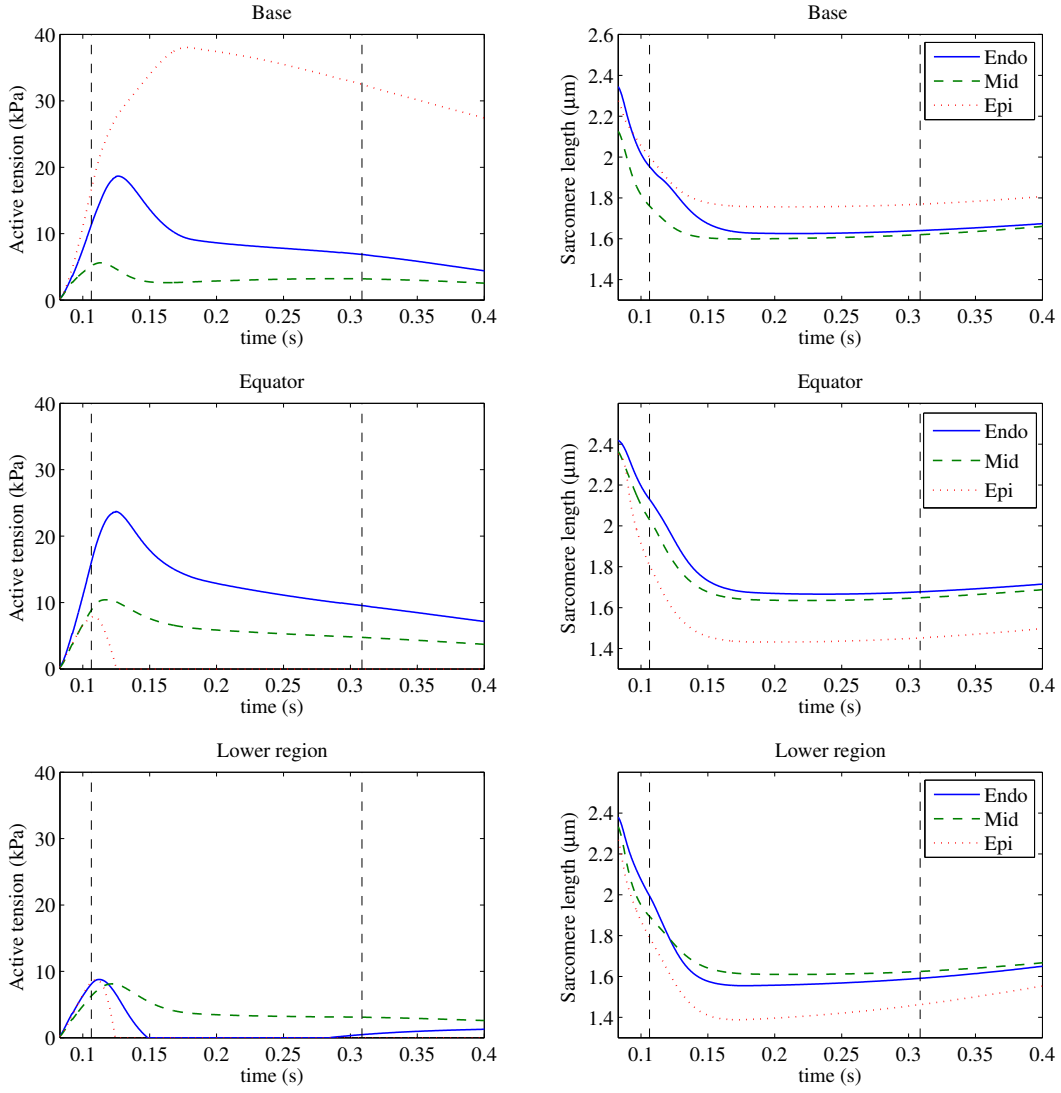

FIGURE 7.39: The active tension development over time for 9 particles located on the free wall of the left ventricle plotted alongside the corresponding sarcomere lengths. The results are presented in three rows, corresponding to positions along the base, equator and lower region (roughly halfway between the equator and the apex). Each figure presents results for particle positions at the endocardium (—), midwall (– –) and epicardium (···). The time line starts at the beginning of isovolumetric contraction, ($t = 0.081s$), the first black vertical dashed line corresponds to the start of ejection and the second black vertical dashed line corresponds to the end of ejection.

Beyar and Sideman [9] has shown that sarcomere lengths on the endocardium shorten more dramatically in systole than those on the epicardium, which occurs on our computational model, except for sarcomeres along the base. This is most likely due to the influence of the basal boundary conditions. The overall shape of the active tension curve, the dependency on the sarcomere length, and the relative deformation of the sarcomeres correspond qualitatively with results found clinically or in other computational studies, as shown in Figure 7.40.

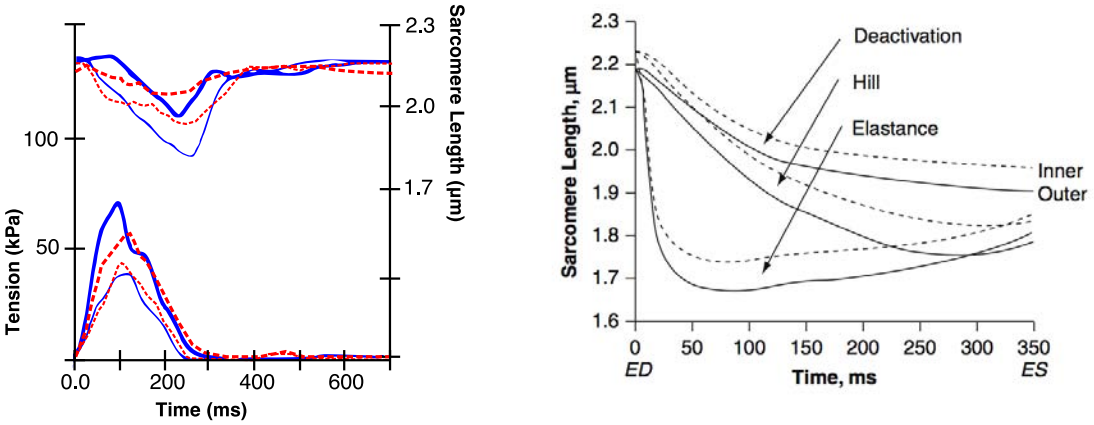

(a) (b)

FIGURE 7.40: (a) Clinically found results for active tension and Sarcomere lengths [52]. (b) Computational model results for sarcomere lengths for different active tension models [48].

The active tension for the model is slightly lower than expected, especially with respect to epicardial active tension, which declines to zero for a number of positions on the left ventricle. This is due to the dramatic decrease in sarcomere length, which falls below the minimum required length of l_0 to develop active tension. The calculation of the sarcomere length for the *Cosserat* fibre model is slightly different from that presented in Guccione et al. [49]. In Guccione, the computational model utilizes Cauchy Green strain and subsequently the sarcomere length is calculated as

$$l_s = l_{s_0}\sqrt{\mathrm{tr}(\mathbf{C}\mathbf{M}_\mathrm{f})}.$$

This form is meant to scale the original sarcomere length by the stretch in fibre direction. This slight discrepancy $\sqrt{\mathrm{tr}(\mathbf{C}\mathbf{M}_\mathrm{f})} \neq \mathrm{tr}(\mathbf{U}\mathbf{M}_\mathrm{f})$, results in lower sarcomere lengths in the *Cosserat* fibre model. While beyond the scope of this research, this could be remedied by imposing a mathematical scaling on l_0, allowing the model to develop active tension for lower sarcomere lengths and recalibrating the active tension model.

Clinical measures

A healthy ejection fraction, Eq. (6.13), for most animals is approximately 50% [139]. This differs however with humans, who have a significantly higher ejection fraction (Schlosser et al. [128] gives the normal ejection fraction in humans as 59.9% $\pm$ 14.4%). The canine left ventricle has a slightly lower ejection fraction, reported at 47.0% [139] and 42.0% $\pm$ 2.0% [109]. The resulting ejection fraction from the computational results of Kerckhoffs [72] at 50% is mildly higher than the literature values and would result in the left ventricle returning to the original unloaded state at the end of the cardiac cycle.

The computational results yielded an ejection fraction of 45.8%, which falls in line with the literature values, and also provides a subsequent advantage for further modelling. As the first cycle will not return to the zero stress state after isovlumetric relaxation, the first cardiac cycle would maintain some residual stress. Subsequent cardiac modelling starting from this point, would start passive filling with a residual pressure and stress state, which is a more accurate reflection of the *in vivo* ventricle [100, 113].

The fractional shortening, Eq. (6.14), for the canine has a large range from $20\% - 45\%$ [32, 98] . The computational result, 21.59% falls into the lower range of the literature values. While within the normal range, it does imply that the computational model is less contractile than the average canine left ventricle.

A fair amount of interest revolves around the timing of the cardiac cycle, otherwise known as hemodynamics. The key measures of the *Cosserat* fibre model, being the duration of isovolumetric contraction Δt_{IVC} and ejection Δt_{Ej}, are presented in Table 7.13 alongside other computational studies and literatures values. While the duration of ejection compares favourably to other computational models and literature values, the duration of isovolumetric contraction is slightly lower than other studies. The duration of $25ms$ is still within the range of literature values, given as $40 \pm 22ms$.

TABLE 7.13: Duration of ejection and isovolumetric contraction for the canine left ventricle.

Parameter	Cauchy	Kerckhoffs et al	*Cosserat* fibre	Literature range
Δt_{ivc} (ms)	52	44	25	40 ± 22 [81]
Δt_{ej} (ms)	212	194	202	$170 - 226$ [81, 85, 142]

Incompressibility

Physiologically, the myocardium are perfused with blood and contain deformable vessels, which affect the total volume of the myocardial walls during the cardiac cycle [10, 140]. Changes in myocardium volume between end diastole and end systole are low, with a

range between 1% - 15% [7, 114, 149], indicating that the myocardium are near incompressible, or at the most, weakly compressible. The *Cosserat* fibre model produces a volume change of 50% between EDV and EDS, which is roughly three times as much as the high range values found in literature. This can be remedied by increasing the value for A_{comp}, however the model is prone to numerical locking for high values of A_{comp} during systole, and the choice of $A_{comp} = 0.5$ was found to be the most stable choice for numerical experiments. The issue of numerical locking warrants further investigation, and recommendations are made in the concluding chapter. The discrepancy between the numeric and physiological result could also stem from the numerical model starting the cardiac cycle in the unloaded state, without any residual stresses. A pre-stressed configuration of the left ventricle may yield more favourable results with regards to incompressibility. Until subsequent cardiac cycles can be performed utilizing a pre-stressed configuration of the left ventricle at the start of the cardiac cycle, it remains inconclusive to the degree this is a flaw in the *Cosserat* fibre model.

Influence of the characteristic length

The inclusion of l as a material parameter introduces a feature of the micro space into the problem, and allows for the direct inclusion of higher order strains in the constitutive law describing the material. These provide a more detailed and physiologically accurate description of the material.

To measure the influence of the characteristic length, the cardiac cycle from the start of passive filling to the end of ejection was modelled without any inclusion of the change in curvature strains, i.e $l = 0.0$. Results from this model were compared to the calibrated *Cosserat* model whereby $l = 0.6622$. Comparative analysis between these two sets of model results revealed that the inclusion of higher order strains predominantly affects the systolic stage of the cardiac cycle. Regional mechanical features for both models are presented in Figure 7.41.

As one would expect, the lack of defined curvature stiffness allowed for the left ventricle to twist more freely. This is illustrated in Figure 7.41(b), whereby a particle on the epicardium surface and along the equator experiences significantly larger displacements. Differences are marginal in the passive filling stage, as the ventricle merely inflates with little torsional deformation. This increase in deformation yields a larger material stress which is illustrated in Figure 7.41(c). The most noteworthy result is perhaps the similarity in the pressure volume curves, Figure 7.41(a), despite the clear discrepancies in material deformation and stress.

This result, motivated a more detailed stress analysis, to be performed at multiple points along the myocardium. This was done at four longitudinal regions of the left ventricle,

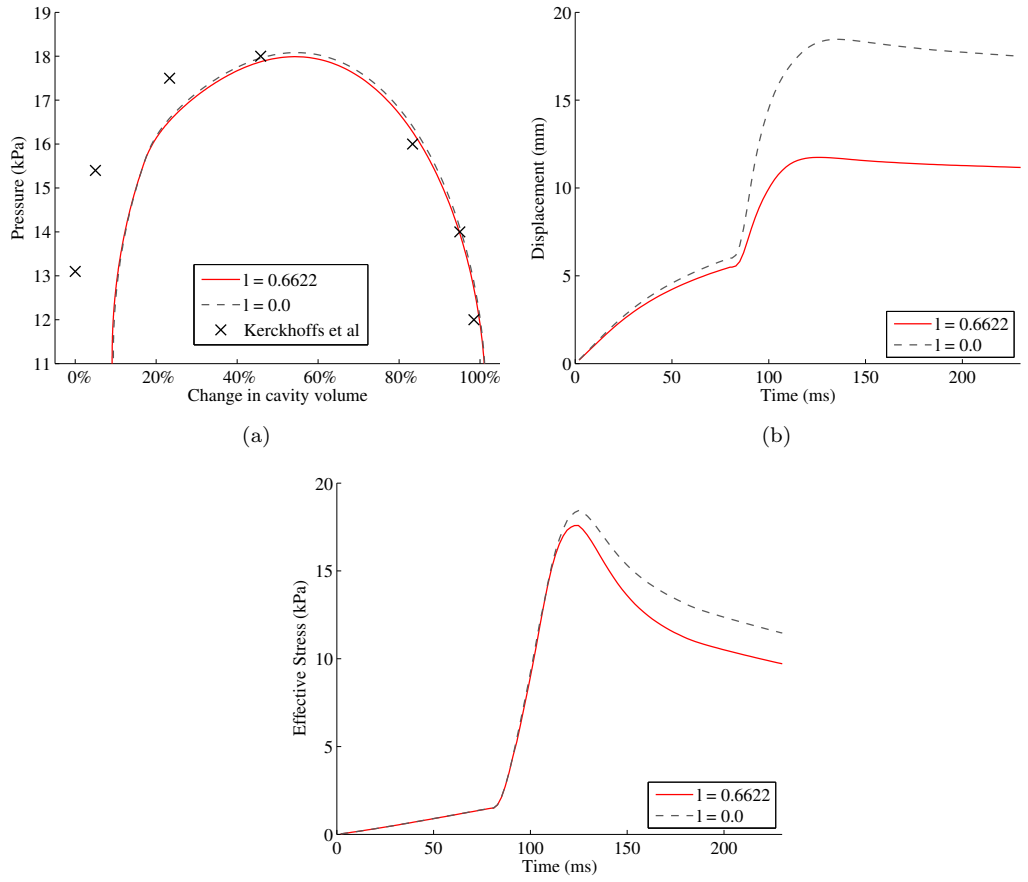

FIGURE 7.41: Comparison of computational results between the calibrated *Cosserat* fibre model, and the case where $l = 0.0$ for (a) the pressure volume relationship during ejection, (b) a particle displacement from the equator of the canine left ventricle, (c) the associated total effective stress for the same particle.

spaced equally apart as illustrated in Figure 7.42. At these positions, a stress analysis was performed on positions corresponding to the endocardium, midwall and epicardium.

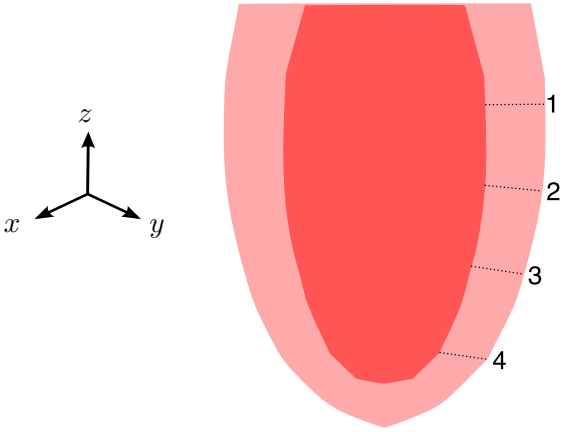

FIGURE 7.42: Labelled sampling points from the canine left ventricle utilized in the stress analysis between models.

The full difference between the effective stress of the two models is displayed in Figure 7.43. Here the L_2 normed difference between the models is presented, normalized with respect to the *Cosserat* fibre model. The analysis may explain the similarity in the pressure volume relationships between the two models: the majority of the points investigated had similar stress responses throughout the cardiac cycle, particularly the midwall region. However, there seems to be larger discrepancies on the endocardium, which from previous analysis, has shown to experience larger strains in general.

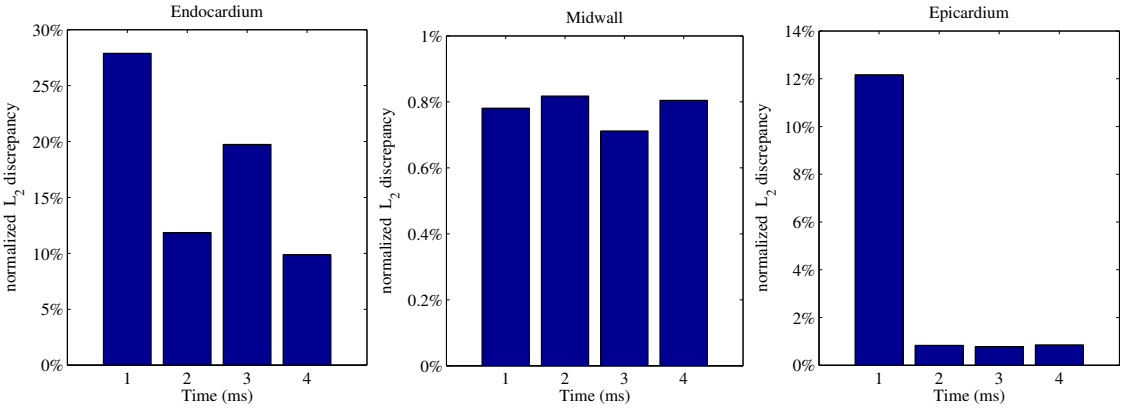

(a) Endocardium (b) Midwall (c) Epicardium

FIGURE 7.43: The discrepancies in effective stress results for the calibrated *Cosserat* fibre model, and the case where $l = 0.0$ at sampling points labelled in Figure 7.42.

The endocardium stress response in the *Cosserat* fibre model was significantly higher for all points, indicating that at large strains, the additional curvature stiffness contribute significantly to the material response. The discrepancies in the material stress for the midwall, and the majority of the epicardium are significantly lower. Both models exhibit the characteristic peak stress found at the midwall, which is consistent with previous findings.

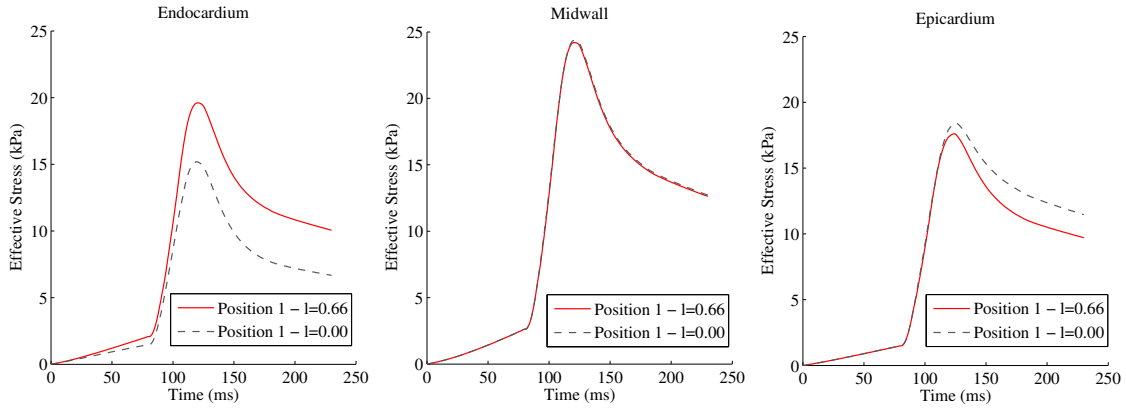

(a) Endocardium (b) Midwall (c) Epicardium

FIGURE 7.44: The effective stress results for the calibrated *Cosserat* fibre model, and the case where $l = 0.0$ at position 1 (i.e the equator) for different radial depths.

Interesting to note is that the discrepancies at the epicardium result in the *Cosserat* fibre model experiencing lower stresses than in the case where $l = 0.0$. This is significantly pronounced, at the equator, where the lack of curvature stiffness combined with the shortening of the minor axis, results in larger deformation and higher stress in the case where $l = 0.0$. It may be that increases and decreases between stress at local regions may average out on the global mechanical response.

One can conclude that the addition of the change in curvature stress into the kinematics and constitutive law has a meaningful and quantifiable influence on the regional material response of the myocardium. The changes in material response that result from the inclusion of the characteristic length are non-uniform across the model geometry and, in the case of the endocardium surface, can be as high as 25%. This is especially important when considering localized analysis on stress and strain which is particularly relevant for the case of acute myocardial infarction, whereby a region of the left ventricle is weakened.

Chapter 8

Conclusion

The major objective of this research was to introduce a novel continuum description for cardiac tissue and launch an initial investigation into the application for cardiac mechanics. This chapter will summarise the major findings, acknowledge any potential shortcomings and outline the future work for the research.

8.1 Summary and concluding remarks

The *Cosserat* fibre continuum description for cardiac tissue was successfully developed, introducing a feature of the micro structure into the kinematics and constitutive laws of the problem description. Together, alongside a mathematical model of the left ventricle, initial investigations into cardiac mechanics were introduced with significant results. The model describes the mechanical function of the heart, together with boundary conditions that simulate the cardiac cycle from the beginning of passive filling to the end of ejection. The geometry of the left ventricle was approximated using a truncated ellipsoid, with the description of fibre orientation consistent with experimental data.

Both linear and nonlinear constitutive laws were developed for the *Cosserat* fibre model which considered non-homogenised and homogenised contributions from the extra cellular matrix and fibre bundle components. Additionally an invariant constitutive law Eq. (5.30) was developed for the nonlinear model.

Linear constitutive laws were able to successfully replicate small strain results for a comparative Cauchy based model [82]. Utilizing the shear experimental data of Dokos et al. [30], the material anisotropy was calibrated which included the characteristic length l. The uniqueness of l cannot be confirmed without further experimental data, which

forced the identification process to select the value for l which led to the closest fit to the experimental data, provided by a Levenberg Marquad optimization algorithm.

The passive mechanics of the heart was described by the nonlinear transversely isotropic constitutive law with a penalty term to enforce incompressibility, Eq. (5.13). This constitutive law was able to reproduce, qualitatively and quantitatively, the characteristic nonlinear pressure volume curve for diastolic filling. With the identification of stress scaling material paramters A, B and A_{comp}, the simulation results were well within experimental results for the rat left ventricle [21, 55, 99] and the computational results of the canine left ventricle [72].

Two diseased cases relating to myocardial infarction were modelled for the passive case. Results for the left ventricle with an infarct in the acute ischemic and the fibrotic stage, followed closely to the qualitative descriptions found in the literature [11, 53, 56]. While some findings can be deduced from the passive results, i.e that in the acute ischemic case the high strains and strain gradients in the infarct region expose the area to a greater risk of rupture or permanent deformation, further investigation into the ventricular function and regional behaviour during systole is needed for conclusive analysis. More realistic model simulations can also be constructed to provide more accurate results. These could include a thinner wall thickness for the infarct region in the fibrotic stage, the inclusion of an infarct border zone or utilizing the homogenised approach to accurately reflect the higher collagen content in the remodelled infarct [69].

The systolic stage of the healthy canine left ventricle was simulated with mixed success. Basic metrics of cardiac function such as ejection fraction and fractional shortening measured favourably against literature findings. During contraction the ellipsoid produces the characteristic torsion that has been found experimentally. The active tension of the left ventricle was modelled using the Guccione et al. [51] active stress model, where active stress is added to the aforementioned passive stress. A slightly different formulation was introduced based on the first *Cosserat* strain tensor $\mathbf{U}$ as was necessary to be consistent with our model. The evolution of the sarcomere lengths and active tension in the *Cosserat* fibre model while still within the reasonable range of results, was slightly lower than those found in literature. Despite this, the model was able to reproduce clinically measured features like the ejection fraction and ejection timing significantly well.

To avoid numerical locking during ejection, the incompressibility constraint was deliberately weakened, which in turn may have affected the slightly below average active tension development on the epicardium. Without repetitive cardiac cycles, it is inconclusive how significant this under performance is.

The materially calibrated characteristic length was shown to have a significant and meaningful influence on the material description of the left ventricle. This was most prominent during systole and especially so during ejection. Regional material response was quantifiable different due to the inclusion of higher order strains in the constitutive law description. These differences may be averaged out on the global scale, when measuring the left ventricle's ability to pump blood, as the pressure volume relation was only modestly influenced. However, from a mechanical standpoint, the material description is meaningfully different. This has serious implications when considering the infarct region of the left ventricle following acute ischemia. The thinning of the infarct region and potential risk of rupture is related to the regional stress and strain distribution [11, 56].

8.2 Future work

Numerical locking and Incompressibility

Further investigation is recommended to analyse the source of numerical locking and how weakening the incompressibility constraint avoids it. Numerical locking with element-free Galerkin methods is rare, and the problem may not be related to incompressibility. Nonetheless, it is recommended that different methods of enforcing incompressibility should be investigated to evaluate the most compatible approach with the *Cosserat* fibre model.

The cardiac cycle

As an initial investigation the current research presents results up until the end of systole. The isovolumetric relaxation phase has been excluded, due to time constraints. Initial investigation into the modelling and computational results shows that the *Cosserat* fibre model is compatible with this phase, and that expected material response is present. i.e steady reduction in stress throughout the material and subsequent untwisting. In further work, the isovolumetric phase must be included with sufficient analysis to accompany it.

The next phase of investigation would be to run multiple cardiac cycles, in a continuous computational experiment. The final deformation of the ventricle at the end of one cycle is used as the starting point for the subsequent cycle. In this way, residual stress can be included in the model and a more realistic cardiac cycle can be modelled. Additionally with the inclusion of multiple cycles, further analysis can be performed that would otherwise be unavailable. This includes metrics like heart rate (measured in

beats per minute) and cardiac phenomena like the Frank-Starling mechanism (for more information see [125]).

Material experiments for tissue specimens

The current research is substantially limited by the availability of experimental data available in the literature. Specifically with respect to material testing of higher order curvature deformations. In order to obtain a unique and accurate material value for the characteristic length l, further research is needed into experimental testing on cardiac tissue specimens. Ideally, a study detailing the fibre orientation of tissue specimens undergoing shear deformations (as in [30]) would be accompanied by experiments investigating the torsional response for the same species. This would provide enough data to define the material anisotropy for a fully orthotropic constitutive law and provide enough information to confidently identify a unique characteristic length.

Application to non symmetric geometries

Establishing a model that can handle realistic geometries is an important objective that would allow for a more realistic analysis of cardiac mechanics. The application of the kinematics and the enforcement of the boundary conditions remains relatively straightforward. The application of a constitutive law which is fibre dependant is far from trivial. There are two main approaches on how to overcome this. The first is define the fibre direction *a priori*, which is usually achieved from extracting density information from MRI images. The second technique, relies on the definition of the fibre orientation on the reference geometry and projects the orientation through a mapping onto the new realistic geometry.

Appendix A

Additional derivations

A.1 Alternative fibre coordinate derivation

The following derivation is highly compatible with implementation. In the case where the fibre coordinate system is orthonormal the following can be applied.

Coordinate transformation of tensor components

Consider a vector quantity v, whether expressed in the cartesian coordinate system, or the fibre coordinate system, the vector quantity remains unchanged, even though the component may differ under the different frame description. That is to say

$$\mathbf{v} = \sum_{i}^{3} v_i \boldsymbol{e}_i = \sum_{i}^{3} \acute{v}_i \mathbf{V}_i \tag{A.1}$$

For the purpose of deriving a relationship between the different coordinate systems, let Q_{ij} denote the dot products between the two bases as

$$Q_{ij} = \mathbf{e}_i \cdot \mathbf{V}_j. \tag{A.2}$$

Utilizing this component matrix we can easily construct transformation from one coordinate system into the other. This can be seen quite easily when considering the following reasoning,

$$\begin{aligned} \mathbf{e}_i = \mathbf{e}_i \mathbf{1} &= \mathbf{e}_i(\mathbf{V}_j \otimes \mathbf{V}_j) \\ &= (\mathbf{e}_i \cdot \mathbf{V}_j)\mathbf{V}_j \\ &= Q_{ij}\mathbf{V}_j \ . \end{aligned}$$

Where the convention of summing over repeated indices has been assumed. The following relationships hold are equally valid

$$\mathbf{e}_i = Q_{ij}\mathbf{V}_j \qquad \text{and} \qquad \mathbf{V}_i = Q_{ji}\mathbf{e}_j. \tag{A.3}$$

It's clear that Q_{ij} describe the components of a second order transformation tensor $\mathbf{Q}$, whereby the first and second indices correspond to the Cartesian frame and the fibre reference frame respectively $\mathbf{Q} = Q_{ij}\mathbf{e}_i \otimes \mathbf{V}_j$. Retrieving components of the vector v in whichever reference frame can be achieved in the following manner

$$\mathbf{v} = \mathbf{Q}\acute{\mathbf{v}} \qquad \text{and} \qquad \acute{\mathbf{v}} = \mathbf{Q}^T\mathbf{v}. \tag{A.4}$$

Similarly second order tensor quantities can be projected onto the fibre reference frame by considering the conversion of each of the bases. To achieve this one needs to contract the second order tensor with two transformation tensors

$$\begin{aligned}\mathbf{Q}^T\mathbf{T}\mathbf{Q} &= T_{ij}\mathbf{Q}^T\mathbf{e}_i \otimes \mathbf{e}_j\mathbf{Q} \\ &= T_{mn}Q_{mr}Q_{ns}\mathbf{V}_r \otimes \mathbf{V}_s \\ &= \acute{T}_{ij}\mathbf{V}_i \otimes \mathbf{V}_j \ .\end{aligned}$$

In general, second order tensor components can be related by the different coordinate frames in the following manner

$$\acute{T}_{ij} = Q_{mi}T_{mn}Q_{nj} \qquad \text{and} \qquad T_{ij} = Q_{im}\acute{T}_{mn}Q_{jn}. \tag{A.5}$$

For the purpose of modelling one dimensional *Cosserat* rods, consider a one-dimensional fibre continuum mapped by the coordinate $s = s(\vartheta^i)$. As such the fibre is assumed to be embedded in three dimensional space. The fibre deformation gradient is given by:

$$\mathbf{F}^{(s)} = \frac{\partial \mathbf{x}}{\partial \vartheta^i}\frac{\partial \vartheta^i}{\partial s} \otimes \mathbf{V}_F = \mathbf{v}_F \otimes \mathbf{V}_F \tag{A.6}$$

where $\mathbf{V}_F$ denotes a vector in fibre direction and the fibre direction in the current configuration is expressed by $\mathbf{v}_F = \mathbf{F}\mathbf{V}_F$. In this sense, $\mathbf{F}^{(s)}$ is the projection of the deformation gradient $\mathbf{F}$ in direction of the fibre. An equivalent formulation, makes use of the change of coordinate tensor $\mathbf{Q}$. The deformation gradient is written in terms of the fibre local coordinate system

$$\acute{F}_{ij}\mathbf{V}_i \otimes \mathbf{V}_j = Q_{mi}F_{mn}Q_{nj}\mathbf{V}_i \otimes \mathbf{V}_j, \tag{A.7}$$

A.2 Linearisation of the variational statement

Consider the internal work of the variational statement in the following form:

$$\mathcal{W}_{int} = \int_{\mathcal{B}} \{\boldsymbol{n} : \delta\mathbf{U} + \boldsymbol{m} : \delta\mathbf{K}\}\, dV \tag{A.8}$$

The linearisation of this statement produces the following terms

$$\int_{\mathcal{B}} \frac{\partial \boldsymbol{n}}{\partial \mathbf{U}} \Delta\mathbf{U} : \delta\mathbf{U} dV \; + \tag{A.9}$$

$$\int_{\mathcal{B}} \frac{\partial \boldsymbol{n}}{\partial \mathbf{K}} \Delta\mathbf{K} : \delta\mathbf{U} dV \; + \tag{A.10}$$

$$\int_{\mathcal{B}} \frac{\partial \boldsymbol{m}}{\partial \mathbf{U}} \Delta\mathbf{U} : \delta\mathbf{K} dV \; + \tag{A.11}$$

$$\int_{\mathcal{B}} \frac{\partial \boldsymbol{m}}{\partial \mathbf{K}} \Delta\mathbf{K} : \delta\mathbf{K} dV \; + \tag{A.12}$$

$$\int_{\mathcal{B}} \{\boldsymbol{n} : \Delta\delta\mathbf{U} + \boldsymbol{m} : \Delta\delta\mathbf{K}\}\, dV \tag{A.13}$$

Consider the first couple term (A.10) in index notation,

$$\int_{\mathcal{B}} \frac{\partial n_{ij}}{\partial K_{kl}} \Delta K_{kl} : \delta U_{ij} dV, \tag{A.14}$$

the double contraction sign, : is kept purely for convenience of separating terms. Consider the introduction of fourth order *Tangent Stiffness* tensors denoted by $\boldsymbol{\mathcal{H}}^{(i)},\ i = 1, 2, 3, 4$ for each of the first four terms (A.9) - (A.12). The term to integrated can now be expressed in the following way

$$\mathcal{H}^{(2)}_{ijkl} \Delta K_{kl} : \delta U_{ij}, \tag{A.15}$$

The variants of ΔK_{kl} and δU_{ij} can be expressed in terms of y and δu (and w, because $\mathbf{U} = \mathbf{R}^T\mathbf{F}$) in the following manner,

$$\begin{aligned} &= \mathcal{H}^{(2)}_{ijkl} R_{mk} y_{m,l} : \{(-R^T W F)_{ij} + (R^T \delta F)_{ij}\} \\ &= \mathcal{H}^{(2)}_{ijkl} R_{mk} y_{m,l} : \{-R_{ri}\epsilon_{rst} F_{sj} w_t + R_{ni}\delta F_{nj}\} \\ &= \mathcal{H}^{(2)}_{ijkl} R_{mk} y_{m,l} : \{-R_{ri}\epsilon_{rst} F_{s,j} w_t + R_{ni}\delta u_{n,j}\} \end{aligned} \tag{A.16}$$

In the same manner we deal with the second couple term

$$\mathcal{H}^{(3)}_{ijkl}\Delta U_{kl} : \delta K_{ij}, \tag{A.17}$$

The variants of ΔU_{kl} and δK_{ij} can be expressed in terms of Δu and w in the following manner,

$$\begin{aligned} &= \mathcal{H}^{(3)}_{ijkl}\{(-R^T Y F)_{kl} + (R^T \Delta F)_{kl}\} : R_{mi} w_{m,j} \\ &= \mathcal{H}^{(3)}_{ijkl}\{-R_{rk}\epsilon_{rst}F_{sl}y_t + R_{nk}\Delta F_{nl}\} : R_{mi} w_{m,j} \\ &= \mathcal{H}^{(3)}_{ijkl}\{-R_{rk}\epsilon_{rst}F_{s,l}y_t + R_{nk}\Delta u_{n,l}\} : R_{mi} w_{m,j} \end{aligned} \tag{A.18}$$

This leaves the following additional expression to include in the code

$$+\mathcal{H}^{(2)}_{ijkl}R_{mk}R_{ni}\|\delta u_{n,j}y_{m,l} \tag{A.19}$$

$$-\mathcal{H}^{(2)}_{ijkl}R_{mk}R_{ri}\epsilon_{rst}F_{s,j}\|y_{m,l}w_t \tag{A.20}$$

$$-\mathcal{H}^{(3)}_{ijkl}R_{rk}\epsilon_{rst}R_{mi}F_{s,l}\|w_{m,j}y_t \tag{A.21}$$

$$+\mathcal{H}^{(3)}_{ijkl}R_{nk}R_{mi}\|w_{m,j}\Delta u_{n,l} \tag{A.22}$$

Variants of the *Cosserat* strains

The variation of $\mathbf{U}$ is expressed as:

$$\begin{aligned} \delta\mathbf{U} &= \delta(\mathbf{R}^T\mathbf{F}) = \delta\mathbf{R}^T\mathbf{F} + \mathbf{R}^T\delta\mathbf{F} \\ &= (\mathbf{W}\mathbf{R})^T\mathbf{F} + \mathbf{R}^T\delta\mathbf{F} \end{aligned} \tag{A.23}$$

Note that variations of rotations are not only multiplicative, but for the quasi-static case we only consider the so called *left group action* as$\mathbf{W}$ is skew-symmetric. This allows us to express:

$$\begin{aligned} \delta\mathbf{U} &= -\mathbf{R}^T\mathbf{W}\mathbf{F} + \mathbf{R}^T\delta\mathbf{F} \\ &= -\mathbf{R}^T\mathbf{W}\mathbf{F} + \mathbf{R}^T\delta\mathbf{u}_{,i} \otimes \mathbf{G}^i \end{aligned} \tag{A.24}$$

We are able to express $\delta\mathbf{K}$ through it's axial vector $\mathbf{k}$ in a similar manner to how we obtained (A.24) as

$$\delta\mathbf{k}_i = \text{axial}\{\delta(\mathbf{R}^T\mathbf{R}_{,i})\} = \mathbf{R}^T\mathbf{w}_{,i}\ . \tag{A.25}$$

Where $\mathbf{w}$ is the axial vector of $\mathbf{W}$.

A.3 Additional derivations for the invariant formulation

$$\begin{aligned}
\frac{\partial Q}{\partial J_i}\frac{\partial J_i}{\partial \mathbf{U}} &= 2b_1\,J_4\,\frac{\partial J_4}{\partial \mathbf{U}} + 2b_2\,J_5\,\frac{\partial J_5}{\partial \mathbf{U}} + 2b_3\,J_6\,\frac{\partial J_6}{\partial \mathbf{U}} + b_4\,\frac{\partial J_7}{\partial \mathbf{U}} + b_5\,\frac{\partial J_8}{\partial \mathbf{U}} + b_6\,\frac{\partial J_9}{\partial \mathbf{U}} = \\
&= 2b_1\,J_4\,\mathbf{M}_f + 2b_2\,J_5\,\mathbf{M}_t + 2b_3\,J_6\,\mathbf{M}_n + b_4\,\mathbf{U}\mathbf{M}_f + b_5\,\mathbf{U}\mathbf{M}_t + b_6\,\mathbf{U}\mathbf{M}_n = \\
&= \Big(2b_1\,J_4\,(\mathbf{M}_f)_{ij} + 2b_2\,J_5\,(\mathbf{M}_t)_{ij} + 2b_3\,J_6\,(\mathbf{M}_n)_{ij} + b_4\,U_{ik}\,(\mathbf{M}_f)_{kj} + \\
&\quad b_5\,U_{ik}\,(\mathbf{M}_t)_{kj} + b_6\,U_{ik}\,(\mathbf{M}_n)_{kj}\Big)\mathbf{e}_i\otimes\mathbf{e}_j\otimes\mathbf{e}_k\otimes\mathbf{e}_l
\end{aligned}$$

with

$$\begin{aligned}
\frac{\partial J_1}{\partial \mathbf{U}} &= \frac{\partial (tr\mathbf{U})}{\partial \mathbf{U}} = \mathbf{1} \\
\frac{\partial J_2}{\partial \mathbf{U}} &= \frac{\partial (tr\mathbf{U}^T\mathbf{U})}{\partial \mathbf{U}} = 2\mathbf{U} \\
\frac{\partial J_4}{\partial \mathbf{U}} &= \frac{\partial (tr(\mathbf{U}\mathbf{M}_f))}{\partial \mathbf{U}} = \mathbf{M}_f \\
\frac{\partial J_5}{\partial \mathbf{U}} &= \frac{\partial (tr(\mathbf{U}\mathbf{M}_t))}{\partial \mathbf{U}} = \mathbf{M}_t \\
\frac{\partial J_6}{\partial \mathbf{U}} &= \frac{\partial (tr(\mathbf{U}\mathbf{M}_n))}{\partial \mathbf{U}} = \mathbf{M}_n \\
\frac{\partial J_7}{\partial \mathbf{U}} &= \frac{\partial (tr(\mathbf{U}^T\mathbf{U}\mathbf{M}_f))}{\partial \mathbf{U}} = 2\mathbf{U}\mathbf{M}_f \\
\frac{\partial J_8}{\partial \mathbf{U}} &= \frac{\partial (tr(\mathbf{U}^T\mathbf{U}\mathbf{M}_t))}{\partial \mathbf{U}} = 2\mathbf{U}\mathbf{M}_t \\
\frac{\partial J_9}{\partial \mathbf{U}} &= \frac{\partial (tr(\mathbf{U}^T\mathbf{U}\mathbf{M}_n))}{\partial \mathbf{U}} = 2\mathbf{U}\mathbf{M}_n
\end{aligned}$$

and

$$\begin{aligned}
\frac{\partial^2 J_7}{\partial \mathbf{U}\partial \mathbf{U}} &= \frac{\partial (U_{im}(\mathbf{M}_f)_{mj})}{\partial U_{kl}} = 2\delta_{ik}\,(\mathbf{M}_f)_{jl}\,\mathbf{e}_i\otimes\mathbf{e}_j\otimes\mathbf{e}_k\otimes\mathbf{e}_l \\
\frac{\partial^2 J_8}{\partial \mathbf{U}\partial \mathbf{U}} &= \frac{\partial (U_{im}(\mathbf{M}_t)_{mj})}{\partial U_{kl}} = 2\delta_{ik}\,(\mathbf{M}_t)_{jl}\,\mathbf{e}_i\otimes\mathbf{e}_j\otimes\mathbf{e}_k\otimes\mathbf{e}_l \\
\frac{\partial^2 J_9}{\partial \mathbf{U}\partial \mathbf{U}} &= \frac{\partial (U_{im}(\mathbf{M}_n)_{mj})}{\partial U_{kl}} = 2\delta_{ik}\,(\mathbf{M}_n)_{jl}\,\mathbf{e}_i\otimes\mathbf{e}_j\otimes\mathbf{e}_k\otimes\mathbf{e}_l
\end{aligned}$$

Also, we consider the linearization of $\boldsymbol{n}$

$$\begin{aligned}
\frac{\partial \boldsymbol{n}}{\partial \mathbf{U}} &= \frac{1}{2}AB^2\exp^{BQ}\frac{\partial Q}{\partial J_i}\frac{\partial J_i}{\partial \mathbf{U}}\frac{\partial Q}{\partial J_j}\frac{\partial J_j}{\partial \mathbf{U}} + \frac{1}{2}A\exp^{BQ}\frac{\partial Q}{\partial J_i}\frac{\partial^2 J_i}{\partial \mathbf{U}\partial \mathbf{U}} + \\
&\quad \frac{1}{2}A\exp^{BQ}\frac{\partial^2 Q}{\partial J_i\partial J_j}\frac{\partial J_i}{\partial \mathbf{U}}\frac{\partial J_j}{\partial \mathbf{U}} + \text{compressibility term}
\end{aligned} \tag{A.26}$$

with

$$\begin{aligned}
\frac{\partial Q}{\partial J_i}\frac{\partial J_i}{\partial \mathbf{U}}\frac{\partial Q}{\partial J_j}\frac{\partial J_j}{\partial \mathbf{U}} &= (2b_1\, J_4\,(\mathbf{M}_f)_{ij} + 2b_2\, J_5\,(\mathbf{M}_t)_{ij} + 2b_3\, J_6\,(\mathbf{M}_n)_{ij} + b_4\, U_{ik}\,(\mathbf{M}_f)_{kj} + \\
&\quad b_5\, U_{ik}\,(\mathbf{M}_t)_{kj} + b_6\, U_{ik}\,(\mathbf{M}_n)_{kj}) \\
&\quad (2b_1\, J_4\,(\mathbf{M}_f)_{kl} + 2b_2\, J_5\,(\mathbf{M}_t)_{kl} + 2b_3\, J_6\,(\mathbf{M}_n)_{kl} + b_4\, U_{km}\,(\mathbf{M}_f)_{ml} + \\
&\quad b_5\, U_{km}\,(\mathbf{M}_t)_{ml} + b_6\, U_{km}\,(\mathbf{M}_n)_{ml}) \\
\frac{\partial Q}{\partial J_i}\frac{\partial^2 J_i}{\partial \mathbf{U}\partial \mathbf{U}} &= b_4\,\frac{\partial J_7}{\partial \mathbf{U}}\,\frac{\partial^2 J_7}{\partial \mathbf{U}\partial \mathbf{U}} + b_5\,\frac{\partial J_8}{\partial \mathbf{U}}\,\frac{\partial^2 J_8}{\partial \mathbf{U}\partial \mathbf{U}} + b_6\,\frac{\partial J_9}{\partial \mathbf{U}}\,\frac{\partial^2 J_9}{\partial \mathbf{U}\partial \mathbf{U}} = \\
&= 2\,\delta_{ik}\Big(b_4\,(\mathbf{M}_f)_{jl} + b_5\,(\mathbf{M}_t)_{jl} + b_6\,(\mathbf{M}_n)_{jl}\Big)\mathbf{e}_i \otimes \mathbf{e}_j \otimes \mathbf{e}_k \otimes \mathbf{e}_l \\
\frac{\partial^2 Q}{\partial J_i \partial J_j}\frac{\partial J_i}{\partial \mathbf{U}}\frac{\partial J_j}{\partial \mathbf{U}} &= 2b_1\,\frac{\partial J_4}{\partial \mathbf{U}}\,\frac{\partial J_4}{\partial \mathbf{U}} + 2b_2\,\frac{\partial J_5}{\partial \mathbf{U}}\,\frac{\partial J_5}{\partial \mathbf{U}} + 2b_3\,\frac{\partial J_6}{\partial \mathbf{U}}\,\frac{\partial J_6}{\partial \mathbf{U}} = \\
&= 2\Big(b_1\,(\mathbf{M}_f)_{ij}\,(\mathbf{M}_f)_{kl} + b_2\,(\mathbf{M}_t)_{ij}\,(\mathbf{M}_t)_{kl} + b_3\,(\mathbf{M}_n)_{ij}\,(\mathbf{M}_n)_{kl}\Big)\mathbf{e}_i \otimes \mathbf{e}_j \otimes \mathbf{e}_k \otimes \mathbf{e}_l
\end{aligned}$$

A.4 Transformation between Prolate spheroid and Cartesian coordinates

In Section 6.2.1, the Cartesian coordinates were given as

$$x = C\sinh(\eta)\sin(\theta)\cos(\phi) \tag{A.27}$$

$$y = C\sinh(\eta)\sin(\theta)\sin(\phi) \tag{A.28}$$

$$z = C\cosh(\eta)\cos(\theta) \tag{A.29}$$

To isolate an expression for ϕ comes naturally from the combination of Eqs. (A.27) and (A.28) whereby

$$\frac{y}{x} = \tan(\phi) \tag{A.30}$$

To find expressions for the focal points consider the focal points of the ellipse, d_1 and d_2 defined by

$$d_1^2 = (z + C)^2 + x^2 + y^2 \tag{A.31}$$

$$d_2^2 = (z - C)^2 + x^2 + y^2, \tag{A.32}$$

and a simplification for $x^2 + y^2$ which is given by

$$\begin{aligned}
x^2 + y^2 &= C^2\sinh^2(\eta)\sin^2(\theta)\left(\cos^2(\phi) + \sin^2(\phi)\right) \\
&= C^2\sinh^2(\eta)\sin^2(\theta).
\end{aligned} \tag{A.33}$$

The full expression for d_1 in prolate coordinates is given by

$$\begin{aligned} d_1 &= \sqrt{z^2 + 2zC + C^2 + C^2\sinh^2(\eta)\sin^2(\theta)} \\ &= C\sqrt{\cosh^2(\eta)\cos^2(\theta) + 2\cosh(\eta)\cos(\theta) + 1 + \sinh^2(\eta)\sin^2(\theta)}. \end{aligned} \tag{A.34}$$

Utilizing the trigonometric identities $\sinh^2\eta = \cosh^2\eta - 1$ and $\sin^2\theta + \cos^2\theta = 1$, allows us to impose simplifications to the expression such that

$$\begin{aligned} d_1 &= C\sqrt{\cosh^2(\eta)\cos^2(\theta) + 2\cosh(\eta)\cos(\theta) + 1 + \sinh^2(\eta)\sin^2(\theta)} \\ &= C\sqrt{\cosh^2(\eta)\cos^2(\theta) + 2\cosh(\eta)\cos(\theta) + 1 + \cosh^2(\eta)\sin^2(\theta) - \sin^2(\theta)} \\ &= C\sqrt{\cosh^2(\eta)(\cos^2(\theta) + \sin^2(\theta)) + 2\cosh(\eta)\cos(\theta) + 1 - \sin^2(\theta)} \\ &= C\sqrt{\cosh^2(\eta) + 2\cosh(\eta)\cos(\theta) + \cos^2(\theta)} \\ &= C\left(\cosh(\eta) + \cos(\theta)\right). \end{aligned} \tag{A.35}$$

The same derivation applied to the expression for d_2 yields

$$d_2 = C\left(\cosh(\eta) - \cos(\theta)\right). \tag{A.36}$$

This allows us to isolate θ and η in the following expressions

$$\cos(\theta) = \frac{d_1 - d_2}{2C} \tag{A.37}$$

$$\cosh(\eta) = \frac{d_1 + d_2}{2C}. \tag{A.38}$$

Appendix B

SESKA

SESKA is a C++ code built upon several libraries by Dr S. Skatulla since the start of the 2000s. The main software objective is to solve continuum mechanics problems utilizing the element free Galerkin method (EFG). The preprocessing, calculation process and post processing are all carried out by the code. The geometry definition and 3D solution visualisation are handled by the pre/post processing commercial software package, GiD. Most of SESKA's processes are parallelised using the OpenMPI library, thus allowing large problems to be solved on high performance computers.

The solving process in SESKA is outlined as follows: the construction of shape functions, assembly particle contributions to a global stiffness matrix and/or mass matrix (for dynamic problems) and solves the set of equations either in a linear or Newton Raphson scheme, depending on the problem description.

Shape functions

Since SESKA employs the EFG method, it needs to primarily find the supporting nodes of all individual particles belonging to the domain. Actually two methods have been used. Either, all the nodal distances relative to a particular particle is calculated and nodes found within the defined radius of support are included in a support particle list, or, the elements connectivity, within a mesh, is used to find the neighbouring nodes. Regarding the influencing zone, SESKA defines them in a flexible way. For example, a geometry with different densities of scattered nodes have different supporting radius. Their shape is defined as either a cuboid or a sphere, with the influence radius being different in each direction (useful if shape functions are computed while taking the anisotropic material properties into consideration). After finding all supporting nodes, the MLS method is then employed to calculate the shape functions and its derivatives.

Calculation

The calculation process is carried out using external libraries coupled with the constitutive laws setup in SESKA. The following packages are used:

BLAS Basic Linear Algebra Subprogram is a set of code that allows a user to perform common linear algebra operations. The functionality of BLAS library is characterised by three levels. Level 1 contains a vector-vector operations, Level 2, a vector-matrix operations and level 3, a matrix-matrix operations.

LAPACK Linear Algebra PACKage is a software library written in Fortran for numerical linear algebra. It contains routines to solve systems of linear equations, eigenvalue problems and single value decomposition. LAPACK heavily relies on the BLAS libraries to perform efficient matrix operations.

ParMETIS The ParMETIS library contains several highly efficient algorithms for mesh partitioning, matrix reordering and others primed for the use of parallelisation.

PETSc The Portable, Extensible Tool-kit for Scientific computation are libraries that allows BLAS, LAPACK and openMPI to work together in order to solve for scalable (i.e large) scientific computational problems. PETSc provides many of the mechanisms needed for solving large systems of equations within a parallel code environment, such as simple parallel matrix and vector assembly routines that allow the overlap of communication and computation.

Bibliography

[1] Jacob Aboudi, M-J Pindera, and Steven M Arnold. Higher-order theory for functionally graded materials. *Composites Part B: Engineering*, 30(8):777–832, 1999.

[2] EC Aifantis. Strain gradient interpretation of size effects. *International Journal of Fracture*, 95(1-4):299–314, 1999.

[3] Johannes Altenbach, Holm Altenbach, and Victor A Eremeyev. On generalized cosserat-type theories of plates and shells: a short review and bibliography. *Archive of Applied Mechanics*, 80(1):73–92, 2010.

[4] Ala Alwan et al. *Global status report on noncommunicable diseases 2010.* World Health Organization, 2011.

[5] T. Arts, P.C. Veenstra, and R.S. Reneman. Epicardial deformation and left ventricular wall mechanisms during ejection in the dog. *American Journal of Physiology-Heart and Circulatory Physiology*, 243(3):H379, 1982.

[6] El Arzt. Size effects in materials due to microstructural and dimensional constraints: a comparative review. *Acta materialia*, 46(16):5611–5626, 1998.

[7] Hiroshi Ashikaga, Benjamin A Coppola, Katrina G Yamazaki, Francisco J Villarreal, Jeffrey H Omens, and James W Covell. Changes in regional myocardial volume during the cardiac cycle: implications for transmural blood flow and cardiac structure. *American Journal of Physiology-Heart and Circulatory Physiology*, 295(2):H610–H618, 2008.

[8] Kenneth P Batts, Douglas M Ackermann, and William D Edwards. Postinfarction rupture of the left ventricular free wall: clinicopathologic correlates in 100 consecutive autopsy cases. *Human pathology*, 21(5):530–535, 1990.

[9] Rafael Beyar and Samuel Sideman. Left ventricular mechanics related to the local distribution of oxygen demand throughout the wall. *Circulation Research*, 58(5): 664–677, 1986.

[10] Arnaud Bistoquet, John Oshinski, and Oskar Skrinjar. Left ventricular deformation recovery from cine mri using an incompressible model. *Medical Imaging, IEEE Transactions on*, 26(9):1136–1153, 2007.

[11] D. K. Bogen, S. A. Rabinowitz, A. Needleman, T. A. McMahon, and W. H. Abelmannj. An analysis of the mechanical disadvantage of myocardial infarction in the canine left ventricle. *Circ Res*, 47(5):728–41, Nov 1980.

[12] J. Bonet and RD Wood. *Nonlinear Continuum Mechanics for Finite Element Analysis*. Cambridge University Press, 2008.

[13] PHM Bovendeerd, T. Arts, JM Huyghe, DH Van Campen, and RS Reneman. Dependence of local left ventricular wall mechanics on myocardial fiber orientation: a model study. *Journal of biomechanics*, 25(10):1129–1140, 1992.

[14] PHM Bovendeerd, J Rijcken, DH Van Campen, AJG Schoofs, K Nicolay, and T Arts. Optimization of left ventricular muscle fiber orientation. In *IUTAM Symposium on Synthesis in Bio Solid Mechanics*, pages 285–296. Springer, 2002.

[15] Maurice B Buchalter, James L Weiss, Walter J Rogers, Elias A Zerhouni, Myron L Weisfeldt, Rafael Beyar, and Edward P Shapiro. Noninvasive quantification of left ventricular rotational deformation in normal humans using magnetic resonance imaging myocardial tagging. *Circulation*, 81(4):1236–1244, 1990.

[16] Gerald Buckberg, Aman Mahajan, Saleh Saleh, Julien I.E. Hoffman, and Cecil Coghlan. Structure and function relationships of the helical ventricular myocardial band. *J Thorac Cardiovasc Surg*, 136(3):578–589, September 1, 2008.

[17] Gerald Buckberg, Julien IE Hoffman, Navin C Nanda, Cecil Coghlan, Saleh Saleh, and Constantine Athanasuleas. Ventricular torsion and untwisting: Further insights into mechanics and timing interdependence: A viewpoint. *Echocardiography*, 28(7):782–804, 2011.

[18] PM Buechner and RS Lakes. Size effects in the elasticity and viscoelasticity of bone. *Biomechanics and Modeling in Mechanobiology*, 1(4):295–301, 2003.

[19] Thomas Caceci. nanozoomer digital pathology. `http://vmserver.vetmed.vt.edu`. Accessed: 2013-11-27.

[20] James B Caulfield and Joseph S Janicki. Structure and function of myocardial fibrillar collagen. *Technology and Health Care*, 5(1):95–113, 1997.

[21] Oscar H Cingolani, Xiao-Ping Yang, Maria A Cavasin, and Oscar A Carretero. Increased systolic performance with diastolic dysfunction in adult spontaneously hypertensive rats. *Hypertension*, 41(2):249–254, 2003.

[22] Jack PM Cleutjens. The role of matrix metalloproteinases in heart disease. *Cardiovascular research*, 32(5):816–821, 1996.

[23] Jay N Cohn, Roberto Ferrari, and Norman Sharpe. Cardiac remodelingconcepts and clinical implications: a consensus paper from an international forum on cardiac remodeling. *Journal of the American College of Cardiology*, 35(3):569–582, 2000.

[24] Kim A Connelly, David L Prior, Darren J Kelly, Michael P Feneley, Henry Krum, and Richard E Gilbert. Load-sensitive measures may overestimate global systolic function in the presence of left ventricular hypertrophy: a comparison with load-insensitive measures. *American Journal of Physiology-Heart and Circulatory Physiology*, 290(4):H1699–H1705, 2006.

[25] Eugène Cosserat, François Cosserat, Maurizio Brocato, and Konstantinos Chatzis. *Théorie des corps déformables*. A. Hermann Paris, 1909.

[26] K. D. Costa, J. W. Holmes, and A. D. McCulloch. Modelling cardiac mechanical properties in three dimensions. *Philosophical Transactions of the Royal Society A*, 359:1233–1250, 2001.

[27] Stephen C Cowin. An incorrect inequality in micropolar elasticity theory. *Zeitschrift für Angewandte Mathematik und Physik (ZAMP)*, 21(3):494–497, 1970.

[28] Linda L. Demer and Frank C. P. Yin. Passive biaxial mechanical properties of isolated canine myocardium. *Journal of Physiology*, 339:615–630, 1983.

[29] S. Dokos, I. J. LeGrice, B. H. Smaill, J. Kar, and A. A. Young. A triaxial-measurement shear-test device for soft biological tissues. *J Biomech Eng*, 122(5): 471–8, Oct 2000.

[30] Socrates Dokos, Bruce H. Smaill, Alistair A. Young, and Ian J. LeGrice. Shear properties of passive ventricular myocardium. *American Journal of Physiology - Heart and Circulatory Physiology*, 283:H2650–H2659, 2002.

[31] Matthew G. Doyle, Stavros Tavoularis, and Yves Bourgault. Adaptation of a rabbit myocardium material model for use in a canine left ventricle simulation study. *Journal of Biomechanical Engineering*, 132(4):041006, 2010.

[32] Joanna Dukes-McEwan, Michele Borgarelli, Anna Tidholm, Andrea C Vollmar, and Jens Häggström. Proposed guidelines for the diagnosis of canine idiopathic dilated cardiomyopathy. *Journal of Veterinary Cardiology*, 5(2):7–19, 2003.

[33] TSE Eriksson, AJ Prassl, G Plank, and GA Holzapfel. Influence of myocardial fiber/sheet orientations on left ventricular mechanical contraction. *Mathematics and Mechanics of Solids*, 2013.

[34] A Cemal Eringen. Theory of micropolar fluids. Technical report, DTIC Document, 1965.

[35] A Cemal Eringen. *Microcontinuum field theories: foundations and solids*, volume 487. Springer New York, 1999.

[36] A Cemal Eringen and ES Suhubi. Nonlinear theory of simple micro-elastic solidsi. *International Journal of Engineering Science*, 2(2):189–203, 1964.

[37] M. A. Essack. Material parameter identification for modelling the left ventricle in the healthy state. Master's thesis, University of Cape Town.

[38] G M Faber and Y Rudy. Action potential and contractility changes in [na+](i) overloaded cardiac myocytes: A simulation study. *Biophysical Journal*, 78:2392–2404, 2000.

[39] J Fatemi, F Van Keulen, and PR Onck. Generalized continuum theories: Application to stress analysis in bone*. *Meccanica*, 37(4-5):385–396, 2002.

[40] Salvatore Federico, Alfio Grillo, Gaetano Giaquinta, and Walter Herzog. Convex fung-type potentials for biological tissues. *Meccanica*, 43(3):279–288, 2008.

[41] WikiMedia file repository. Wriggers diagram, licenced under creative commons attribution-share alike 2.5 license. `http://en.wikipedia.org/wiki/File:Wiggers_Diagram.svg`. Accessed: 2013-11-29.

[42] NA Fleck, GM Muller, MF Ashby, and JW Hutchinson. Strain gradient plasticity: theory and experiment. *Acta Metallurgica et Materialia*, 42(2):475–487, 1994.

[43] G. M. Fomovsky, S. Thomopoulos, and J. W. Holmes. Contribution of extracellular matrix to the mechanical properties of the heart. *J Mol Cell Cardiol*, 48(3):490–6, Mar 2010.

[44] S Forest, G Cailletaud, and R Sievert. A cosserat theory for elastoviscoplastic single crystals at finite deformation. *Arch. Mech*, 49:705–736, 1997.

[45] M.G.D. Geers, V.G. Kouznetsova, and W.A.M. Brekelmans. Multi-scale computational homogenization: Trends and challenges. *Journal of Computational and Applied Mathematics*, 234(7):2175 – 2182, 2010. ISSN 0377-0427. doi: http://dx.doi.org/10.1016/j.cam.2009.08.077. URL `http://www.sciencedirect.com/science/article/pii/S0377042709005536`. Fourth International Conference on Advanced {COmputational} Methods in {ENgineering} (ACOMEN 2008).

[46] Stephen H. Gilbert, Alan P. Benson, Pan Li, and Arun V. Holden. Regional localisation of left ventricular sheet structure: integration with current models of

cardiac fibre, sheet and band structure. *Eur J Cardiothorac Surg*, 32(2):231–249, August 1, 2007.

[47] S. Göktepe, S. N. S. Acharya, J. Wong, and E. Kuhl. Computational modeling of passive myocardium. *International Journal for Numerical Methods in Biomedical Engineering*, 27(1):1–12, 2011. ISSN 2040-7947.

[48] J M Guccione. *Computational Cardiovascular Mechanics*. Springer, 2010.

[49] J M Guccione, L K Waldman, and A D McCulloch. Mechanics of active contraction in cardiac muscle: Part ii-cylindrical models of the systolic left ventricle. *ASME Journal of Biomechanical Engineering*, 115:82–90, 1993.

[50] J. M. Guccione, K. D. Costa, and A. D. McCulloch. Finite element stress analysis of left ventricular mechanics in the beating dog heart. *Journal of Biomechanical Engineering*, 28:1167–1177, 1995.

[51] J. M. Guccione, A. Salahieh, S. M. Moonly, J. Kortsmit, A. W. Wallace, and M. B. Ratcliffe. Myosplint decreases wall stress without depressing function in the failing heart: a finite element model study. *Ann Thorac Surg*, 76(4):1171–80; discussion 1180, Oct 2003.

[52] JM Guccione, GS Le Prell, PP De Tombe, and WC Hunter. Measurements of active myocardial tension under a wide range of physiological loading conditions. *Journal of biomechanics*, 30(2):189–192, 1997.

[53] K. B. Gupta, M. B. Ratcliffe, M. A. Fallert, L. H. Edmunds, and D. K. Bogen. Changes in passive mechanical stiffness of myocardial tissue with aneurysm formation. *Circulation*, 89:2315–2326, 1994.

[54] Peter J Hanley, Alistair A Young, Ian J LeGrice, Stephen G Edgar, and Denis S Loiselle. 3-dimensional configuration of perimysial collagen fibres in rat cardiac muscle at resting and extended sarcomere lengths. *The Journal of physiology*, 517 (3):831–837, 1999.

[55] Keith L Herrmann, Andrew D McCulloch, and Jeffrey H Omens. Glycated collagen cross-linking alters cardiac mechanics in volume-overload hypertrophy. *American Journal of Physiology-Heart and Circulatory Physiology*, 284(4):H1277–H1284, 2003.

[56] J. W. Holmes, T. K. Borg, and J. W. Covell. Structure and mechanics of healing myocardial infarcts. *Annual Review of Biomedical Engineering*, 7:223–253, 2005.

[57] G. A Holzapfel. *Encyclopedia of Computational Mechanics*, chapter Computational Biomechanics of Soft Biological Tissue. John Wiley & Sons, 2004.

[58] G. A. Holzapfel and R. W. Ogden. Constitutive modelling of passive myocardium: a structurally based framework for material characterization. *Philosophical Transactions of the Royal Society a-Mathematical Physical and Engineering Sciences*, 367(1902):3445–3475, Sep 13 2009. ISSN 1364-503X.

[59] Gerhard A Holzapfel. *Nonlinear solid mechanics: a continuum approach for engineering*. John Wiley & Sons Ltd., 2000.

[60] Gerhard A Holzapfel. Biomechanics of soft tissue. *The handbook of materials behavior models*, 3:1049–1063, 2001.

[61] Gerhard A Holzapfel, Thomas C Gasser, and Ray W Ogden. A new constitutive framework for arterial wall mechanics and a comparative study of material models. *Journal of elasticity and the physical science of solids*, 61(1-3):1–48, 2000.

[62] Cornelius O Horgan and Jeremiah G Murphy. On the modeling of extension-torsion experimental data for transversely isotropic biological soft tissues. *Journal of Elasticity*, 108(2):179–191, 2012.

[63] JD Humphrey. Review paper: Continuum biomechanics of soft biological tissues. *Proceedings of the Royal Society of London. Series A: Mathematical, Physical and Engineering Sciences*, 459(2029):3–46, 2003.

[64] J.D. Humphrey and FC Yin. Constitutive relations and finite deformations of passive cardiac tissue ii: stress analysis in the left ventricle. *Circulation research*, 65(3):805–817, 1989.

[65] JD Humphrey and FCP Yin. On constitutive relations and finite deformations of passive cardiac tissue: I. a pseudostrain-energy function. *Journal of biomechanical engineering*, 109:298, 1987.

[66] Jagir R Hussan, Mark L Trew, and Peter J Hunter. A mean-field model of ventricular muscle tissue. *Journal of biomechanical engineering*, 134(7), 2012.

[67] David Jegger, Ajit S Mallik, Mohammed Nasratullah, Xavier Jeanrenaud, Rafaela da Silva, Hendrik Tevaearai, Ludwig K von Segesser, and Nikolaos Stergiopulos. The effect of a myocardial infarction on the normalized time-varying elastance curve. *Journal of Applied Physiology*, 102(3):1123–1129, 2007.

[68] B. I. Jugdutt. Ventricular remodeling after infarction and the extracellular collagen matrix: when is enough enough? *Circulation*, 108(11):1395–403, Sep 16 2003.

[69] B. I. Jugdutt and R. W. Amy. Healing after myocardial infarction in the dog: changes in infarct hydroxyproline and topography. *Journal of the American College of Cardiology*, 7(1):91–102, 1986. ISSN 0735-1097.

[70] Arnold Katz. *Physiology of the Heart*. Wolters Kluwer Health, 2011.

[71] R. C. Kerckhoffs, O. P. Faris, P. H. Bovendeerd, F. W. Prinzen, K. Smits, E. R. McVeigh, and T. Arts. Timing of depolarization and contraction in the paced canine left ventricle: model and experiment. *J Cardiovasc Electrophysiol*, 14(10 Suppl):S188–95, Oct 2003.

[72] Roy Kerckhoffs. *Depolarization wave and mechanics in the paced heart: model and experiment*. PhD thesis, Tehcnical University of Eindhoven, 2003.

[73] S Kessel. The stress functions of the cosserat continuum (translated from german). *ZAMM-Journal of Applied Mathematics and Mechanics/Zeitschrift für Angewandte Mathematik und Mechanik*, 47(5):329–336, 1967.

[74] S. Klinkel, C. Sansour, and W. Wagner. An anisotropic fibre-matrix material model at finite elastic-plastic strains. *Computational Mechanics*, 35:409–417, 2005.

[75] Jeroen Kortsmit, Neil H Davies, Renee Miller, Jesse R Macadangdang, Peter Zilla, and Thomas Franz. The effect of hydrogel injection on cardiac function and myocardial mechanics in a computational post infarction model. *Computer Methods in Biomechanics and Biomedical Engineering*, 2012.

[76] Varvara Kouznetsova, Marc GD Geers, and WA Marcel Brekelmans. Multi-scale constitutive modelling of heterogeneous materials with a gradient-enhanced computational homogenization scheme. *International Journal for Numerical Methods in Engineering*, 54(8):1235–1260, 2002.

[77] V.G. Kouznetsova, M.G.D. Geers, and W.A.M. Brekelmans. Multi-scale second-order computational homogenization of multi-phase materials: a nested finite element solution strategy. *Computer Methods in Applied Mechanics and Engineering*, 193(4851):5525 – 5550, 2004. ISSN 0045-7825. doi: http://dx.doi.org/10.1016/j.cma.2003.12.073. URL `http://www.sciencedirect.com/science/article/pii/S0045782504002853`. Advances in Computational Plasticity.

[78] Gaurav Krishnamurthy, Daniel B Ennis, Akinobu Itoh, Wolfgang Bothe, Julia C Swanson, Matts Karlsson, Ellen Kuhl, D Craig Miller, and Neil B Ingels. Material properties of the ovine mitral valve anterior leaflet in vivo from inverse finite element analysis. *American Journal of Physiology-Heart and Circulatory Physiology*, 295(3):H1141–H1149, 2008.

[79] RS Lakes. Experimental microelasticity of two porous solids. *International Journal of Solids and Structures*, 22(1):55–63, 1986.

[80] Michael M Laks, Michael J Nisenson, and HJC Swan. Myocardial cell and sarcomere lengths in the normal dog heart. *Circulation research*, 21(5):671–678, 1967.

[81] Steven Lavine. Effect of changes in contractility on the index of myocardial performance in the dysfunctional left ventricle. *Cardiovascular ultrasound*, 4(1):45, 2006.

[82] D. Legner, S. Skatulla, J. MBewu, R.R. Rama B.D. Reddy, C. Sansour, N.H. Davies, and T. Franz. Studying the influence of hydrogel injections into the infarcted left ventricle using the element-free galerkin method. *International Journal for Numerical Methods in Biomedical Engineering*, 2013. under review.

[83] I. Legrice, P Hunter, A Young, and B Smaill. The architecture of the heart: a data-based model. *Philosophical Transactions of the Royal Society A*, 359:1217–1232, 2001.

[84] Kenneth Levenberg. A method for the solution of certain problems in least squares. *Quarterly of applied mathematics*, 2:164–168, 1944.

[85] Vafa Mansouri and Steven J Lavine. Effect of external constraint on the index of myocardial performance in a canine model of left ventricular dysfunction. *Echocardiography*, 24(7):712–722, 2007.

[86] G Thomas Mase and George E Mase. *Continuum mechanics for engineers*. Crc Press, 2010.

[87] C Mathers and Dejan Loncar. Updated projections of global mortality and burden of disease, 2002-2030: data sources, methods and results. *Geneva: World Health Organization*, 2005.

[88] Gérard A Maugin. Generalized continuum mechanics: What do we mean by that? In *Mechanics of Generalized Continua*, pages 3–13. Springer, 2010.

[89] A D McCulloch, B H Smaill, and P J Hunter. Regional left ventricular deformation in the passive dog heart. *Circulation Research*, 64:721–733, 1989.

[90] Andrew W McFarland and Jonathan S Colton. Role of material microstructure in plate stiffness with relevance to microcantilever sensors. *Journal of Micromechanics and Microengineering*, 15(5):1060, 2005.

[91] RD Mindlin. Micro-structure in linear elasticity. *Archive for Rational Mechanics and Analysis*, 16(1):51–78, 1964.

[92] RD Mindlin and HF Tiersten. Effects of couple-stresses in linear elasticity. *Archive for Rational Mechanics and Analysis*, 11(1):415–448, 1962.

[93] I Münch, P Neff, and W Wagner. Transversely isotropic material: nonlinear cosserat versus classical approach. *Continuum Mechanics and Thermodynamics*, 23(1):27–34, 2011.

[94] MP Nash and PJ Hunter. Computational mechanics of the heart. *Journal of elasticity*, 61(1):113–141, 2000. ISSN 0374-3535.

[95] H Neuber. On problems of stress concentration in cosserat bodies (translated from german). *Acta Mechanica*, 2(1):48–69, 1966.

[96] Steven A Niederer and Nicolas P Smith. The role of the frank–starling law in the transduction of cellular work to whole organ pump function: A computational modeling analysis. *PLoS computational biology*, 5(4):e1000371, 2009.

[97] P M F Nielsen, I J LeGrice, B H Smaill, and P J Hunter. Mathematical model geometry and fibrous structure of the heart. *American Journal of Physiology*, 260: H1365–H1378, 1991.

[98] T.G. Nyland and J.S. Mattoon. *Small Animal Diagnostic Ultrasound*. Saunders, 2002. ISBN 9780721677880.

[99] J. H. Omens, T. P. Usyk, Z. J. Li, and A. D. McCulloch. Muscle lim protein deficiency leads to alterations in passive ventricular mechanics. *American Journal of Physiology-Heart and Circulatory Physiology*, 282(2):H680–H687, Feb 2002. ISSN 0363-6135.

[100] Jeffrey H Omens and Y C Fung. Residual strain in rat left ventricle. *Circulation Research*, 66:37–45, 1990.

[101] Jeffrey H Omens, Deidre A MacKenna, and Andrew D McCulloch. Measurement of strain and analysis of stress in resting rat left ventricular myocardium. *Journal of biomechanics*, 26(6):665–676, 1993.

[102] Dinesh K Pai. Strands: Interactive simulation of thin solids using cosserat models. In *Computer Graphics Forum*, volume 21, pages 347–352. Wiley Online Library, 2002.

[103] HC Park and RS Lakes. Cosserat micromechanics of human bone: strain redistribution by a hydration sensitive constituent. *Journal of biomechanics*, 19(5): 385–397, 1986.

[104] Jinah Park, Dimitri Metaxas, Alistair A Young, and Leon Axel. Deformable models with parameter functions for cardiac motion analysis from tagged mri data. *Medical Imaging, IEEE Transactions on*, 15(3):278–289, 1996.

[105] M. A. Pfeffer, E. Braunwald, L. A. Moye, L. Basta, Jr. Brown E. J., T. E. Cuddy, B. R. Davis, E. M. Geltman, S. Goldman, G. C. Flaker, and et al. Effect of captopril on mortality and morbidity in patients with left ventricular dysfunction after myocardial infarction. results of the survival and ventricular enlargement trial. the save investigators. *N Engl J Med*, 327(10):669–77, Sep 3 1992.

[106] M.A. Pfeffer and E. Braunwald. Ventricular remodeling after myocardial infarction. experimental observations and clinical implications. *Circulation*, 81(4):1161, 1990.

[107] JH Poynting. On pressure perpendicular to the shear planes in finite pure shears, and on the lengthening of loaded wires when twisted. *Proceedings of the Royal Society of London. Series A, Containing Papers of a Mathematical and Physical Character*, 82(557):546–559, 1909.

[108] Frank E Rademakers, MB Buchalter, Walter J Rogers, Elias A Zerhouni, Myron L Weisfeldt, James L Weiss, and Edward P Shapiro. Dissociation between left ventricular untwisting and filling. accentuation by catecholamines. *Circulation*, 85(4): 1572–1581, 1992.

[109] J.S Rankin, P.A McHale, C.E Arentzen, D Ling, J.C Greenfield, and R.W Anderson. The three-dimensional dynamic geometry of the left ventricle in the conscious dog. *Circulation Research*, 39(3):304–313, 1976.

[110] Espen W Remme, Alistair A Young, Kevin F Augenstein, Brett Cowan, and Peter J Hunter. Extraction and quantification of left ventricular deformation modes. *Biomedical Engineering, IEEE Transactions on*, 51(11):1923–1931, 2004.

[111] J. Rijcken, P. H. Bovendeerd, A. J. Schoofs, D. H. van Campen, and T. Arts. Optimization of cardiac fiber orientation for homogeneous fiber strain during ejection. *Ann Biomed Eng*, 27(3):289–97, May-Jun 1999.

[112] D.E Roberts, L.T Hersh, and A.M Scher. Influence of cardiac fiber orientation on wavefront voltage, conduction velocity, and tissue resistivity in the dog. *Circulation Research*, 44(5):701–712, 1979.

[113] E.K. Rodriguez, J.H. Omens, LK Waldman, and AD McCulloch. Effect of residual stress on transmural sarcomere length distributions in rat left ventricle. *American Journal of Physiology-Heart and Circulatory Physiology*, 264(4):H1048, 1993.

[114] Ignacio Rodriguez, Daniel B Ennis, and Han Wen. Noninvasive measurement of myocardial tissue volume change during systolic contraction and diastolic relaxation in the canine left ventricle. *Magnetic resonance in medicine*, 55(3):484–490, 2006.

[115] Josef Rosenberg and Robert Cimrman. Microcontinuum approach in biomechanical modeling. *Mathematics and Computers in Simulation*, 61(3):249–260, 2003.

[116] I K Russel. *Myocardial strain, torsion and untwisting in the normal and failing heart measured with magnetic resonance imaging.* PhD thesis, V U University Amsterdam, 2010.

[117] Frank B Sachse, K G Glanzel, and G Seemann. Modeling of protein interactions involved in cardiac tension development. *International Journal of Bifurcation and Chaos*, 13:3561–3578, 2003.

[118] Michael S Sacks. Biaxial mechanical evaluation of planar biological materials. *Journal of elasticity and the physical science of solids*, 61(1-3):199–246, 2000.

[119] C Sansour. A unified concept of elastic-viscoplastic cosserat and micromorphic continua. *Le Journal de Physique IV*, 8(PR8):Pr8–341, 1998.

[120] C Sansour. A theory of the elastic-viscoplastic cosserat continuum. *Archives of Mechanics*, 50(3):577–597, 1998.

[121] C. Sansour and S. Skatulla. A non-linear cosserat continuum-based formulation and moving least square approximations in computations of size-scale effects in elasticity. *Computational Materials Science*, 41:589–601, 2008.

[122] C Sansour, S Skatulla, and H Zbib. A formulation for the micromorphic continuum at finite inelastic strains. *International Journal of Solids and Structures*, 47(11): 1546–1554, 2010.

[123] Carlo Sansour and Herbert Bednarczyk. The cosserat surface as a shell model, theory and finite-element formulation. *Computer Methods in Applied Mechanics and Engineering*, 120(1):1–32, 1995.

[124] Carlo Sansour and Hans Bufler. An exact finite rotation shell theory, its mixed variational formulation and its finite element implementation. *International Journal for Numerical Methods in Engineering*, 34(1):73–115, 1992.

[125] Stanley J Sarnoff and Erik Berglund. Ventricular function i. starling's law of the heart studied by means of simultaneous right and left ventricular function curves in the dog. *Circulation*, 9(5):706–718, 1954.

[126] H Schaefer. Das cosserat kontinuum (german). *ZAMM-Journal of Applied Mathematics and Mechanics/Zeitschrift für Angewandte Mathematik und Mechanik*, 47 (8):485–498, 1967.

[127] Thomas F Schaible, Ashwani Malhotra, Gary Ciambrone, and James Scheuer. The effects of gonadectomy on left ventricular function and cardiac contractile proteins in male and female rats. *Circulation research*, 54(1):38–49, 1984.

[128] Thomas Schlosser, Konstantin Pagonidis, Christoph U Herborn, Peter Hunold, Kai-Uwe Waltering, Thomas C Lauenstein, and Jorg Barkhausen. Assessment of left ventricular parameters using 16-mdct and new software for endocardial and epicardial border delineation. *American Journal of Roentgenology*, 184(3):765–773, 2005.

[129] A. Schmidt, C.F. Azevedo, A. Cheng, S.N. Gupta, D.A. Bluemke, T.K. Foo, G. Gerstenblith, R.G. Weiss, E. Marban, G.F. Tomaselli, et al. Infarct tissue heterogeneity by magnetic resonance imaging identifies enhanced cardiac arrhythmia susceptibility in patients with left ventricular dysfunction. *Circulation*, 115 (15):2006, 2007.

[130] Partho P Sengupta, Bijoy K Khandheria, and Jagat Narula. Twist and untwist mechanics of the left ventricle. *Heart failure clinics*, 4(3):315–324, 2008.

[131] S. Skatulla and C. Sansour. A nonlinear generalized formulation with free rotations applied to meshfree approximations describing microstructure related material behaviour. *Computer Methods in Applied Mechanics and Engineering*, 2012.

[132] Sebastian Skatulla. *Computational aspects of generalized continua based on moving least square approximations*. PhD thesis, University of Adelaide, 2006.

[133] NP Smith, DP Nickerson, EJ Crampin, and PJ Hunter. Multiscale computational modelling of the heart. *Acta Numerica*, 13(1):371–431, 2004.

[134] James Southern, Joe Pitt-Francis, Jonathan Whiteley, Daniel Stokeley, Hiromichi Kobashi, Ross Nobes, Yoshimasa Kadooka, and David Gavaghan. Multi-scale computational modelling in biology and physiology. *Progress in Biophysics and Molecular Biology*, 96(1-3):60 – 89, 2008. ISSN 0079-6107. Cardiovascular Physiome.

[135] Jonas Spillmann and Matthias Teschner. C o r d e: Cosserat rod elements for the dynamic simulation of one-dimensional elastic objects. In *Proceedings of the 2007 ACM SIGGRAPH/Eurographics symposium on Computer animation*, pages 63–72. Eurographics Association, 2007.

[136] Paul Steinmann. A micropolar theory of finite deformation and finite rotation multiplicative elastoplasticity. *International Journal of Solids and Structures*, 31 (8):1063–1084, 1994.

[137] Daniel D Streeter and William T Hanna. Engineering mechanics for successive states in canine left ventricular myocardium ii. fiber angle and sarcomere length. *Circulation Research*, 33(6):656–664, 1973.

[138] D.D. Streeter JR. Gross morphology and fiber geometry of the heart. *Handbook of physiology: a critical, comprehensive presentation of physiological knowledge and concepts. The cardiovascular system: Formerly Section 2: Circulation. The heart*, 1:61, 1979.

[139] Kenji Sunagawa, W Lowell Maughan, and Kiichi Sagawa. Optimal arterial resistance for the maximal stroke work studied in isolated canine left ventricle. *Circulation research*, 56(4):586–595, 1985.

[140] Cory Swingen, Xiaoen Wang, and Michael Jerosch-Herold. Evaluation of myocardial volume heterogeneity during end-diastole and end-systole using cine mri. *Journal of Cardiovascular Magnetic Resonance*, 6(4):829–835, 2004.

[141] Larry A Taber, Ming Yang, and W William Podszus. Mechanics of ventricular torsion. *Journal of biomechanics*, 29(6):745–752, 1996.

[142] PK DELLA TORRE, AC Kirby, DB Church, and R Malik. Echocardiographic measurements in greyhounds, whippets and italian greyhounds-dogs with a similar conformation but different size. *Australian veterinary journal*, 78(1):49–55, 2000.

[143] RA Toupin. Elastic materials with couple-stresses. *Archive for Rational Mechanics and Analysis*, 11(1):385–414, 1962.

[144] RA Toupin. Theories of elasticity with couple-stress. *Archive for Rational Mechanics and Analysis*, 17(2):85–112, 1964.

[145] SWJ Ubbink, PHM Bovendeerd, Tammo Delhaas, Theo Arts, and Frans N van de Vosse. Towards model-based analysis of cardiac mr tagging data: relation between left ventricular shear strain and myofiber orientation. *Medical image analysis*, 10 (4):632–641, 2006.

[146] Kazunori Uemura, Toru Kawada, Masaru Sugimachi, Can Zheng, Koji Kashihara, Takayuki Sato, and Kenji Sunagawa. A self-calibrating telemetry system for measurement of ventricular pressure-volume relations in conscious, freely moving rats. *American Journal of Physiology-Heart and Circulatory Physiology*, 287(6):H2906–H2913, 2004.

[147] Taras P. Usyk, Ian J. LeGrice, and Andrew D. McCulloch. Computational model of three-dimensional cardiac electromechanics. *Computing and Visualization in Science*, 4:249–257, 2002. ISSN 1432-9360. 10.1007/s00791-002-0081-9.

[148] T.P. Usyk, R. Mazhari, and A.D. McCulloch. Effect of laminar orthotropic myofiber architecture on regional stress and strain in the canine left ventricle. *Journal of Elasticity*, 61:143–164, 2000. ISSN 0374-3535.

[149] L. K. Waldman, Y. C. Fung, and J. W. Covell. Transmural myocardial deformation in the canine left ventricle. normal in vivo three-dimensional finite strains. *Circ Res*, 57(1):152–63, Jul 1985.

[150] C-C Wang. A new representation theorem for isotropic functions. *Archive for Rational Mechanics and Analysis*, 36(3):166–197, 1970.

[151] Karl T Weber. Cardiac interstitium in health and disease: the fibrillar collagen network. *Journal of the American College of Cardiology*, 13(7):1637–1652, 1989.

[152] Karl T Weber, Piero Anversa, Paul W Armstrong, Christian G Brilla, John C Burnett Jr, John M Cruickshank, Richard B Devereux, Thomas D Giles, Niels Korsgaard, Carl V Leier, et al. Remodeling and reparation of the cardiovascular system. *Journal of the American College of Cardiology*, 20(1):3–16, 1992.

[153] KT Weber, JS Janicki, SG Shroff, R. Pick, RM Chen, and RI Bashey. Collagen remodeling of the pressure-overloaded, hypertrophied nonhuman primate myocardium. *Circulation research*, 62(4):757–765, 1988.

[154] N. Westerhof, J. Lankhaar, and B.E. Westerhof. The arterial windkessel. *Med. Biol. Eng. Comput.*, 47:131–141, 2009.

[155] Jonathan Wong and Ellen Kuhl. Generating fibre orientation maps in human heart models using poisson interpolation. *Computer methods in biomechanics and biomedical engineering*, (ahead-of-print):1–10, 2012.

[156] P. Wriggers. *Nonlinear finite element methods*. Springer Verlag, 2008.

[157] JFC Yang and Roderic S Lakes. Experimental study of micropolar and couple stress elasticity in compact bone in bending. *Journal of biomechanics*, 15(2):91–98, 1982.

[158] QS Zheng. Theory of representations for tensor functions—a unified invariant approach to constitutive equations. *Applied Mechanics Reviews*, 47(11):545–587, 1994.